Electron Acceleration by Coherent Laser Pulses in Periodic Structures

Inaugural-Dissertation

zur Erlangung des Doktorgrades
der Mathematisch-Naturwissenschaftlichen Fakultät
der Heinrich-Heine-Universität Düsseldorf

vorgelegt von

Phuc Luu-Thanh

aus Ho Chi Minh Stadt, Vietnam

Düsseldorf, May 9th, 2016

aus dem Institut für Theoretische Physik I
der Heinrich-Heine-Universität Düsseldorf

Gedruckt mit der Genehmigung der
Mathematisch-Naturwissenschaftlichen Fakultät der
der Heinrich-Heine-Universität Düsseldorf

Referent: Prof. Dr. A. Pukhov
Korreferent: Prof. Dr. Dr. C. Müller
Tag der mündlichen Prüfung:

Statement of Authorship

I declare under oath that I have compiled my dissertation independently and without any undue assistance by third parties under consideration of the "Principles for the Safeguarding of Good Scientific Practice at Heinrich Heine Universität Düsseldorf".

Phuc Luu-Thanh
Düsseldorf, May 9th, 2016

Abstract

With the coming-of-age of the lithography and fibre laser technologies, the interest of developing a compact and economic particle accelerator has increased in recent years. In this thesis, we propose a particle acceleration in periodic structures. Since the acceleration mechanism is based on the direct interaction between particles and lasers, it is also referred as direct laser acceleration, in contrast with the plasma acceleration. The structure consists of many rectangular blocks (called shields) with cylindrical holes at the centre. The blocks are separated by half laser wavelength from each other such that there is a gap for the longitudinal electric field component to accelerate particles. The proposed scheme is ready to be integrated into a scalable multi-stage electron acceleration.

The investigation is done by performing simulations with the Virtual Laser Plasma Laboratory (VLPL) code. The particles will be inject into the scheme and pass through dozen periods of the silicon structure. The acceleration gradient is calculated to be approximately 136 GeV/m. We also study the effect of the ionisation on the stability of the scheme.

Due to their high electrical breakdown, heavier dielectric materials are desirable for the scheme. However, the ionisation process likely leads to the abundance of electrons in the simulation domain, which can lessen the computation speed. Thus, we also report in this thesis the development of the Voronoi particle merging algorithm as an integral part of the VLPL code. The core concept is using the Voronoi tessellation to group similar particles in the phase space. In this manner, the growth of particles in the simulation box is put under control while the physical description of the system is not strongly distorted. The algorithm can enhance the computation performance and is serviceable for simulations where the number of particles grows exponentially.

Zusammenfassung

Mit der Etablierung von Lithographie und Faserlasern ist das Interesse an der Entwicklung von einem kompakten und wirtschaftlichen Teilchenbeschleuniger in der letzten Jahren angestiegen. In dieser Arbeit schlagen wir eine Teilchenbeschleunigung in periodischen Strukturen vor. Da der Beschleunigungsmechanismus auf der direkten Wechselwirkung zwischen den Teilchen und dem Laser basiert, wird dieser Prozess auch als direkte Laserbeschleunigung bezeichnet, im Gegensatz zu der Plasmabeschleunigung. Die Struktur besteht aus vielen rechteckigen Blöcken (sogenannten Schilden) mit zylindrischen Bohrungen in der Mitte. Die Blöcke sind durch eine halbe Laserwellenlänge voneinander getrennt, so dass es Raum für die longitudinale Komponente des elektrischen Feldes gibt, um Partikel zu beschleunigen.

Die Untersuchung wird durch Simulationen mit dem Virtual Laser-Plasma Laboratory (VLPL) Code fertiggestellt. Die Partikel werden in dem Aufbau injiziert und fahren durch ein Dutzend Perioden der Siliziumstruktur. Der Beschleuningungsgradient wird zu ca. 136 GeV/m berechnent. Des Weiteren untersuchen wir die Wirkung der Ionisation auf die Stabilität des Systems.

Aufgrund ihrer höheren elektrischen Durchschlagschwelle sind schwerere dielektrische Materialen für das Schema wünschenwert. Jedoch führt die Ionisation warscheinlich zu einem Überfluss von Elektronen in der Simulationsdomain, was die Rechengeschwindigkeit verringern kann. So berichten wir in dieser Arbeit auch von der Entwicklung des verschmelzenden Voronoi Partikel Algorithmus als integralem Bestandteil des VLPL Codes. Das Kernkonzept benutzt den Voronoi Tessellation, um ähnliche Partikel im Phasenraum zu gruppieren. Auf diese Weise wird das Wachstum der Partikel in der Simulationsbox unter Kontrolle gehalten, wärent die physikalische Beschreibung des Systems nicht stark verzerrt wird. Der Algorithmus kann die Rechenleistung

verbessern und ist betriebsbereit für Simulationen, bei denen die Anzahl der Partikel exponentiell wächst.

Acknowledgements

I would like, first and foremost, to thank Prof. Dr. Alexander Pukhov. While writing this thesis, the biggest help is from him, who has been generous with his time for reading through the draft and giving constructive feedbacks. I am also grateful to him for giving insights and understandings and providing financial support.

I am glad to acknowledge my debt of gratitude to Prof. Dr. Dr. Carsten Müller for his willingness to be my mentor and also second reviewer for this thesis. Many consultations with him have proven to be invaluable in finishing this work.

A special word of thanks goes to Frau Elvira Gröters, the peerless and ever-cheery secretary of the Institut. Many thanks must go to Evgenij Bleile. This work cannot be complete without his work maintaining the cluster.

I acknowledge my debt of gratitude to Tobias Tückmantel for his generous effort in teaching me how to use the code and many insightful comments. To Friedrich Schluck and Vural Kaymak, their generosity and criticism are invaluable gifts to me in preparing this work.

To other individuals I express my heartfelt gratitude: Götz Lehmann, Liangliang Ji, Oliver Jansen, Mykyta Charednycheck, Debin Zou, Longquing Yi, Zi-Yu Chen, Selym Villalba, Johannes Thomas, John Farmer, Roberto Martorelli, Matthias Dellweg, Martin Jansen, Alexey Snydnikov, Christoph Baumann, Michael Jansen, Anvar Khujakulov, and Soroosh Alighanbari.

Most importantly, I thank my parents, Luu Van Ly and Uong Thi Tam, for encouraging me during the research and their unconditional support.

Contents

CHAPTER 1

Introduction

Atoms are mindless particles and none of them are considered to be *alive*. Mysteriously, trillions of them engage in a particular arrangement and a willing manner to create a functioning human body. Not only that, they form all organic living things on Earth. They are the essential constituents of the Universe's miraculous state known as life. Despite this, they are not the smallest particles known by mankind. Tinier are protons and electrons. It was theorised by Murray Gell-Mann and G. Zweig [1] that if we delved deeper into the proton structure, we would find quarks, the fundamental building blocks of matter. This theory was then verified by experiments in 1968 [2] at the Stanford Linear Accelerator Center (SLAC). The thrilling journey of finding subatomic particles has not yet ended with these findings. In 2013, particle physicists triumphed once more when CERN[†] proudly proclaimed that the Higgs boson, first proposed by P. Higgs [3] in 1964, was experimentally discovered in Geneva, Switzerland [4].

[*]French: Conseil Européen pour la Recherche Nucléaire; English: European Council for Nuclear Research.

The progress and fame of particle physics cannot be acknowledged without giving credit to a less popular physical discipline, *particle acceleration*. Quarks' physical existence was first perceived at SLAC. SLAC's main accelerator is an RF linear accelerator which is 3.2 km long and buried 10 m below grounds. According to data published in 1993 [5], the establishment of SLAC facility amounted to $600ml (approx. €528.5ml), *"excluding the original R&D, the cost of SLC"*. On the other hand, the hunting for Higgs boson initiated the construction of the world's most powerful and largest particle experiment complex, CERN's Large Hadron Collider (LHC). With the annual budget of €7.5bn*, it occupies an area of 27 km in circumference, 175 m under the France-Switzerland border. In these gigantic machines, the particles can get accelerated up to 50 GeV (for electrons and positrons at SLAC) or 6.5 TeV (for protons at CERN).

Not all particle accelerators are as enormous as these colossi and solely dedicated to explore the fundamental layer of matter. They can be used as sources of X-ray radiations (synchrotron radiation or free electron laser). These high energy photon beams are valuable assets in many scientific fields, such as material science, chemistry, and biology. Moreover, particle accelerators also find their place in the modern daily life: in hospitals or in specialised clinics. Not as grand as their relatives, these humble machines serve a noble purpose: to treat cancer.

Due to all benefits it bestows, it is desirable to own a powerful accelerator. Unfortunately, not all research facilities nor hospitals acquire huge land area or large budget plan like SLAC or CERN. Thus, over the years, many works have

*For more detail, see: http://askanexpert.web.cern.ch/AskAnExpert/en/Accelerators/LHCgeneral-en.html#3

been dedicated to create a compact and powerful particle accelerator. In this thesis, we propose the novel idea of particle acceleration in periodic structures. The scheme is readily compact and thus can be integrated into a multi-stage accelerator. Our scheme consists of multiple identical cuboids, called shielding blocks, which are separated from each other by half the laser wavelength. The main objective of these blocks is to limit the interaction length between the particle beam and the lasers such that the particles only experience only the accelerating phase.

The works in this thesis are done by using the particles-in-cell (PIC) simulation code Virtual Laser Plasma Laboratory (VLPL) developed by Prof. A. Pukhov. Nowadays, PIC codes can be downloaded for free (e.g. EPOCH[†]) or requires commercial licenses (e.g. VORPAL [6]). Despite being different in the ways of distribution, PIC programs utilise the same core concept: the usage of macro-particles to represent plasma's particle distribution function in the full six-dimensional phase space. Being able to run on high performance computational grids or clusters, the PIC algorithm has a wide range of service, from particle physics to astrophysics. First introduced in the 1960s, a PIC simulation consisted of merely several hundred macro-particles. The simulation complexity has grown considerably afterwards: in several scenarios, millions of particles might be required in order to obtain a decent result. Although the advancement of computer technology has helped to mitigate this problem, the bottleneck issue still exists.

Another approach is to merge particles during simulations. This strategy is favourable and advantageous in certain cases in which the number of particles

[†]See: https://ccpforge.cse.rl.ac.uk/gf/project/epoch/

grows constantly, e.g. pair production or ionisation. The procedure must be carried out such that the phase space must not be distorted after a merging event and the fundamental physics conservation laws must be obeyed. Within the scope of this thesis, the Voronoi particle merging algorithm is presented. The algorithm operates on the basis of tessellation of the 6D phase space. The particles are grouped together if they are close together in the phase space. The distance measure is defined through the Voronoi diagram. Moreover, our algorithm also provides a mean to directly control the errors due to merging events. The algorithm is tested in several scenarios and yields positive results.

The thesis is organised as follows

- In **Chapter 2**, I give the overview of the Lawson-Woodward theorem, which is fundamental in particle acceleration. Then I present a short survey of the recent development in particle acceleration (laser wakefield acceleration and dielectric laser acceleration). Also included in this chapter are basic knowledge that are required for the simulations and data analysis: optical field ionisation and emittance.

- **Chapter 3** is reserved for the particles-in-cell algorithm. The explanation of the macro-particle concept is given. Other necessary algorithms like finite difference time domain method and Boris pusher are also covered in this chapter. Furthermore, the parallel implementation of PIC code in VLPL is also briefly introduced.

- **Chapter 4** features the particle acceleration scheme in periodic structures. I also explore several aspects of the scheme in detail.

- In **Chapter 5**, I describe the simulation setup in order to test the performance of our acceleration scheme. Then the simulation results are presented and discussed.

- **Chapter 6** involves the design of the Voronoi particle merging algorithm. The algorithm is explained thoroughly in every step. I also discuss the issue of the energy conservation in particle merging algorithm in general and the ways to improve it. Afterwards the analysis of simulation results is presented and studied.

- **Chapter 7** is the final chapter of this thesis. Here I summarise my works and explore the prospects of future developments for our acceleration scheme and particle merging algorithm.

CHAPTER 2

General Aspects

2.1 Lawson-Woodward theorem

Consider an electron travelling in vacuum across a transverse laser field. In one half of the laser oscillation, the phase of the field can be supportive for particle acceleration. Thus, in this duration, the particle can extract energy from the field (see Fig. 2.1a). However, this accelerating phase will eventually reverse to become the decelerating phase. In the second half of the laser oscillation, the laser phase changes signs and the particle gets decelerated as a consequence (see Fig. 2.1b). In total, the particle gains no energy in one laser cycle. Mathematically, the energy gain by the particle is given by [7]

$$\Delta E = e\mathcal{E}_0 \sin\theta \int_{-\infty}^{+\infty} v \cos\left[\omega t \left(\beta \cos\theta - 1\right)\right] dt = 0. \tag{2.1}$$

Here, $\mathcal{E}_0$ is the laser's amplitude, ω its frequency; v is the electron velocity, $\beta = v/c$ with c is the speed of light; θ is the angle between the electron's and

laser's propagation direction.

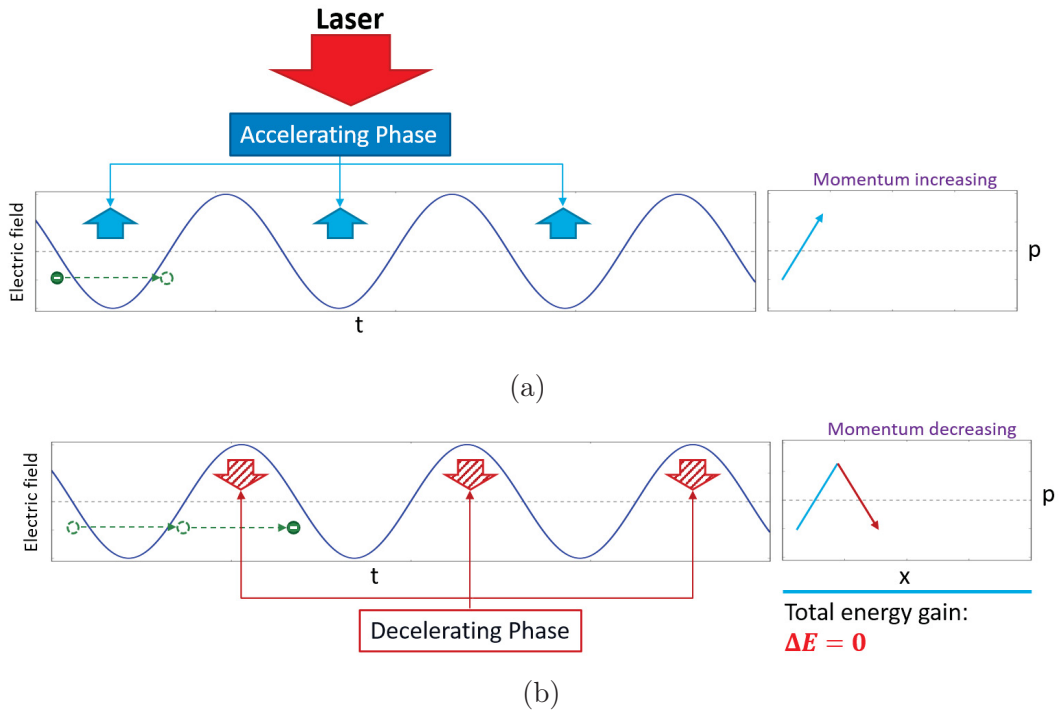

Figure 2.1: An electron travelling across a transverse laser field in vacuum. (a) The particle gains energy in the first half of the laser oscillation. (b) The field becomes decelerating in the second half of the oscillation.

In the field of particle acceleration, the *Lawson-Woodward theorem* [8][9] provides an important guideline to consider under which circumstances the particle acceleration is possible. It states that particles will gain no energy under following circumstances

1. The interaction takes place in vacuum.
2. No boundaries or surfaces (dielectric, conductor, or plasma) are present.
3. The particle is highly relativistic.
4. The interaction region is infinitely large.

5. Non-linear forces (e.g. ponderomotive forces) are neglected.

Thus, in order to accelerate relativistic particles one has to violate at least one of these conditions. In this chapter, we will review two most interesting approaches to accelerate particles to relativistic energy: wakefield acceleration and dielectric laser acceleration.

2.2 Wakefield acceleration

Wakefield acceleration is a plasma-based acceleration, where the acceleration mechanism is based on the excitation of a plasma wave by an intense laser pulse (laser wakefield acceleration - LWA) or an electron beam (plasma wakefield acceleration - PWFA). The concept was originally put forward for consideration by T. Tajima and J. M. Dawson [10] in 1979 and first experimented by C. Joshi in 1984 [11]. It is demonstrated that plasma accelerators can generate billions of electron volts per metre. Currently, the wakefield machine at the Lawrence Berkeley National Laboratory is the strongest, by accelerating electrons up to 4.25 GeV over a 2 cm length [12]. The review by E. Esarey et al. [13] provides deep knowledge and discussion about the topic.

In LWA, the excitation of an underdense plasma by intense laser pulses is produced via the ponderomotive force associated with the pulse envelope (see Fig. 2.2). The plasma electrons are expelled from the region of high laser intensity. If the longitudinal length scale L_z of the pulse profile's gradient is approximately equal to the plasma wavelength λ_p, the ponderomotive force excites large amplitude plasma waves (called wakefields), offering high energy

gain [13].

In PWFA, a pair of electron bunches are sent through a plasma slab. The front bunch (drive bunch) pushes plasma electrons away, creating a so-called *blowout* (or *bubble*) regime (proposed in 2002 by A. Pukhov and J. Meyer-ter-Vehn [14], experimentally confirmed in 2004 by J. Faure et al. [15]), which consists of only positively charge ions. The plasma wakefield is created and accelerates the second bunch (trailing bunch) when the expelled electrons are pushed back in behind this bunch (see Fig. 2.3).

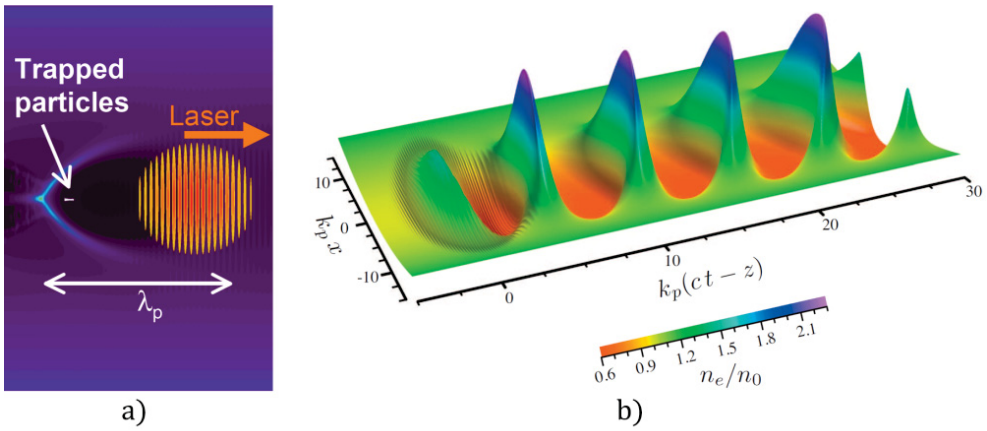

Figure 2.2: (a) Schematic of LWA. The illustration is taken from C. Geddes[16]. (b) The plasma wakefield excied by a Gaussian laser pulse. The figure is taken from E. Esarey et al. [13].

In 2014, SLAC's Facility for Advanced Accelerator Experimental Tests reported that a highly efficient technique for accelerating electrons [18]. The bunch contains a substantial charge and has a small energy spread. At CERN, scientists have been working on the AWAKE project to accelerate electron beams to the TeV energy regime using 400[GeV] proton beams from the Super Proton Synchrotron*. Having potential to be an affordable and compact accelerator, it is expected that once it reaches its full potential, the technology can

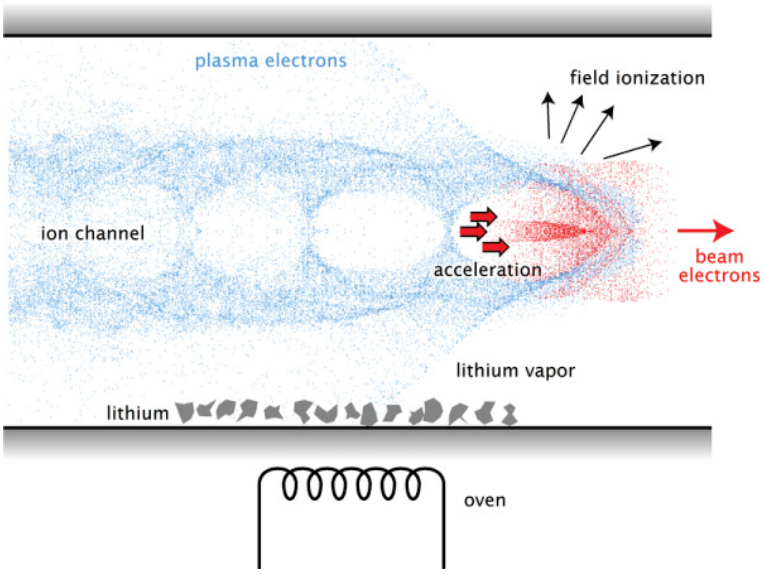

Figure 2.3: Schematic of bubble acceleration. The illustration is taken from N. Kirby et al. [17].

find its service in many laboratories, hospitals, industries and even security service, as a replacement for traditional RF accelerators.

2.3 Dielectric laser acceleration

The early concept for dielectric laser acceleration (DLA) was proposed by Y. Takeda and I. Matsui [19] in 1968 by exploiting the inverse Smith-Purcell effect [20] in metallic gratings. Due to the electrical breakdown of metals, the acceleration gradient was merely in the order of kiloelectronvolt per metre. On the other hand, it has been verified through experiments [21][22] that dielectric materials can endure stronger fields, one to two orders of magnitude, than metals.

To utilise the advantage of high laser damage thresholds and low Ohmic

*See: http://awake.web.cern.ch/awake/.

losses of dielectric materials [7], several DLA schemes have been proposed in recent years. For example, Fig. 2.4 shows the DLA proposal by Plettner et al. [23]. The scheme consists of two dielectric gratings separated by a vacuum channel. Two counter-propagating laser beams are sent into the channel from both sides. During the propagation inside the gratings, the electromagnetic waves will encounters an additional π-phase shift at the pillars, as depicted in the inset. After being injected into the structure, an electron beam will always experience the accelerating field.

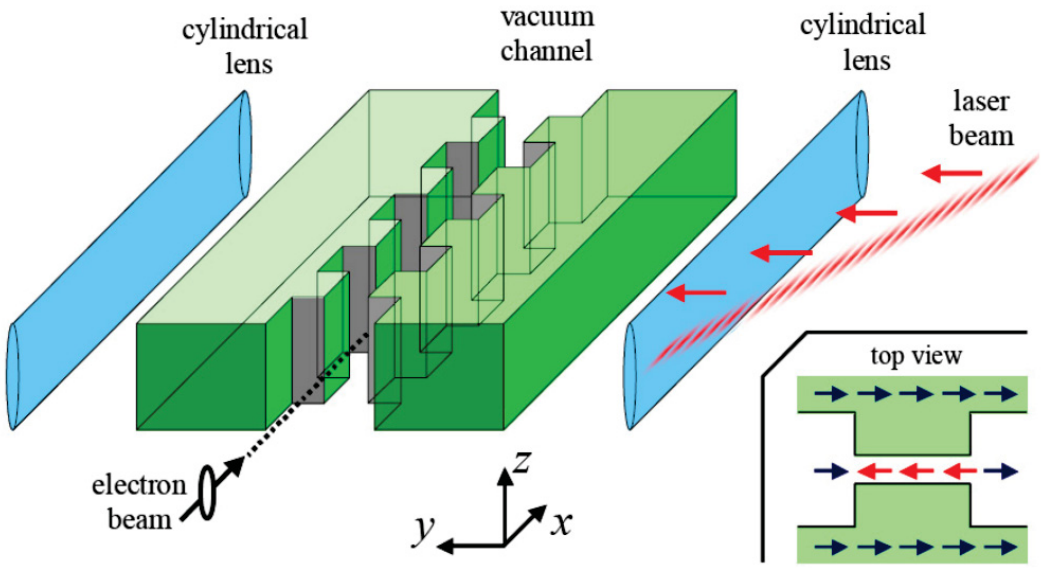

Figure 2.4: The DLA scheme with double dielectric gratings. The lasers are sent from both sides of the structure. The pillars will add a π-phase shift to the electromagnetic waves. The correctly injected particle beam will always harvest the accelerating field, as shown in the inset. The picture is taken from Plettner et al. [23]

Fig. 2.5 depicts the experiment setup and results performed at the Next Linear Collider Test Accelerator (SLAC) facility at the SLAC National Accelerator Laboratory [24]. The structure is 550 μm long, with period 800 nm ($\approx$ 687 optical periods) and gap 400 nm. The 60 MeV beam is focused by a

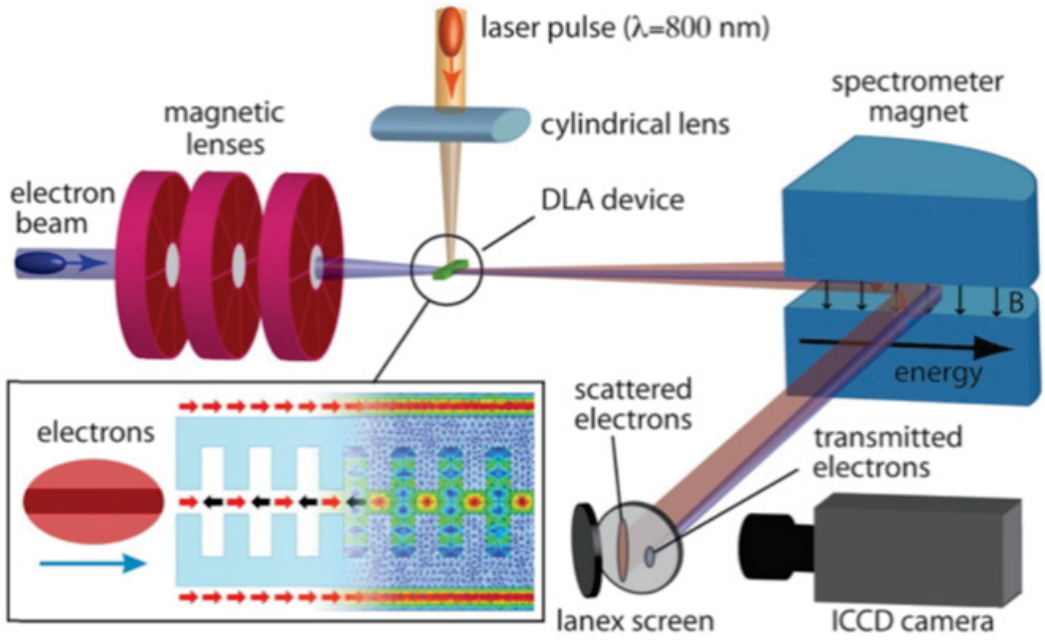

(a)

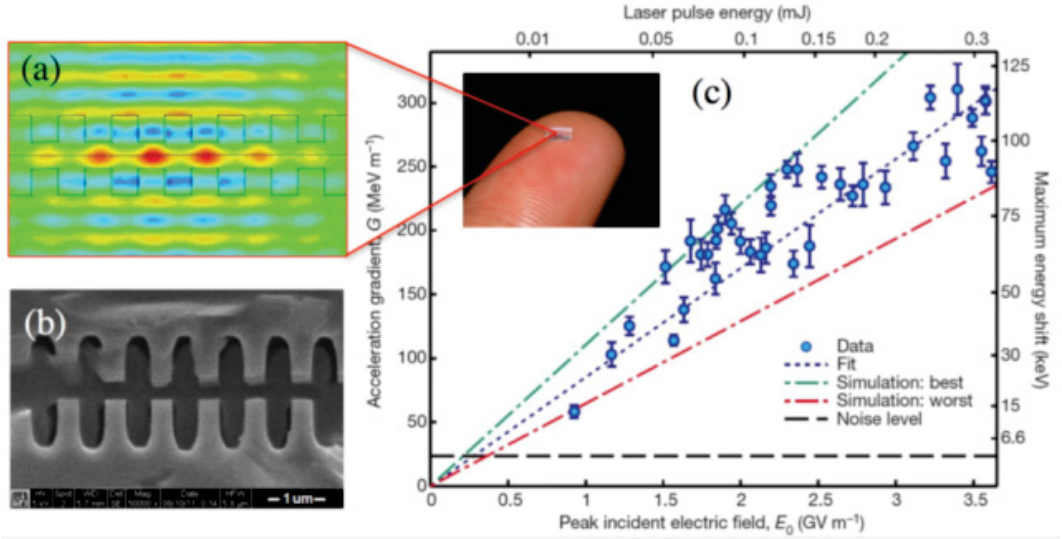

(b)

Figure 2.5: The SLAC Next Linear Collider Test Accelerator: (a) experimental setup; (b) an acceleration gradient of 300[MV/m] is achieved from experiments. The images are taken from [24].

permanent magnetic quadrupole triplet and then injected to the structure. It is reported that the acceleration gradient of 300 MV/m is achieved. Fig. 2.5b shows a sample of the structure, in comparison with human finger. Almost at the same time, J. Breuer and P. Hommelhoff reported a 25 MeV/m acceleration gradient for non-relativistic electron beam in a dielectric structure [25].

Based on these results, it is envisioned that a scalable and modular linear accelerator can be realised, which has a wide operation range: the machine can accelerate particles from non-relativistic to relativistic regime while does not occupy much area. Moreover, the structures can also be useful in ultrafast electron microscopy or electron diffraction experiments [26].

2.4 Ionisation

Ionisation is the process by which atoms or molecules lose electrons due to the interaction with external fields (e.g. laser pulses), known as optical field ionisation (OFI), or by collision with other particles. In this section, we recapitulate the principal formulae for the OFI process. On the other hand, we neglect the effect of the collisional ionisation since it is slow compared to the femtosecond pulse used in the simulations [27].

The behaviour of an ionisation process and the dependence of the ionisation probability on the ionisation potential and properties of an external field is quantified in the adiabatic parameter κ, published by Keldysh [28] in 1965. The Keldysh parameter is defined as the ratio between the frequency ω_0

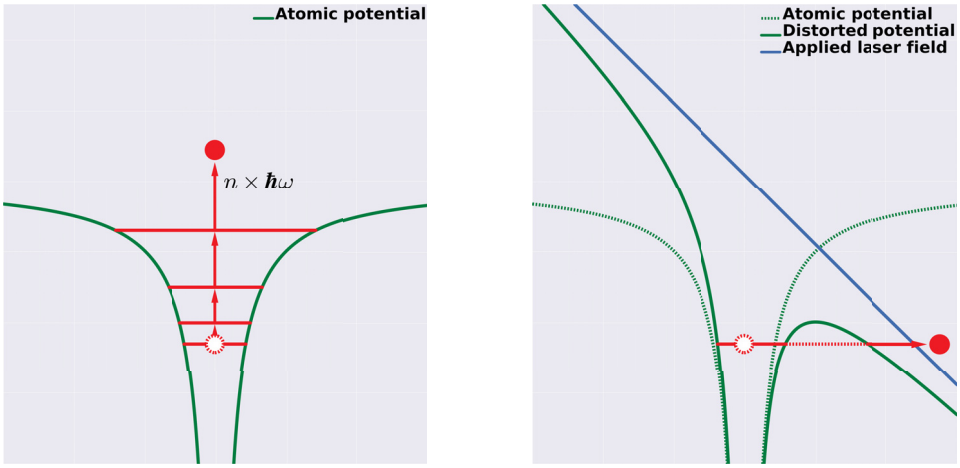

(a) Multi-photon ionisation (b) Tunnelling ionisation

Figure 2.6: Ionisation processes

of the laser beam and the frequency ω_t of an electron tunnelling through an ionisation potential barrier of an atomic level U_{ion} [29]

$$\kappa = \frac{\omega_0}{\omega_t} = \omega_0 \frac{\sqrt{2m_e U_{ion}}}{eE}. \tag{2.2}$$

Here, E is the electric field amplitude, e and m_e are the elementary charge and the electron mass, respectively. The Keldysh factor has two limiting cases:

- $\kappa \gg 1$: in this regime an electron will simultaneously absorb $N > 1$ photons (see Fig. 2.6a). Granted that the energy per laser photon is smaller than the ionisation potential, the total absorbed energy is high enough to facilitate electron's crossing the energy gap between the initial and final (ionised) states. This phenomenon is known as *multi-photon* or *weak-field* ionisation [30].

- $\kappa \ll 1$: under an intense laser field, the potential barrier of an atom (or molecule) is distorted drastically. As a consequence, the height of the

barrier is lowered and the length decreases. Thus, electrons can tunnel through the barrier and escape the atom (or molecule) easily (see Fig. 2.6b). This phenomenon is called *tunnelling* or *strong-field* ionisation, and is a quantum-mechanic event [30].

In our simulation, the ionisation potential U_{ion} is in between 20 eV and 120 eV at the early stage of the ionisation process. The laser intensity is about $I \approx 2 \times 10^{17}$ W/cm^2, we obtain from Eq. (2.2) $\kappa \approx 0.05$. Thus, we can neglect the effect of the multi-photon process. Moreover, the time step is usually smaller than the laser period and hence the laser field can be considered to be static at each time step. On the account of these conditions, we can safely use the formula for the tunnelling ionisation in a static field. According to Chen et al. [31], the tunnelling ionisation rate of complex atoms in a static field E is given by

$$W_{DClm} = \omega_a C^2_{n^*l^*} \frac{(2l+1)(l+|m|)!}{2^{|m|}(|m|)!(l-|m|)!} \times \left(\frac{U_{ion}}{2U_H}\right) \left[2\frac{E_a}{E}\left(\frac{U_{ion}}{U_H}\right)^{3/2}\right]^{2n^*-|m|-1} \times \exp\left[-\frac{2}{3}\frac{E_a}{E}\left(\frac{U_{ion}}{U_H}\right)^{3/2}\right]. \tag{2.3}$$

Here, $U_H = 13.6$ eV is Hydrogen's ionisation potential; $\omega_a = \alpha^3 c/r_e$ is the atomic unit frequency; $E_a = \alpha^4 m_e c^2/e r_e$; α and r_e are the fine structure constant and classical electron radius, respectively; l and m are the electron's quantum number and its projection; $n^* = Z\sqrt{U_H/U_{ion}}$ is the effective principal quantum number and n_0^* is the value for the ground state; $l^* = n_0^* - 1$ is the effective orbital number; Z is the ion charge number after ionisation. The coefficients $C_{n^*l^*}$, based on the Ammosov-Delone-Krainov (ADK) model [32],

are defined as

$$C^2_{n^*l^*} = \frac{2^{2n^*}}{n^*\Gamma(n^* + l^* + 1)\Gamma(n^* - l^*)}, \tag{2.4}$$

with the gamma function $\Gamma(t) = \int_0^\infty x^{t-1}e^{-x}dx$.

2.5 Emittance

One important property of a charged particle beam in a particle accelerator is the *emittance* (unit: mm × mrad). It quantifies the average area or volume spread of particles in the phase space. Unlike the physical dimensions, the beam emittance is an invariant quantity in the absence of dissipative or cooling forces [33]. In one dimension (the phase space consists only position x and momentum p), the root-mean-square (rms) emittance of a beam with N_e particles is defined as [34]

$$\epsilon_x = \sqrt{\langle x^2\rangle\langle p^2\rangle - \langle xp\rangle^2}, \tag{2.5}$$

where the rms beam size is defined as

$$\langle x^2\rangle = \sigma_x^2 = \frac{1}{N_e}\sum_j x_j^2, \tag{2.6}$$

and the rms beam angular divergence σ_p

$$\langle p^2\rangle = \sigma_p^2 = \frac{1}{N_e}\sum_j p_j^2, \tag{2.7}$$

and the rms correlation term

$$\langle xp \rangle = \frac{1}{N_e} \sum_j x_j p_j. \tag{2.8}$$

Often the beam energy varies in the accelerators and thus the emittance is no longer invariant. To retain the invariance property, we often use the normalised emittance ϵ_x^n which is defined as

$$\epsilon_x^n = \beta\gamma\epsilon_x. \tag{2.9}$$

Here, $\beta = v/c$ and $\gamma = 1/\sqrt{1 - v^2/c^2}$, with c is the speed of light. The normalised emittance defined in Eq. (2.9) is conserved during acceleration.

CHAPTER 3

Particle-in-Cell Algorithm

3.1 Introduction

In plasma physics, we typically encounter huge particle densities: ranging from 10^{12} cm^{-3} in laboratory plasmas to 10^{27} cm^{-3} in laser pellet fusion plasmas. The practicality of analytical approaches are limited in such scenarios. Pioneered by Buneman [35] and Dawson [36], the Particle-in-Cell (PIC) method has been developed over many decades [37][38][39] to become a powerful simulation tool to study plasma phenomena with full kinetic description. The PIC codes employ the concept of *macro-particle*. A macro-particle represents a smooth cloud of many real particles moving with the same velocity and has the same charge-to-mass ratio as in real plasmas [40].

In this chapter I will introduce the core concept of the PIC method. The chapter is organised as follows

- Section 3.2 features the finite difference time domain method to solve

the Maxwell's equations.

- Section 3.3 describes the algorithm to solve the particles' equation of motion.

- Section 3.4 explains the macro-particle representation of the phase space distribution and the current deposition in PIC code .

- Section 3.5 summarise the chapter and introduce several technical aspects of a PIC program.

3.2 Maxwell Solver

The Maxwell's equations in the CGS unit system are [41]

$$\nabla \cdot \mathbf{E} = 4\pi\rho, \tag{3.1}$$

$$\nabla \cdot \mathbf{B} = 0, \tag{3.2}$$

$$\nabla \times \mathbf{E} = -\frac{1}{c}\frac{\partial \mathbf{B}}{\partial t}, \tag{3.3}$$

$$\nabla \times \mathbf{B} = \frac{1}{c}\frac{\partial \mathbf{E}}{\partial t} + \frac{4\pi}{c}\mathbf{J}. \tag{3.4}$$

Here, $\mathbf{E}$ and $\mathbf{B}$ are the electric and magnetic fields, respectively; ρ is the charge density; $\mathbf{J}$ is the current density; c is the speed of light. The continuity equation can be obtained by combining Eqs. (3.1) and (3.4)

$$\frac{\partial \rho}{\partial t} + c\nabla \cdot \mathbf{J} = 0. \tag{3.5}$$

If the system under consideration satisfies the continuity equation and the Gauss' laws at the very beginning of the simulation, it will always conserve the charge. As a result, we can discard Eqs. (3.1) and (3.3) and only need to solve Eqs. (3.3) and (3.4) during the simulation.

In 1966, Yee introduced a finite-difference time-domain method (FDTD) to solve the time-dependent Maxwell's equations [42]. Tested over 45 years, the Yee's algorithm proves to be a robust and efficient technique with applications in various fields. The method employs the staggering scheme in space and the leapfrog integration in time.

Spatial discretisation: The Yee algorithm splits the simulation domain into cubical cells with grid steps Δx, Δy, and Δz in the x, y, and z axes, respectively. In each cell, electric field components are placed at the cell faces and magnetic field components are arranged along the cell edges*(see Fig. 3.1). A field component u evaluated at a discrete point in the grid can be represented by a set of integer numbers (i, j, k) as

$$u(i\Delta x, j\Delta y, k\Delta z) = u_{i,j,k}. \tag{3.6}$$

Then, we define the symmetric finite difference operators $\hat{d}_\alpha$ of a field component $u_{i,j,k}$ as follows

$$\hat{d}_x u_{i,j,k} = \frac{u_{i+1/2,j,k} - u_{i-1/2,j,k}}{\Delta x}, \tag{3.7}$$

$$\hat{d}_y u_{i,j,k} = \frac{u_{i,j+1/2,k} - u_{i,j-1/2,k}}{\Delta y}, \tag{3.8}$$

$$\hat{d}_z u_{i,j,k} = \frac{u_{i,j,k+1/2} - u_{i,j,k-1/2}}{\Delta z}. \tag{3.9}$$

*Placing all **E** and **B** components at the cell centre will give rise to the numerical errors and dispersion.

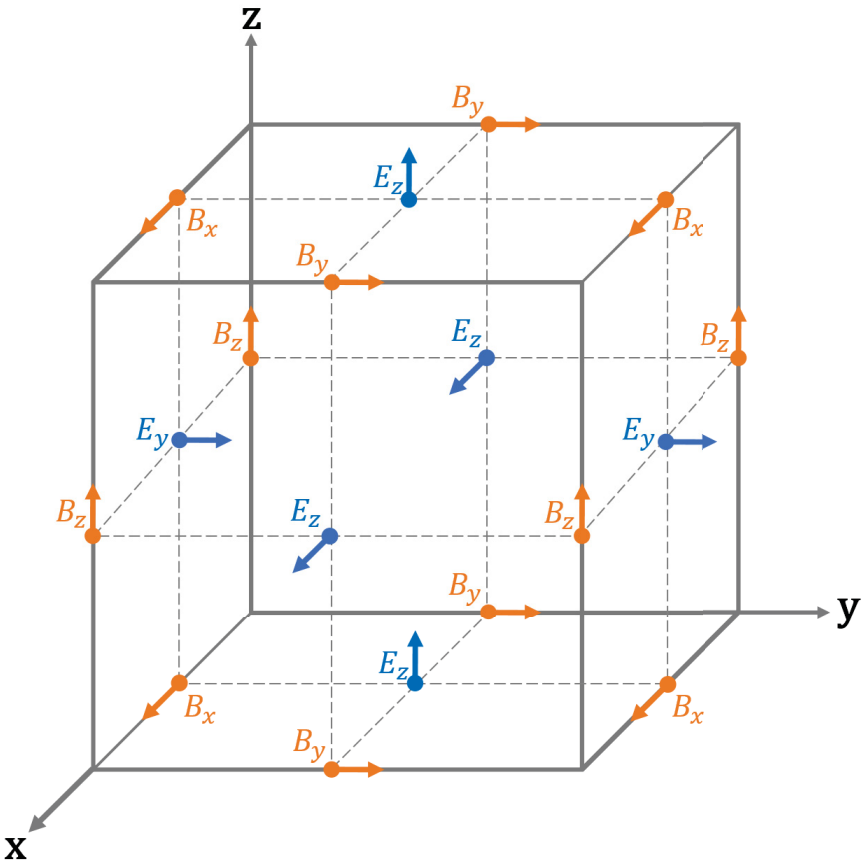

Figure 3.1: Structure of a Yee cell: electric field components are defined at the cell faces and magnetic field components are placed along the edges.

Then, the Maxwell's equations (3.3) and (3.4) are spatially discretised, based on the Yee grid, as

$$\begin{aligned}\nabla \times \mathbf{E} &= \begin{pmatrix} \hat{d}_y E_z|_{i+1/2,j,k} - \hat{d}_z E_y|_{i+1/2,j,k} \\ \hat{d}_z E_x|_{i,j+1/2,k} - \hat{d}_x E_z|_{i,j+1/2,k} \\ \hat{d}_x E_y|_{i,j,k+1/2} - \hat{d}_y E_x|_{i,j,k+1/2} \end{pmatrix} \\ &= -\frac{\partial_t}{c} \begin{pmatrix} B_x|_{i+1/2,j,k} \\ B_y|_{i,j+1/2,k} \\ B_z|_{i,j,k+1/2} \end{pmatrix} = -\frac{1}{c}\frac{\partial \mathbf{B}}{\partial t}, \end{aligned} \tag{3.10}$$

$$\begin{aligned}\nabla \times \mathbf{B} &= \begin{pmatrix} \hat{d}_y B_z|_{i,j+1/2,k+1/2} - \hat{d}_z B_y|_{i,j+1/2,k+1/2} \\ \hat{d}_z B_x|_{i+1/2,j,k+1/2} - \hat{d}_x B_z|_{i+1/2,j,k+1/2} \\ \hat{d}_x B_y|_{i+1/2,j+1/2,k} - \hat{d}_y B_x|_{i+1/2,j+1/2,k} \end{pmatrix} \\ &= \frac{\partial_t}{c} \begin{pmatrix} E_x|_{i,j+1/2,k+1/2} \\ E_y|_{i+1/2,j,k+1/2} \\ E_z|_{i+1/2,j+1/2,k} \end{pmatrix} + \frac{4\pi}{c} \begin{pmatrix} J_x|_{i,j+1/2,k+1/2} \\ J_y|_{i+1/2,j,k+1/2} \\ J_z|_{i+1/2,j+1/2,k} \end{pmatrix} \\ &= \frac{1}{c}\frac{\partial \mathbf{E}}{\partial t} + \frac{4\pi}{c}\mathbf{J}. \end{aligned} \tag{3.11}$$

Temporal discretisation In the Yee's algorithm, the field components **E** and **B** are temporally centred and interleaved in a so-called *leapfrog arrangement*,

as depicted in Fig. 3.2. According to Taflove et al. [43], the advantages of this approach are "central difference in nature and second-order accurate."

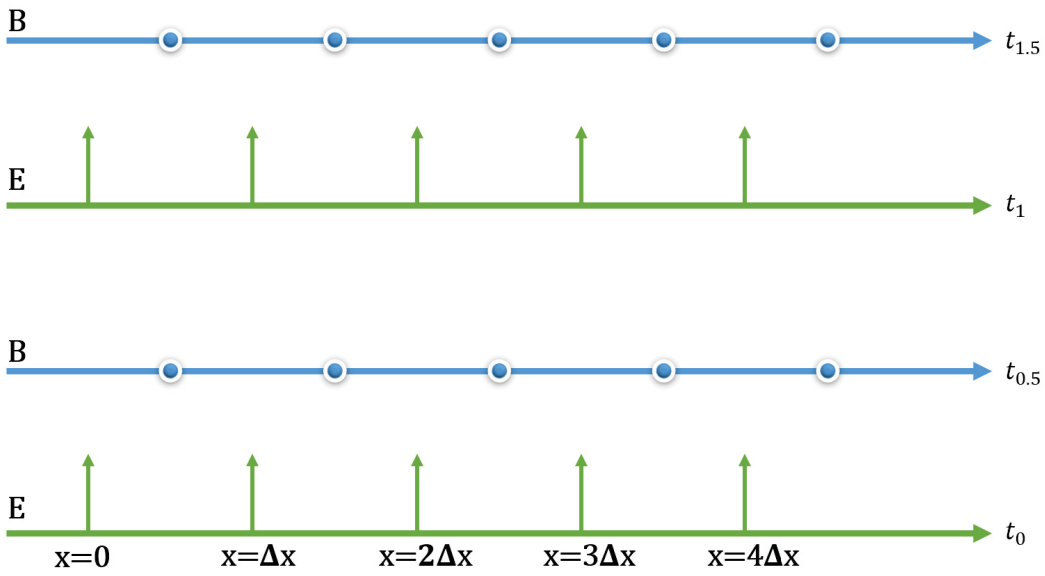

Figure 3.2: The location of the field components **E** and **B** in the Yee's algorithm: central difference in space and leapfrog in time.

In free space, the Maxwell's equations (3.3) and (3.4) can be rewritten in the form

$$\frac{1}{c}\frac{\partial}{\partial t}\begin{bmatrix} E_x \\ E_y \\ E_z \\ B_x \\ B_y \\ B_Z \end{bmatrix} = \begin{bmatrix} \frac{\partial B_z}{\partial y} \\ \frac{\partial B_x}{\partial z} \\ \frac{\partial B_y}{\partial x} \\ \frac{\partial E_y}{\partial z} \\ \frac{\partial E_z}{\partial x} \\ \frac{\partial E_x}{\partial y} \end{bmatrix} - \begin{bmatrix} \frac{\partial B_y}{\partial z} \\ \frac{\partial B_z}{\partial x} \\ \frac{\partial B_x}{\partial y} \\ \frac{\partial E_z}{\partial y} \\ \frac{\partial E_x}{\partial z} \\ \frac{\partial E_y}{\partial x} \end{bmatrix}. \tag{3.12}$$

which can be written in a more compact form

$$\frac{\partial \mathbf{u}}{\partial t} = \hat{M}\mathbf{u} + \hat{N}\mathbf{u}. \tag{3.13}$$

By applying the standard temporal Crank-Nicholson discretisation [44] to Eq. (3.13), we obtain

$$\frac{\mathbf{u}^{n+1} - \mathbf{u}^n}{\Delta t} = \frac{1}{2}\left(\hat{M}\mathbf{u}^{n+1} + \hat{M}\mathbf{u}^n\right) + \frac{1}{2}\left(\hat{N}\mathbf{u}^{n+1} + \hat{N}\mathbf{u}^n\right) + \mathcal{O}(\Delta t)^2. \tag{3.14}$$

Expanding and omitting high order terms in Eq. (3.14) yields

$$\left(1 - \frac{\Delta t}{2}\hat{M}\right)\left(1 - \frac{\Delta t}{2}\hat{N}\right)\mathbf{u}^{n+1} = \left(1 + \frac{\Delta t}{2}\hat{M}\right)\left(1 + \frac{\Delta t}{2}\hat{N}\right)\mathbf{u}^n, \tag{3.15}$$

which can be separated into two stages[†]

$$\begin{cases} \left(1 - \frac{\Delta t}{2}\hat{M}\right)\mathbf{u}^{n+1/2} &= \left(1 + \frac{\Delta t}{2}\hat{N}\right)\mathbf{u}^n \\ \left(1 - \frac{\Delta t}{2}\hat{N}\right)\mathbf{u}^{n+1} &= \left(1 + \frac{\Delta t}{2}\hat{M}\right)\mathbf{u}^{n+1/2}. \end{cases} \tag{3.16}$$

By combining the spatially discretised Maxwell's equations (3.10) and (3.11) and the temporal discretisation Eq. (3.16), we obtain the FDTD Maxwell solver used in the VLPL framework. The solver virtually involves three steps

$$\mathbf{B}^{n+1/2} = \mathbf{B}^n - \frac{\Delta t}{2}\nabla \times \mathbf{E}^n, \tag{3.17}$$

$$\mathbf{E}^{n+1} = \mathbf{E}^n + \Delta t \nabla \times \mathbf{B}^{n+1/2} - \Delta t \mathbf{J}^{+1/2}, \tag{3.18}$$

$$\mathbf{B}^{n+1} = \mathbf{B}^{n+1/2} - \frac{\Delta t}{2}\nabla \times \mathbf{E}^{n+1}. \tag{3.19}$$

[†]Detailed calculation can be found in Fomberg's article [44].

Stability condition of Yee's scheme The Yee's algorithm requires a specific relation between the time step Δt and grid steps Δx, Δy, and Δz [43]

$$c\Delta t\sqrt{\frac{1}{(\Delta x)^2}+\frac{1}{(\Delta y)^2}+\frac{1}{(\Delta z)^2}}\geq 1. \tag{3.20}$$

The violation of the condition (3.20) will cause the nonphysical wave dispersion: the speed of light in vacuum is smaller than c in the simulation domain.

3.3 Particle pusher

For a relativistic particle with mass m and charge q, the equation of motion reads

$$\mathbf{p}=\gamma m\mathbf{v}, \tag{3.21}$$

$$\mathbf{F}=\frac{d\mathbf{p}}{dt}. \tag{3.22}$$

Here, $\mathbf{p}$ and $\mathbf{v}$ are the momentum and velocity of the particle. The particle's Lorentz factor is given by

$$\gamma=\frac{1}{\sqrt{1-\frac{v^2}{c^2}}}. \tag{3.23}$$

Introducing $\mathbf{u}=\gamma v/c=\mathbf{p}/mc$, Eq. (3.22) becomes

$$\mathbf{F}=m\frac{d\left(\gamma\mathbf{v}\right)}{dt}=m\frac{d\mathbf{u}}{dt}. \tag{3.24}$$

In an electromagnetic field, the force $\mathbf{F}$ is the Lorentz force. Thus,

$$m\frac{d\mathbf{u}}{dt} = q\left(\mathbf{E} + \frac{\mathbf{v}\times\mathbf{B}}{c}\right). \tag{3.25}$$

The particle position $\mathbf{x}$ and momentum $\mathbf{u}$ can be found by solving the symplectic system of differential equations

$$\dot{\mathbf{u}} = \frac{\mathbf{F}}{m}, \tag{3.26}$$

$$\dot{\mathbf{x}} = \frac{\mathbf{u}}{\gamma}. \tag{3.27}$$

The leapfrog method can be used to solve the system (3.26) and (3.27) effectively: staggering $\mathbf{x}$ and $\mathbf{u}$ at discrete times (see Fig. 3.3) and using the temporal average for $\mathbf{u}^n$ to maintain the second-order accuracy

$$\mathbf{u}^n = \frac{\mathbf{u}^{n-1/2} + \mathbf{u}^{n+1/2}}{2}. \tag{3.28}$$

Hence, we obtain the implicit equations

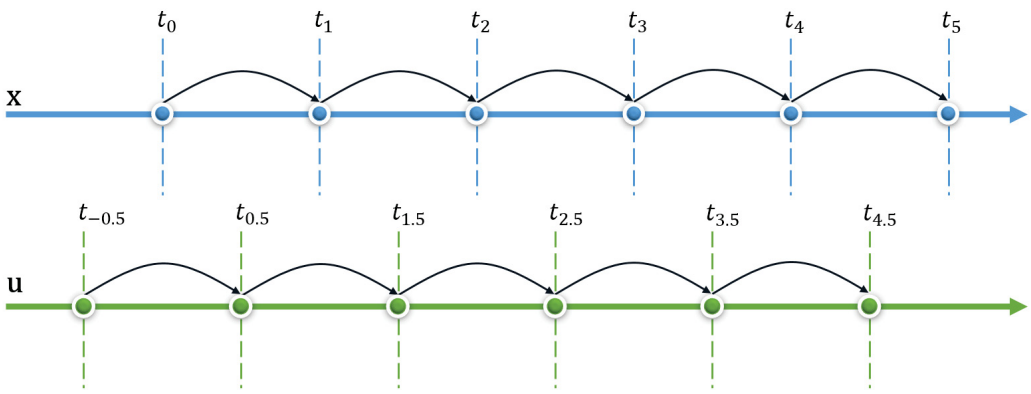

Figure 3.3: Chart of the leapfrog method: position $\mathbf{x}$ is evaluated at integral time-steps while momentum $\mathbf{u}$ is evaluated at half times.

$$\frac{\mathbf{x}^{n+1}-\mathbf{x}^{n}}{\Delta t}=\frac{\mathbf{u}^{n+1/2}}{\gamma^{n+1/2}}, \tag{3.29}$$

$$\frac{\mathbf{u}^{n+1/2}-\mathbf{u}^{n-1/2}}{\Delta t}=\frac{q}{mc}\left(\mathbf{E}^{n}+\frac{\mathbf{u}^{n+1/2}+\mathbf{u}^{n-1/2}}{2\gamma^{n}}\times\mathbf{B}^{n}\right). \tag{3.30}$$

Eqs. (3.29) and (3.30) can be solved by using high-order integration methods (e.g. Runge-Kutta). However, these methods often require a considerable amount of time, especially when there are many particles in the system. Instead, the implicit method proposed by Boris in 1970 [45] provides an efficient solution by decoupling the electric field push from the magnetic field push. By defining the relations

$$\mathbf{u}^{n-1/2}=\mathbf{u}^{-}-\frac{q\mathbf{E}^{n}}{2mc}\Delta t, \tag{3.31}$$

$$\mathbf{u}^{n+1/2}=\mathbf{u}^{+}+\frac{q\mathbf{E}^{n}}{2mc}\Delta t. \tag{3.32}$$

and inserting into Eq. (3.30), we have

$$\mathbf{u}^{+}-\mathbf{u}^{-}=\left(\mathbf{u}^{+}+\mathbf{u}^{-}\right)\times\frac{q\mathbf{B}}{2mc\gamma^{n}}dt. \tag{3.33}$$

Denoting $\mathbf{t}=q\mathbf{B}\Delta t/2mc\gamma^{n}$, Eq. (3.33) reduces to

$$\begin{aligned}\mathbf{u}^{+}-\mathbf{u}^{-}&=\left(\mathbf{u}^{+}+\mathbf{u}^{-}\right)\times\mathbf{t}\\ \Rightarrow\mathbf{u}^{+}-\mathbf{u}^{+}\times\mathbf{t}&=\mathbf{u}^{-}+\mathbf{u}^{-}\times\mathbf{t}.\end{aligned} \tag{3.34}$$

Eq. (3.34) is a linear system with the solution

$$\mathbf{u}'=\mathbf{u}^{-}+\mathbf{u}^{-}\times\mathbf{t}, \tag{3.35}$$

$$\mathbf{u}^{+}=\mathbf{u}^{-}+\mathbf{u}'\times\frac{2\mathbf{t}}{1+t^{2}}. \tag{3.36}$$

Collecting all equations together, the Boris method involves four steps to push the particle momentum:

Step 1: apply the first half of the electric field push

$$\mathbf{u}^{-} = \mathbf{u}^{n-1/2} + \frac{q\mathbf{E}^n}{2mc}\Delta t. \tag{3.37}$$

Step 2: calculate the mid term $\mathbf{u}'$

$$\mathbf{u}' = \mathbf{u}^{-} + \mathbf{u}^{-} \times \mathbf{t}, \tag{3.38}$$

$$\mathbf{t} = \frac{q\mathbf{B}}{2mc\gamma^n}\Delta t. \tag{3.39}$$

Step 3: apply the magnetic field push (rotation).

$$\mathbf{u}^{+} = \mathbf{u}^{-} + \mathbf{u}' \times \frac{2\mathbf{t}}{1+t^2}. \tag{3.40}$$

Step 4: apply the second half of the electric field push.

$$\mathbf{u}^{n+1/2} = \mathbf{u}^{+} + \frac{q\mathbf{E}^n}{2mc}\Delta t. \tag{3.41}$$

The particle position can be easily obtained from the new momentum $\mathbf{u}^{n+1/2}$

$$\begin{aligned}\mathbf{x}^{n+1} &= \mathbf{x}^n + \frac{\mathbf{u}^{n+1/2}}{\gamma^{n+1/2}}\Delta t \\ &= \mathbf{x}^n + \frac{\mathbf{u}^{n+1/2}}{\sqrt{1+\left(\mathbf{u}^{n+1/2}\right)^2}}\Delta t\end{aligned} \tag{3.42}$$

3.4 Macro-particles

The relativistic Vlasov equation, which describes the temporal evolution of the distribution function $f(\mathbf{x}, \mathbf{p}, t)$ of plasma, reads [46]

$$\frac{\partial f}{\partial t} + \frac{\mathbf{p}}{m\gamma} + \frac{\mathbf{F}}{m}\nabla_p f = \mathrm{St}. \tag{3.43}$$

Here, St is the collisional term. In combination with the Maxwell's equations, the Vlasov equation 3.43 provides the complete information about plasma behaviour. The PIC algorithm operates on the basis that the particle distribution function is decomposed into many macro-particles in the phase space

$$\begin{aligned} f(\mathbf{x}, \mathbf{p}, t) &= \sum_{i=1}^{N} f_i(\mathbf{x}_i, \mathbf{p}_i, t) \\ &= \sum_{i}^{N} W_i S_{\mathbf{x}}(\mathbf{x} - \mathbf{x}_i) S_{\mathbf{p}}(\mathbf{p} - \mathbf{p}_i), \end{aligned} \tag{3.44}$$

where W_i is the weight of the i^{th} macro-particle; $S(\mathbf{x}_i, \mathbf{p}_i, t)$ is the shape function which describes the macro-particle's extension in phase space. It is required that S has to satisfy the identity

$$\int_{-\infty}^{+\infty} S(\mathbf{x}, t) d\mathbf{x} = 1. \tag{3.45}$$

Typically the shape function for momentum $S_{\mathbf{p}}$ is chosen to be Dirac delta function

$$S_{\mathbf{p}}(\mathbf{p} - \mathbf{p}_i) = \delta(\mathbf{p} - \mathbf{p}_i). \tag{3.46}$$

while the counterpart for position $S_{\mathbf{x}}$ is defined to be separable

$$S_{\mathbf{x}}\left(\mathbf{x}-\mathbf{x}_i\right)=S\left(x-x_i\right)S\left(y-y_i\right)S\left(z-z_i\right). \tag{3.47}$$

and each component has a flat-top profile

$$S(x)=\begin{cases}1, & |x|<\frac{1}{2}\\ 0, & \text{otherwise}\end{cases}. \tag{3.48}$$

To compute the force acting on the n-th particle $(\mathbf{x}_n, \mathbf{p}_n)$, the fields obtained

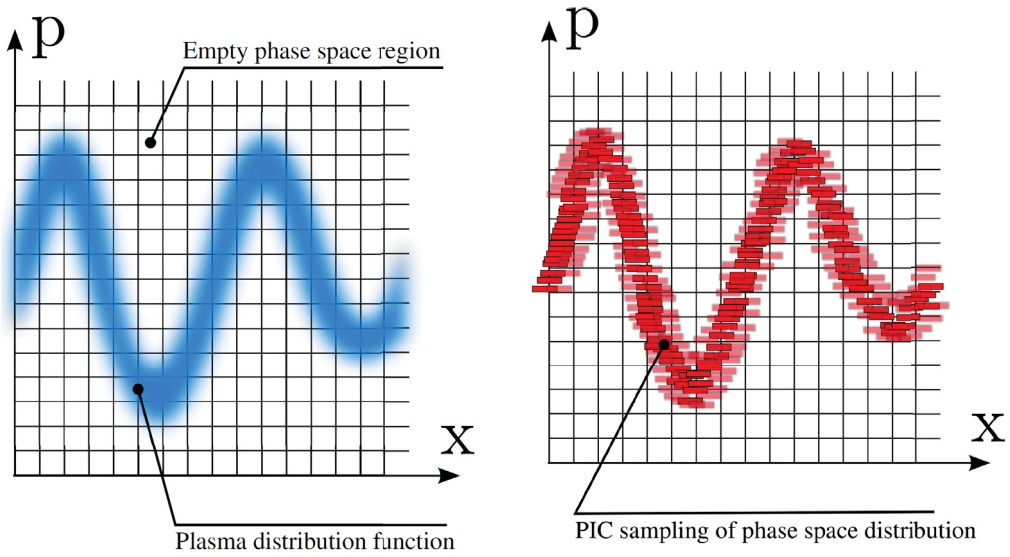

Figure 3.4: Plasma phase space distribution: (a) Represented by Vlasov's equation (3.43); (b) Rendered with macro-particles in PIC algorithm. The images are taken from T. Tückmantel [47].

from Yee's algorithm must be interpolated at the particle's position

$$E_n=\sum_{i\in\Gamma}E_iS(\mathbf{x}_n-\mathbf{x}_i). \tag{3.49}$$

Here, Γ denotes a group of Yee cells surrounding the particle. Fig. 3.5 shows an example of linear interpolation scheme for the electric field. Then, we deposit

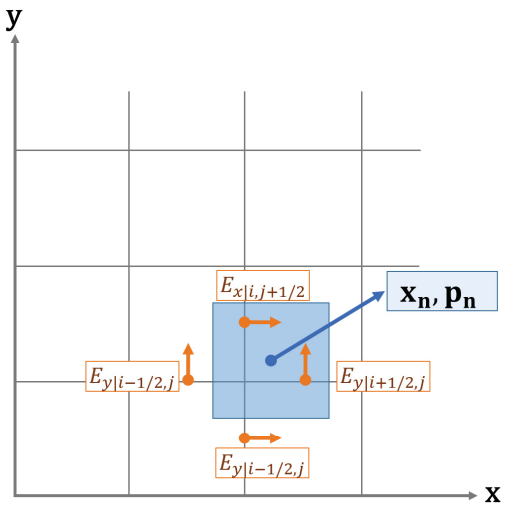

Figure 3.5: To push a particle, the field values from Yee cells are interpolated at the particle's centre of mass.

the current induced by the particle's motion to the grid cells

$$J^x_{i,j+1/2,k+1/2} = \delta x W_n (a_y^+ a_z^+ + b_{yz}), \tag{3.50}$$

$$J^y_{i+1/2,j,k+1/2} = \delta y W_n (a_z^+ a_x^+ + b_{zx}), \tag{3.51}$$

$$J^z_{i+1/2,j+1/2,k} = \delta z W_n (a_x^+ a_y^+ + b_{xy}), \tag{3.52}$$

$$J^x_{i,j-1/2,k+1/2} = \delta x W_n [(1 - a_y^+) a_z^+ - b_{yz}], \tag{3.53}$$

$$J^x_{i,j+1/2,k-1/2} = \delta x W_n [a_y^+ (1 - a_z^+) - b_{yz}], \tag{3.54}$$

$$J^x_{i,j-1/2,k-1/2} = \delta x W_n [(1 - a_y^+)(1 - a_z^+) - b_{yz}], \tag{3.55}$$

$$J^y_{i+1/2,j,k-1/2} = \delta y W_n[(1-a_z^+)a_x^+ - b_{zx}], \tag{3.56}$$

$$J^y_{i-1/2,j,k+1/2} = \delta y W_n[a_z^+(1-a_x^+) - b_{zx}], \tag{3.57}$$

$$J^y_{i-1/2,j,k-1/2} = \delta y W_n[(1-a_z^+)(1-a_x^+) - b_{zx}], \tag{3.58}$$

$$J^z_{i-1/2,j+1/2,k} = \delta z W_n[(1-a_x^+)a_y^+ - b_{xy}], \tag{3.59}$$

$$J^z_{i+1/2,j-1/2,k} = \delta z W_n[a_x^+(1-a_y^+) - b_{xy}], \tag{3.60}$$

$$J^z_{i-1/2,j-1/2,k} = \delta z W_n[(1-a_x^+)(1-a_y^+) - b_{xy}], \tag{3.61}$$

where $(\delta x, \delta y, \delta z)$ denote the particle's displacement; for $\alpha, \beta = \{x, y, z\}$

$$a_\alpha = 1 - 2\frac{x_\alpha + 0.5\Delta_\alpha}{\Delta_\alpha}, \tag{3.62}$$

$$b_{\alpha\beta} = \frac{1}{12}\Delta x_\alpha \Delta x_\beta. \tag{3.63}$$

3.5 Particle-in-Cell algorithm

Collecting all steps together, we have a complete computational cycle of the PIC algorithm (see Fig. 3.6) as follows

- The plasma phase space distribution is represented by a set of macro-particles with position $\mathbf{x}_n$ and momentum $\mathbf{p}_n$.
- The simulation domain is spatially discretised and the electromagnetic fields $\mathbf{E}$ and $\mathbf{B}$ are obtained by solving Maxwell's equations.
- The field values are then interpolated to particles' position in order to solve the equations of motion. The particle pusher module can be ex-

tended to include other interesting effects like ionisation or photon generation.

- Generate the currents due to particles' displacement and deposit them to the grid cells.

- Proceed to the next time step.

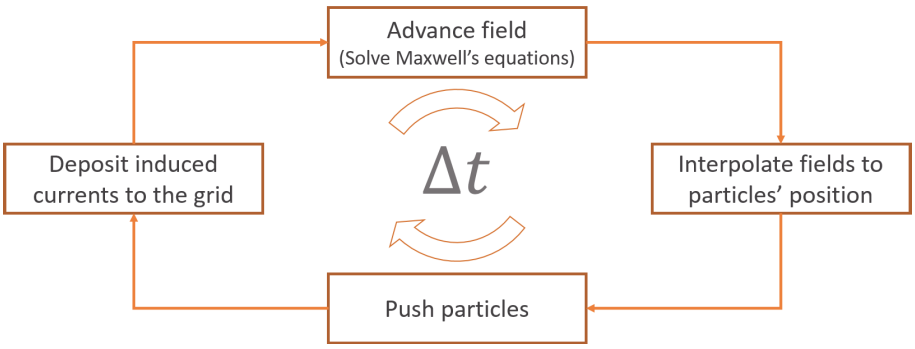

Figure 3.6: A computational cycle of the PIC algorithm.

Depending on the grid steps, a simulation can contain from several hundred to millions grid cells. To handle this kind of increase and to utilise the clusters' computing resources, the simulation domain is often partitioned into smaller grids which are then passed to different processes. The subdomains then can run as separate simulations (see Fig. 3.7). While being separated, the processed must be controlled by an interface for management of simulation consistency. In the VLPL code, we use OpenMPI[†] to keep track of processes' activities.

After one computation time step, the processes will communicate with each other. To avoid the mismatches that might occur during runtime, two or more guard cells are added to each subdomain (see Fig. 3.8). Data can

be transferred by mean of accessing information stored in the guard cells. In VLPL, the data storage is handled by the HDF5 model[‡].

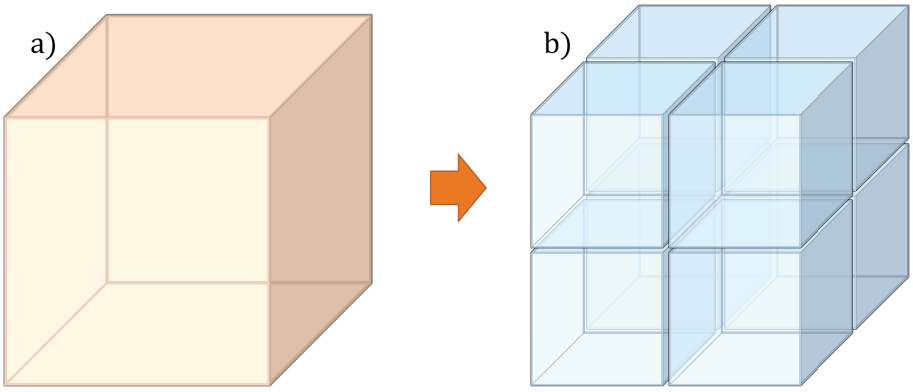

Figure 3.7: Parallelisation in PIC programs: An original simulation domain (a) is partitioned into several sub-domains (b) which are then passed to different processes.

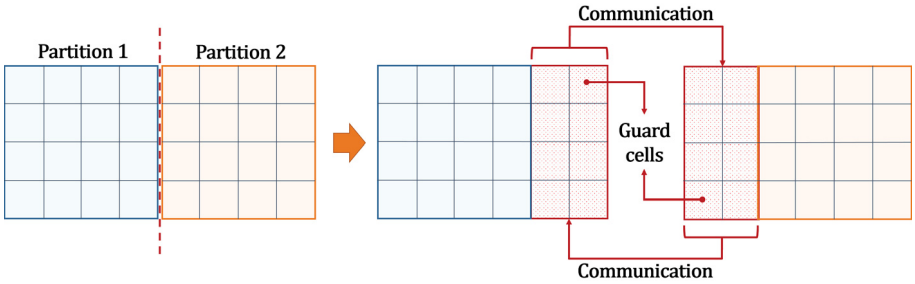

Figure 3.8: The communication bridges between partitions are established by adding guard cells to each subdomain. Their main tasks are to maintain the local boundary conditions and store information from adjacent partitions.

[†]Open Message Passing Interface. See webpage http://www.open-mpi.de/ for more detail.

[‡]Hierarchical Data Format. See webpage https://www.hdfgroup.org/HDF5/ for more detail.

CHAPTER 4

Electron Acceleration Scheme based on Periodic Structures

4.1 Introduction

In Chapter 1, we have discussed about the Lawson-Woodward theorem and several scenarios to violate it. Before going further, we revisit the situation where an electron travelling in vacuum across a transverse laser field. As we already know that the particle gets accelerated in one half of the laser oscillation and decelerated in the other half. If we desire to accelerate particles, we need to restrict the interaction length between the laser and the particle. This requirement can be fulfilled by inserting a kind of field obstruction during the decelerating phase. Expectedly, the electron only experiences the accelerating field in one laser cycle (see Fig. 4.1). This is the constitution concept of the electron acceleration scheme presented in this chapter.

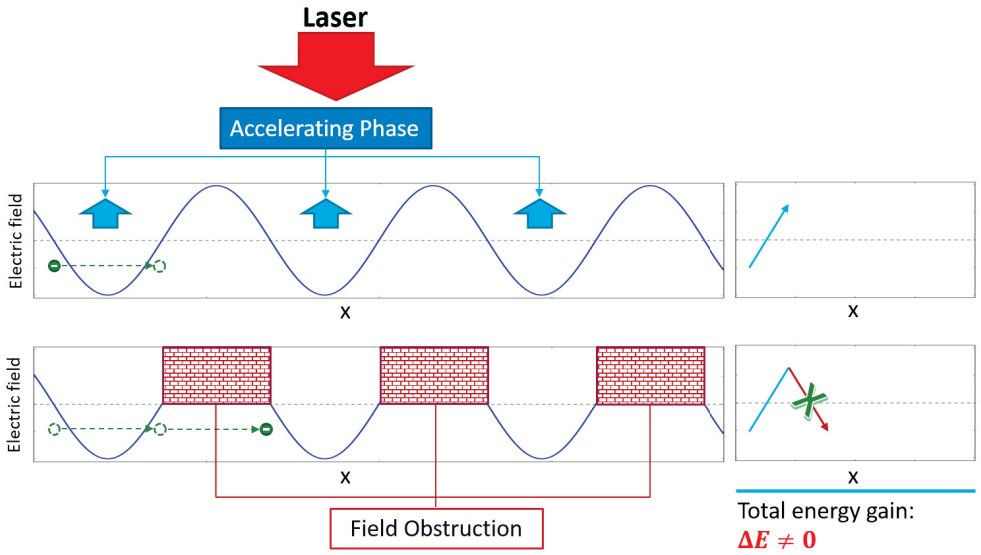

Figure 4.1: To accelerate particles, we need to limit the interaction length between the particles and the laser beams, especially during the decelerating phase. This can be done by the introduction of a field obstruction.

Section 4.2 explains in great detail the operational design of the acceleration scheme. In section 4.3 we discuss several aspects and experimental requirements concerning the scheme.

4.2 The scheme design

Fig. 4.2 shows the design of the periodic structure for electron acceleration. Here, (1) encapsulates one structure period, which consists of shielding blocks (2) and two pairs of lasers (3).

A shielding block is a rectangular cuboid with length l and thickness (width and height) w, whose main task is to impede the laser propagation. A cylindrical hole with diameter d_0 is drilled through the block to allow particles' propagation (see Fig. 4.2c). Each block is separated from each other such that

the gap between two consecutive blocks is half laser wavelength λ_0 long. The gap length ensures that the particles will interact with the laser field only in half oscillation period. Thus, they are either accelerated or decelerated, not both. The blocks are positioned along the particles' propagation direction (e.g. x-axis).

In the transverse plane (e.g. yz-plane), two pairs of laser beams (one along y- and one along z-axis) are provided at each gap. The laser beams counter-propagate in their corresponding axes and are focused at the centre of the gap (see Fig. 4.2b). This geometry of lasers guarantees a symmetric formation of the field in the gap. In consequence, when travelling through the gap, the particles will experience a strong accelerating and balanced field such that they are not pushed towards any particular direction but are maintained equally inside the block hole. There is also another requirement imposed on the laser configuration. The lasers at later periods must be temporally shifted backwards such that the particles will always experience the same field at every structure period. Thus, the pairs (4) in Fig. 4.2a are intendedly faded to indicate the temporal shift. Fig. 4.3 shows the electric field component E_X obtained from a self-consistent simulation. The right pairs appear to be weaker than the left counterpart since they arrive at the structure at a later time.

Before being injected into the acceleration structure, the particle beam will have to pass through magnetic lens to ensure that the beam remains in the centre of the structure gap. Usually the beam diameter might be larger than that of the gap. In this case, many particles will collide with the structure and

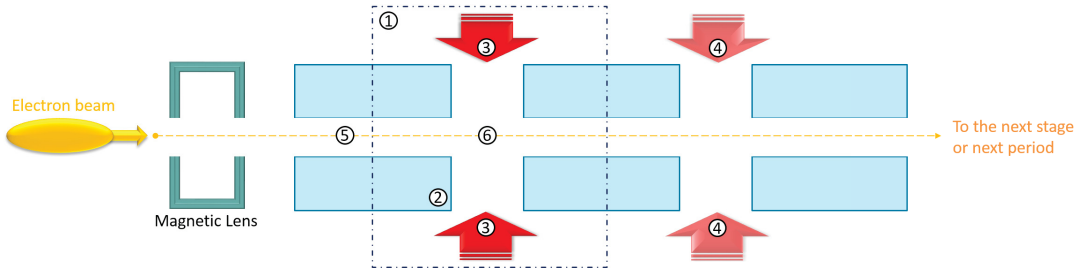

(a) The schematic design of the periodic structure for electron acceleration. Here, ① encapsulates one structure period and ② is the shielding structure. ③ and ④ represent the laser beams, where ④ appear faded since they are delayed in time. ⑤ and ⑥ describe main regions during particles' propagation inside the structure.

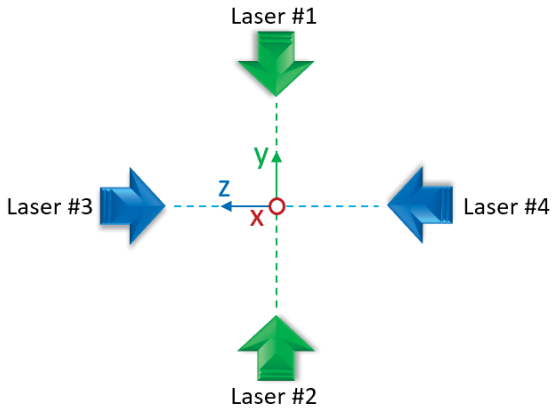

(b) The laser setup at each gap. The four laser beams are focused at the centre of the gap, which will intendedly provide a strong field for electron acceleration.

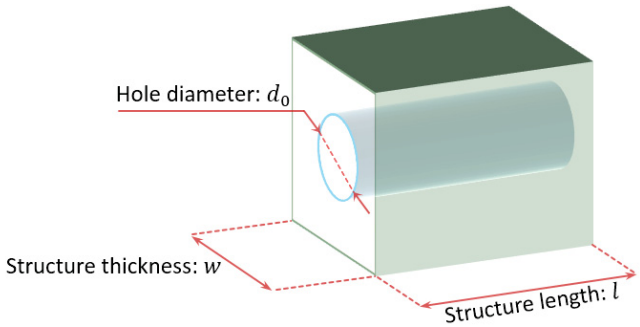

(c) The parameter detail of the shielding structure.

Figure 4.2: The design, laser setup, and parameter detail of the periodic structure for electron acceleration.

get lost while the others pass through and enter the structure. Due to this reason, it is recommended to build the first shielding block longer so that the effect caused by the beam impact does not affect the acceleration performance.

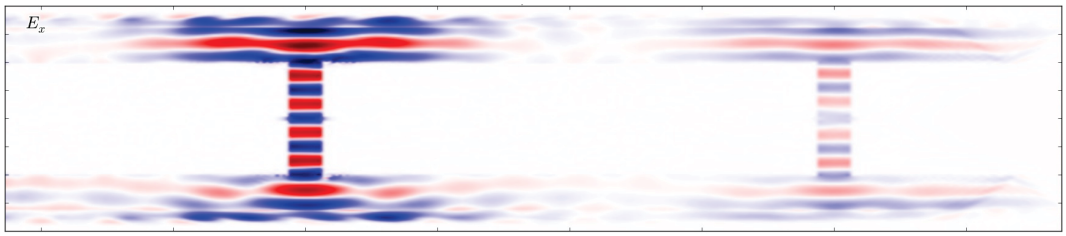

Figure 4.3: The electric field component E_X in the acceleration scheme obtained from a self-consistent simulation (see next chapter). The right pairs are delayed in time thus they appear to be weaker than the left counterpart.

Throughout the operating time of the acceleration scheme, there are mainly two regions of interest, namely the shielded region (5) and the open region (6) (see Fig. 4.2a). Fig. 4.4 shows the expected evolution of an electron propagating in the structure. In the shielded region, the particles are exempt from the interaction with the lasers, since the shielding block prevents them from penetrating inside. Accordingly, the particles' momenta remain constant in this region, as depicted with the straight lines in Fig. 4.4. Subsequently, the particles cross the extent of the gap and travel in the gap. In this open region, the field is building up intensely. Assumed that the injection is at the right phase, the particles can extract energy from the field and thus the momenta increase. The outcome of this region is depicted as the steep slopes in Fig. 4.4. The laser phase will eventually change side. When it happens, the particles are already at the other end of the gap and entering the next shielding block.

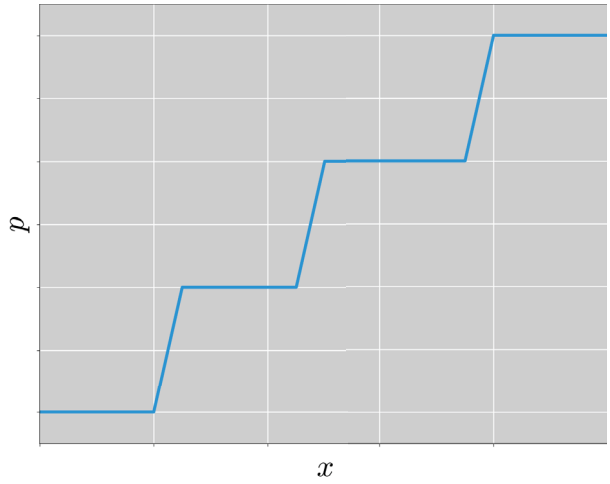

Figure 4.4: The expected phase space evolution of an electron travelling in the acceleration structure. The particle's momentum will remain constant when propagating in the hole and increase when travelling in the open gap.

Although the energy gain per period might be small, the particles will propagate through hundreds of periods and thus small gains will aggregate into huge total energy upsurge at the end of the structure. Moreover, by adjusting the temporal shifts for the laser and/or the length of the blocks, the structure can be constructed and assembled in a multi-stage acceleration process.

In this scheme, the electron acceleration is realised based on the *direct* interaction between the laser pulses and particles. Hence, we can also name it the direct laser acceleration, in contrast to plasma-based acceleration.

4.3 Other aspects

Analogy with dielectric laser acceleration: The direct laser acceleration proposed in this chapter does not rely on the laser phase shift during the

propagation inside the structure since it is difficult to control. Moreover, we aim for single-shot scenarios with intense laser pulses to achieve higher acceleration gradient. Thus, the material damages may not pose a serious concern as in the dielectric scheme.

Half-period Fabry-Perot structure: The original accelerating design was the half-period Fabry-Perot structure [48] shown in Fig. 4.5. Contrary to the open structure presented in section 4.2, the gaps in the Fabry-Perot design are formed into micro-cavities with length L, where one side is covered by a layer of thin foil being partially transparent to laser beams and the other is closed to reflect radiation. The main task of the micro-cavity is to enhance the laser field. The field enhancement factor can be estimated by

$$M = \frac{E_c}{E_0} \approx \frac{1}{1-R}, \tag{4.1}$$

where E_c is the field in the cavity, E_0 is the laser field, and R is the reflectivity of the thin foil. According to [49], the cavity field can be amplified from the pump laser manifold. Fig. 4.6 shows the field enhancement factor M against the cavity length L for the case the thin foil thickness is $d_{tf} = 0.02\lambda_0$ and $\lambda_0 = 800$ nm. The maximised value is $M = 59.48$ for $L = 0.4792\lambda_0$. That is, the resonant field E_c can be expectedly 60 times higher than the original field E_0. However, this design has several disadvantages.

- For this design, it is required that the laser intensity must be moderate to maintain the structure's integrity during the interaction. It

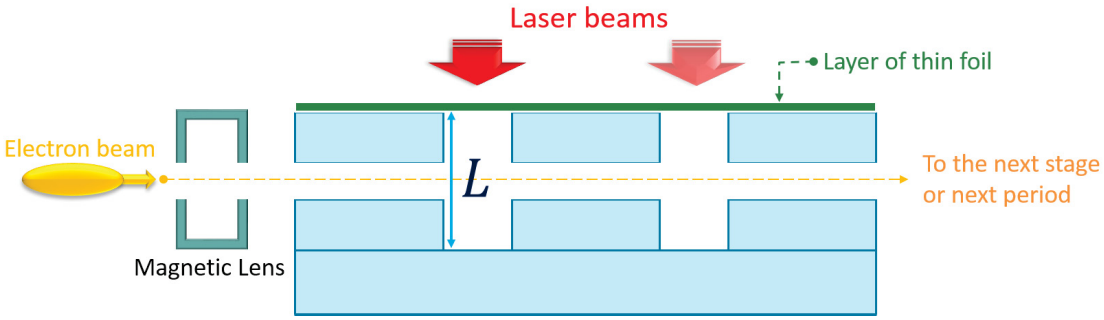

Figure 4.5: The schematic design of the Fabry-Perot resonator accelerating structure. A layer of thin film being partially transparent to laser beams is used to cover one side of the gap. The other side is closed by a reflective wall. The gap is then formed into a micro-cavity with length L.

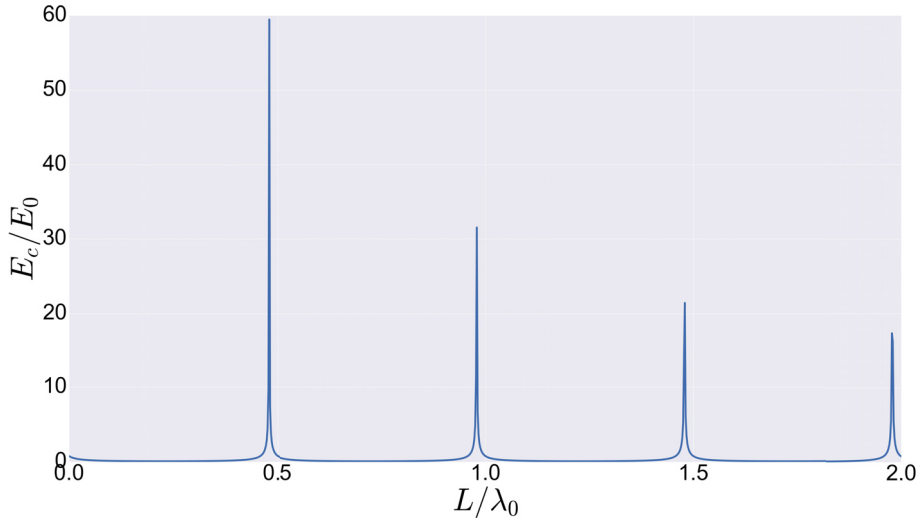

Figure 4.6: The field enhancement factor M against the cavity length L in the half-period Fabry-Perot accelerating structure. The thin foil is assumed to have thickness $d_{tf} = 0.02\lambda_0$, for $\lambda_0 = 800$ nm.

is shown that the whole structure can sustain lasers with intensities as high as 10^{14} W/cm^2 [48]. In spite of high finesse, we cannot exploit higher intensity laser that are available on the market. This limitation would greatly bring down the performance of the scheme.

- In order to achieve the highest finesse as possible, the cavity length and thin foil thickness must be precisely produced at tiny scale. Any small deviation can undermine the cavity's quality. This restriction can cause a lot of pressure on the manufacturing process.
- The thin foil can be easily damaged due to the interaction with the incoming laser field or the resonant field. This can also degrade the finesse of the cavity.

In contrast, the open structure presented in section 4.2 can operate with laser intensities as high as 10^{17} W/cm^2 (see next chapter). Moreover, the accelerating field of the open structure does not rely on the property of the cavity and thus the flexibility of the design is greatly expanded. On account of these reasons, the development of the resonant design is terminated.

Producing structures for experiments The size of the structure is normally in nano-scale. For this range, the 3D-printing approach is much favoured. For example, in early February 2016 (at the time of writing this thesis), a group of scientists at the Karlsruhe Institute of Technology, Germany published their findings in Nature Materials [50], in which they created a glassy carbon nano-lattice with single struts shorter than 1 μm and diameters as small as 200 nm. To produce such a lattice, the team make use of a 3D printing technique, so called *two-photon direct*

laser writing or *direct-write laser lithography*. After 3D printing process is finished, the pyrolysis process is utilised to shrink the lattice by 80% to resolve even a smaller lattice. Such technology is expensive for the time being but will expectedly go down in price in the near future.

Laser requirement The coherency between laser pulses is of utmost importance in our acceleration scheme. For typical laser systems, maintaining the coherency for two pulses is already a laborious task, leave alone for a dozen of lasers. However, the emergence of the Coherent Amplification Network (CAN) fibre laser system [51] provides a prospective possibility to realise the periodic laser-based electron acceleration. Fig. 4.7 shows the CAN's operating principle. The most significant property of the CAN system is *massive parallelism*: a huge number of identical and mutually coherent laser pulses can be created from a vast fibre array.

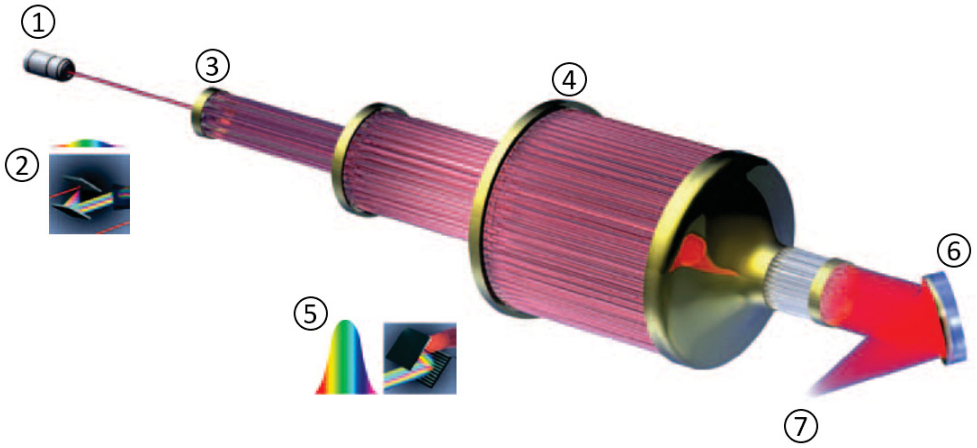

Figure 4.7: The operating system of the Coherent Amplification Network (CAN): the seed laser pulse (1) is stretched (2), then split and amplified in many fibre channels (3). The process is repeated several times (4). All the channels are combined, compressed (5) and focused (6) coherently to produce the final pulse (7). The image is taken from [51].

CHAPTER 5

Simulation Results on Electron Acceleration

In the previous chapter, I have described in detail the design of the new electron acceleration scheme based on the periodic structure and the functionalities of its components. In this chapter lies the major part of my work: conducting the simulation to test the performance and practicality of the scheme. The simulation results are presented in the following order:

- Section 5.1 contains the parameter list for conducting the simulations.
- In section 5.2, I study the ionisation process of the periodic structure and the effect of the hole diameter on the field.
- Section 5.3 shows the main simulation results.

Finally, in section 5.4 I summarise the works done in this chapter and discuss other characteristic points.All the simulations presented here are obtained by using the VLPL code [38].

Parameter	Notation	Value	Unit
	General Settings		
Wavelength	λ_0	0.8×10^{-4}	cm
Boxlength	$x \times y \times z$	$16 \times 8 \times 8$	λ_0
Gridstep	$dx \times dy \times dz$	$0.05 \times 0.05 \times 0.05$	λ_0
Timestep	dt	0.01	λ_0/c
Number of particles per cell		10	
	Structure Settings		
Element		Silicon	
Hole diameter	d_0	0.2	λ_0
Thickness	w	4	λ_0
Length	l	7.5	λ_0
Number of periods		12	
	Laser Settings		
Beam diameter		2	λ_0
Pulse duration		30	fs
Temporal delay		10	λ_0/c
	Electron Beam Settings		
Initial Lorentz factor	γ_i	1000	
Beam length		8	λ_0
Initial bunch charge	Q_i	318.37	fC

Table 5.1: The simulation parameters for electron acceleration scheme in periodic structures.

5.1 Parameter settings

The parameter settings for the electron acceleration simulations are listed in Table 5.1. The laser wavelength is assumed to be $\lambda_0 = 0.8 \times 10^{-4}$ cm. The simulation box has a three dimensional planar geometry with lengths $16\lambda_0 \times 8\lambda_0 \times 8\lambda_0$ and gridsteps $0.05\lambda_0 \times 0.05\lambda_0 \times 0.05\lambda_0$ in $x-$, $y-$, and $z-$axes. The timestep is chosen to be $dt = 0.01\lambda_0/c$. Each cell has eight numerical particles for every species.

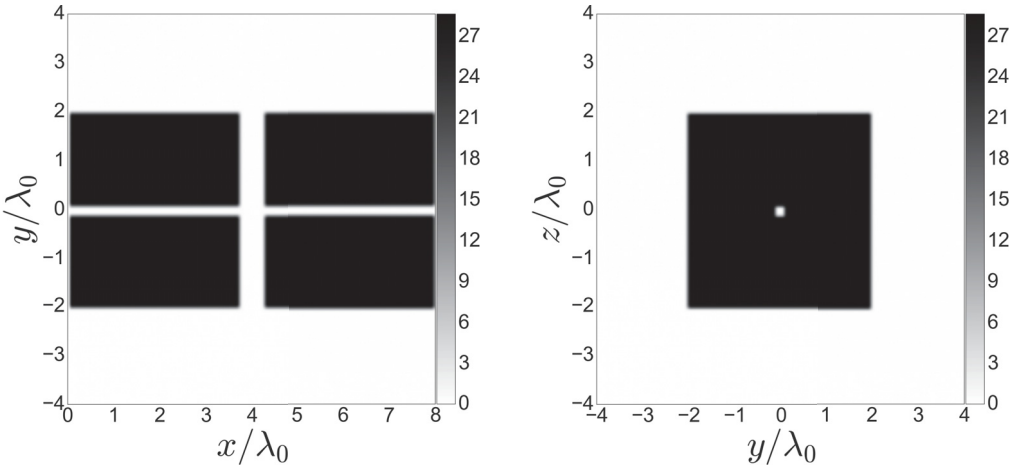

(a) Longitudinal plane (b) Transverse plane

Figure 5.1: The initial configuration of one structure period in the longitudinal (a) and transverse (b) planes for the electron acceleration simulations. The electron beam will be injected along the x-axis and traverse through twelve structure periods.

Fig. 5.1 shows the initial atom density of one structure period in the longitudinal and transverse planes. Silicon is selected to be the element of the structure. The choice of the material will be discussed further in section 5.4. In the beginning of the simulation, the silicon atom is at ground state and hence there is no free electron. Each structure period has length $l = 7.5\lambda_0$, thickness $w = 4\lambda_0$, and hole diameter $d_0 = 0.2\lambda_0$. The electrons will be

injected from the left border along the $x-$axis. Initially, the electron beam has the Lorentz factor $\gamma_i = 1000$. The beam is $8\lambda_0$ long and has the total bunch charge $Q_i \approx 318.37$ fC*. The particle beam will traverse through twelve structure periods.

As described in the previous chapter, each gap is supported by four lasers, two of which propagate along the y-axis and the others along the z-axis. The laser temporal delay between two consecutive gaps is set at $8\lambda_0/c$. The laser pulses have Gaussian profiles in the propagation directions and transverse planes. They are focused at the centre of their corresponding gaps. To save the computation time, the beam diameter at the focal point is chosen to be $2\lambda_0$ and the pulse duration is 30 fs. The normalised laser amplitude $a_0 = eE_L/m_e\omega_0 c = 1.0$, corresponding to the optical intensity $I_0 \approx 2.13 \times 10^{18}$ W/cm^2. Here, E_L is the laser electric field amplitude and ω_0 is the laser frequency.

The simulation is done in the moving frame with the box shift speed is set at the speed of light c.

5.2 Overview simulations

5.2.1 Effect of ionisation and material response

Fig. 5.2 shows the electron density of the structure in the longitudinal and transverse planes before (T_0) and after ($T_1 = T_0 + 8\lambda_0/c$) the particle beam

*In contrast, test particles will not generate field. On that account, simulations with test particles are generally faster but lack full physical description.

passes through the gap.

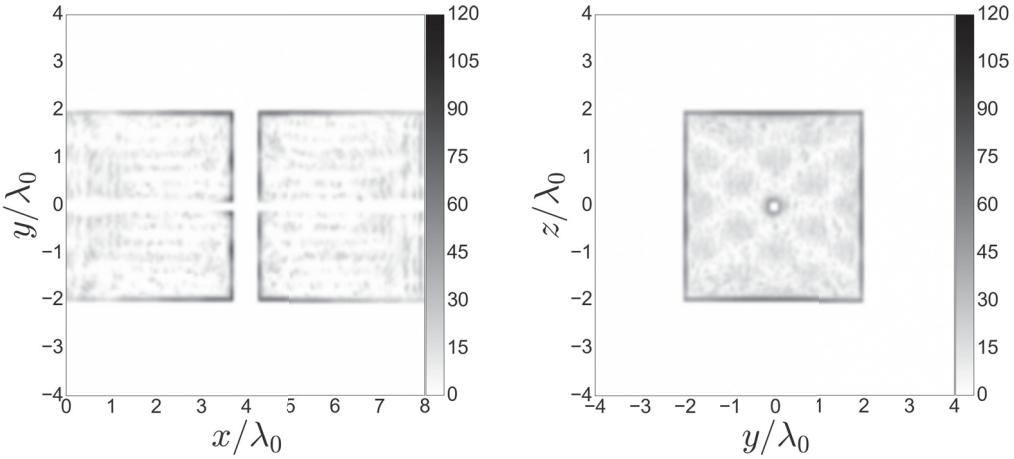

(a) Longitudinal plane, before. (b) Transverse plane, before.

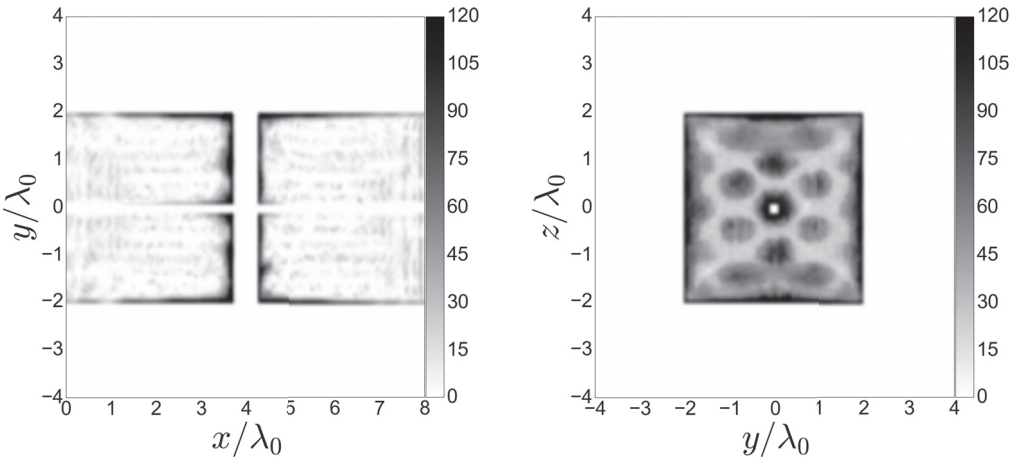

(c) Longitudinal plane, after. (d) Transverse plane, after.

Figure 5.2: The electron density of the structure in the longitudinal and transverse planes before (a and b) and after (c and d) the electron beam passes through the gap.

We observe that at both time stamps the edge of structure is going through a strong ionisation process due to the interaction with the laser fields. Indeed, the average ionisation of silicon ions at frame T_0 is 1.8, while at frame T_1 this number has increased to 5.6. Meanwhile, the bulk of the structure endures a mild perturbation with the average ionisation level is about 1.4. This

is due to the fact that the laser fields are not yet strong enough to penetrate deep into the shielding block and a part of them is reflected back at the surface.

We also notice that there is an asymmetry in the electron density between two sides of the gap in the structure (see Figs. 5.2a and 5.2c). The figures indicate that the ionisation process on the left side is stronger than its counterpart on the right side of the gap. The reason is that since the particle beam is injected from the left side of the simulation box, the field generated by the beam will interact with the left part sooner and hence the ionisation on this side will occur earlier. This leads to the lack of symmetry observed in Fig. 5.2.

5.2.2 Hole diameters

We now test the dependence of the field on the diameter d while keeping other parameters intact. In this series of simulation, the normalised laser intensities are set at $a = 1.0$, corresponding to the optical intensity $I = 2.1 \times 10^{18}$ W/cm^2. Fig. 5.3 shows the simulation results for various hole diameters $d = \{0.1\lambda_0, 0.2\lambda_0, 0.3\lambda_0, 0.4\lambda_0, 0.5\lambda_0\}$ and Fig. 5.4 shows the 1D cut of the electric field E_x.

From the figures, we observe that the hole diameter influences not only the shape but also the field amplitude at the gap centre, which in turn affects the quality of the shielding. As clearly seen from Fig. 5.3, the wider the diameter becomes, the more the field broadens into the hole. For $d \leq 0.2\lambda_0$, the field spreading can still be considered acceptable. However, with $d = 0.5\lambda_0$ the higher oscillation perpetuates across the longitudinal axis. Thus, the intention

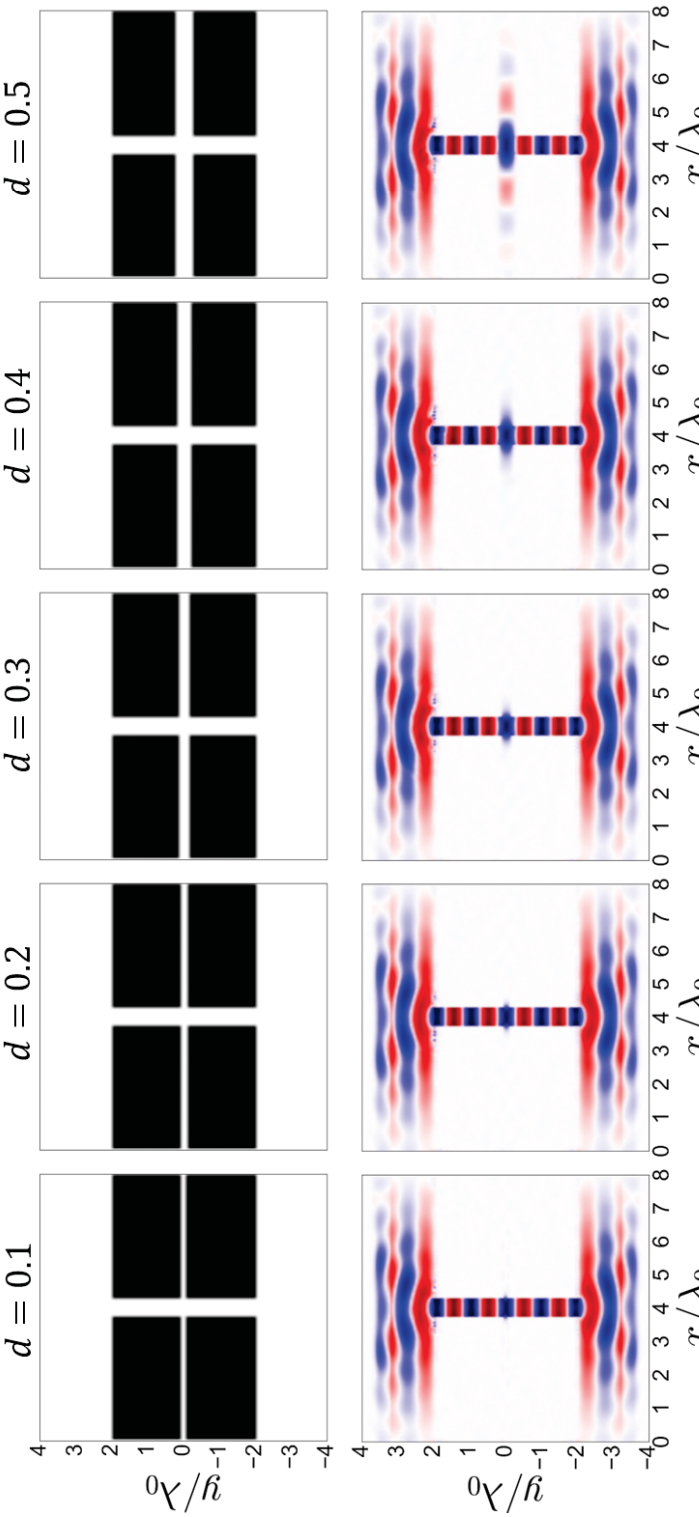

Figure 5.3: Simulation results of the structure with hole diameters $d = \{0.1\lambda_0, 0.2\lambda_0, 0.3\lambda_0, 0.4\lambda_0, 0.5\lambda_0\}$. The first row shows the ion density and second row shows the electric field component E_x.

of the shielding becomes less useful. We also notice from Fig. 5.4 that the field at the centre of the gap evolves from a flat-top to a bell-like shape and the field amplitude is being reduced as the diameter increases.

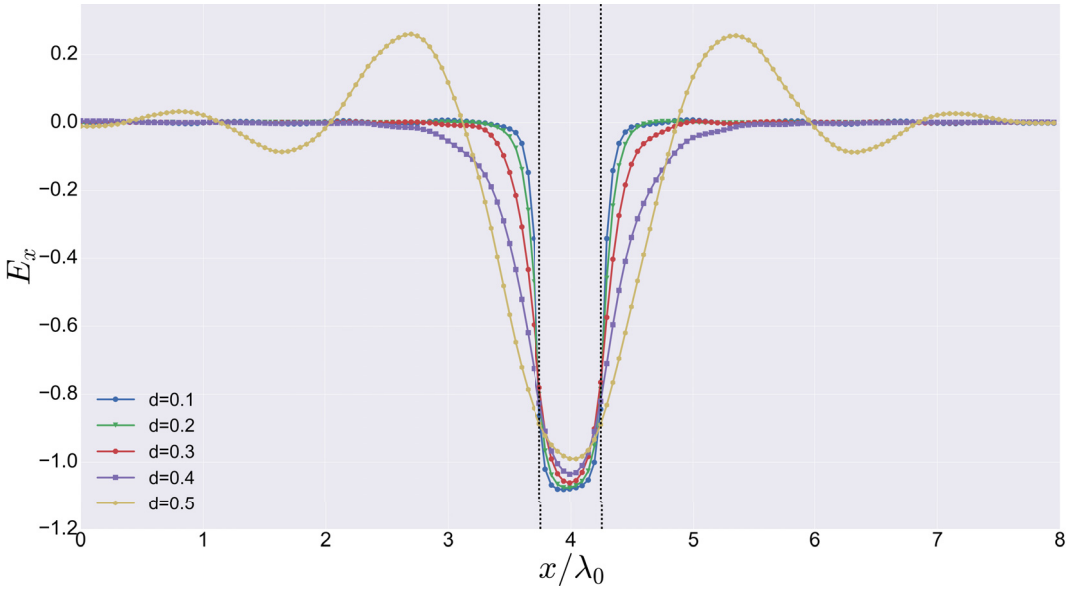

Figure 5.4: 1D cut of the electric field E_x along the longitudinal axis of the hole with diameters $d = \{0.1\lambda_0, 0.2\lambda_0, 0.3\lambda_0, 0.4\lambda_0, 0.5\lambda_0\}$. The black dotted lines indicate the extent of the gap.

We conclude that in order to achieve good quality of shielding, the hole diameter d must be kept as small as possible since wider holes will allow the fields spreading into the shielding, and even higher oscillation in certain cases. On the other hand, by maintaining $d \leq 0.2\lambda_0$ the structure offers not only the best shielding but also high intensity and flat-top field for particle acceleration.

5.3 Simulation results

5.3.1 Simulation with laser intensity a = 1.0

First we consider the simulation in which the normalised laser intensities are set to $a = 1.0$ (optical intensity $I = 2.1 \times 10^{18}$ W/cm^2). Fig. 5.5 shows the initial and final phase space x/p_x distributions of the electron beam in the acceleration simulation with twelve structure periods. Here, only particles which are trapped inside the hole are taken into consideration

$$y^2 + z^2 \leq \frac{d_0^2}{4}, \tag{5.1}$$

with y and z are particle's position and d_0 is the hole diameter.

Initially, every electron has the same Lorentz factor $\gamma_i = 1000$. Thus, the phase space distribution is a straight line, as shown in Fig. 5.5a. After travelling through the acceleration structure, the beam's phase space distribution transforms into a much different curve, as shown in Fig. 5.5b. We have several remarks concerning this evolution.

1. At the end of the simulation, the phase space distribution is sinusoidal, mimicking the laser field oscillation and its peak occurs at the time the lasers are focused at the gap centre.

2. The beam is broken into many parts and the particles are concentrating around the extremum points of the wave: if particles get accelerated, they will gather around maximum points, called acceleration windows.

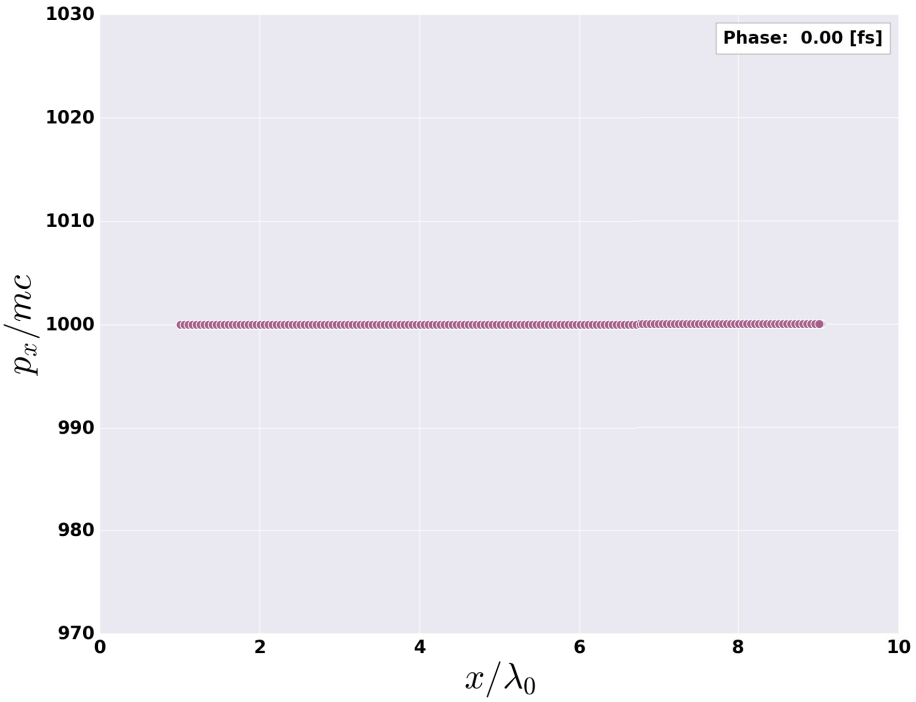

(a) The initial phase space distribution.

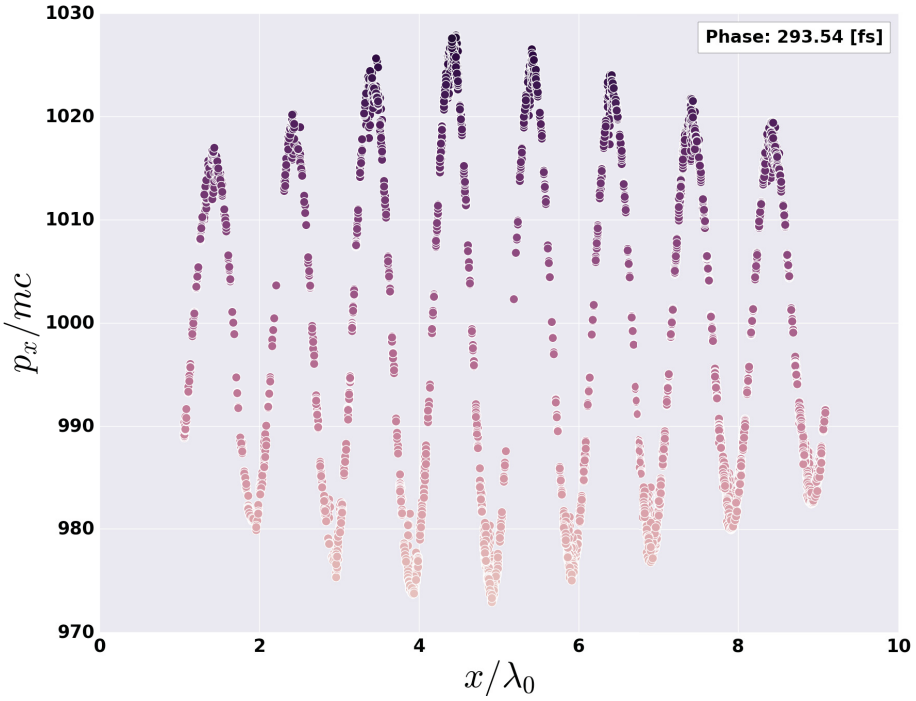

(b) The final phase space distribution.

Figure 5.5: The initial (a) and final (b) phase space x/p_x distributions of the electron beam in the acceleration simulation with twelve structure periods.

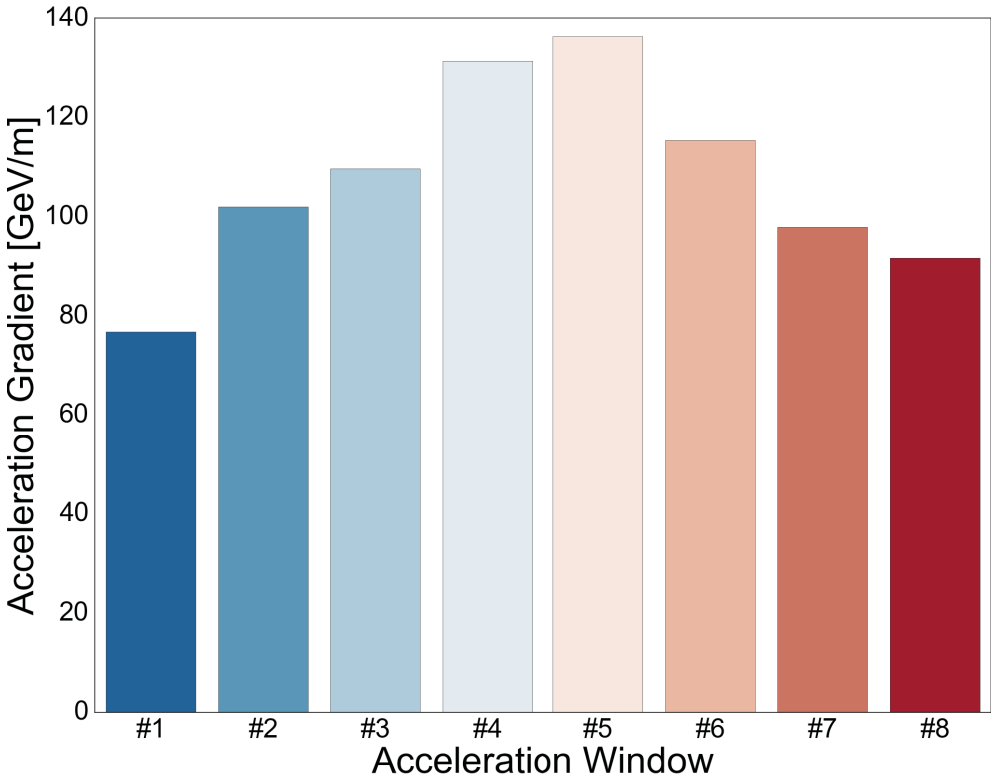

Figure 5.6: The acceleration gradient for each acceleration window in the simulation with $a = 1.0$.

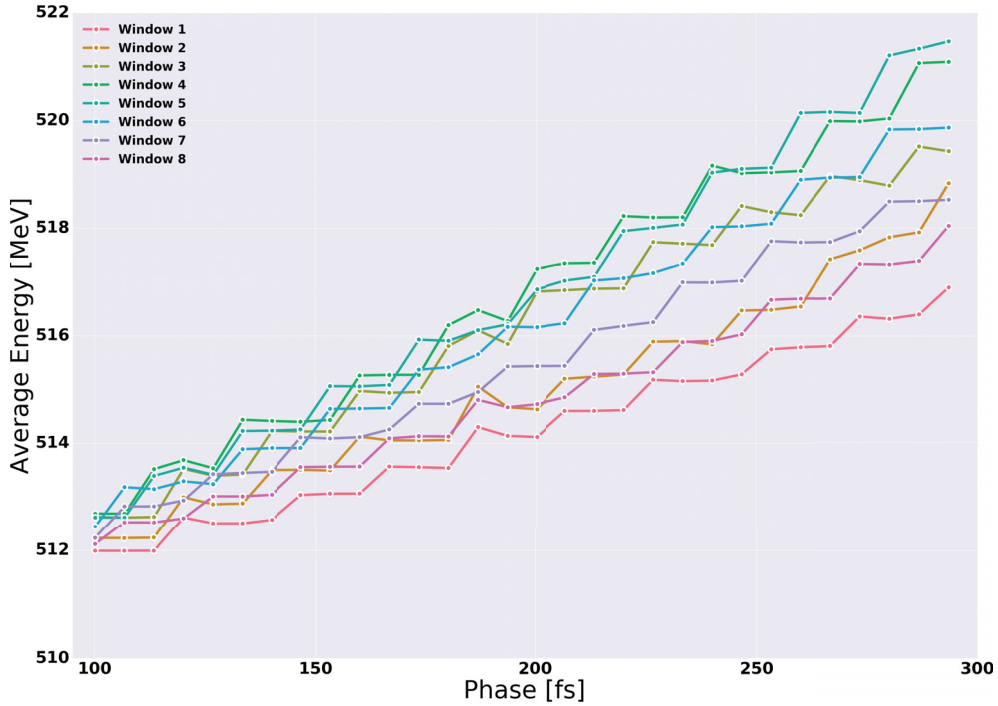

Figure 5.7: The average energy for each acceleration window in the simulation with $a = 1.0$.

Otherwise, they get together at minimum points. In this thesis, the acceleration windows are enumerated from left to right, starting from 1. In this simulation, there are in total eight windows since the beam length is 8λ.

3. The peaks of all acceleration windows are not equal. Instead, they follow the peaks of the laser field: raising and then declining. As a consequence, each acceleration window experiences a different acceleration gradient. Fig. 5.6 shows the acceleration gradient and Fig. 5.7 shows the average energy for each acceleration window. We observe that window #8 enters the gap first and achieves the final energy of 518.04 MeV with the acceleration gradient 91.69 GeV/m. The highest gradient, 136.34 GeV/m, is reached at window #5 whose average energy is 521.47 MeV after 294 fs. Then it gradually decreases to 76.9 GeV/m at the tail window #1. Moreover, Fig. 5.7 shows that the average energies of all acceleration windows increase in a short period and then remain constant by a long duration, as expected in Fig. 4.4.

4. We also see that there are less particles at the slopes between two consecutive extrema. This implies that particles will get lost if they are not localised around an extremum.

The transverse particle distribution of the electron beam at the end of the simulation is shown in Fig. 5.8. We observe that the electrons are concentrating around the centre of the y-axis and being slightly shifted to the right. Meanwhile, along the z-axis the particles are spreading out but still exhibits bell-like distribution. After travelling through the structure, the total bunch

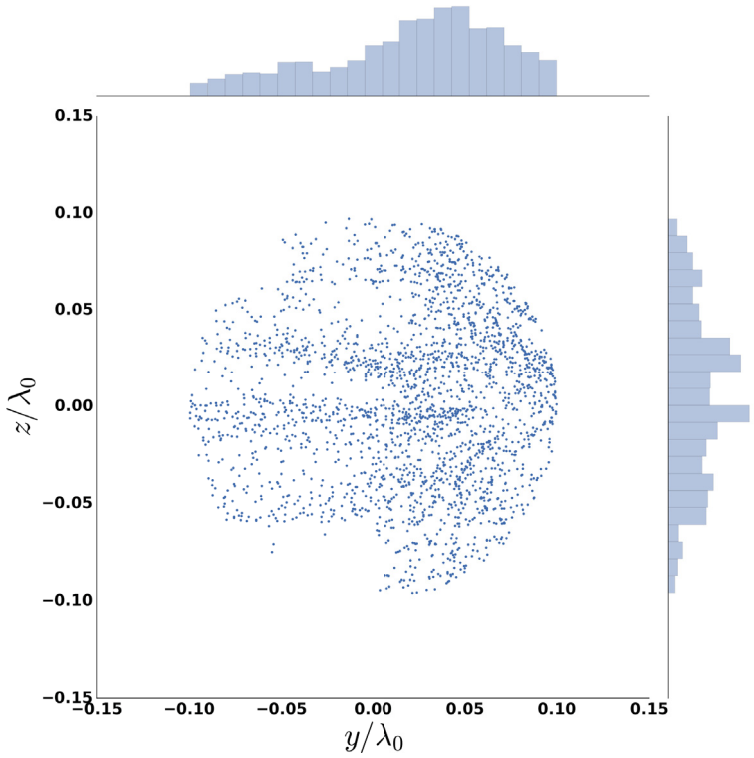

Figure 5.8: The transverse particle distribution of the electron beam at the end of the simulation.

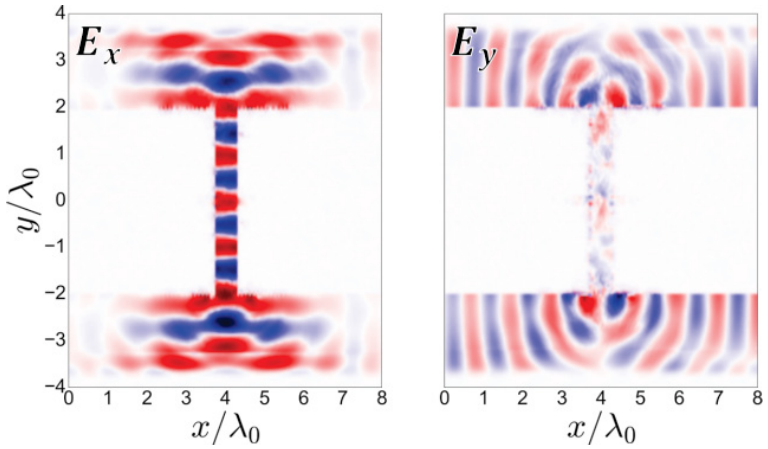

Figure 5.9: The electric field components E_x and E_y when the lasers are focused at the centre of the gap.

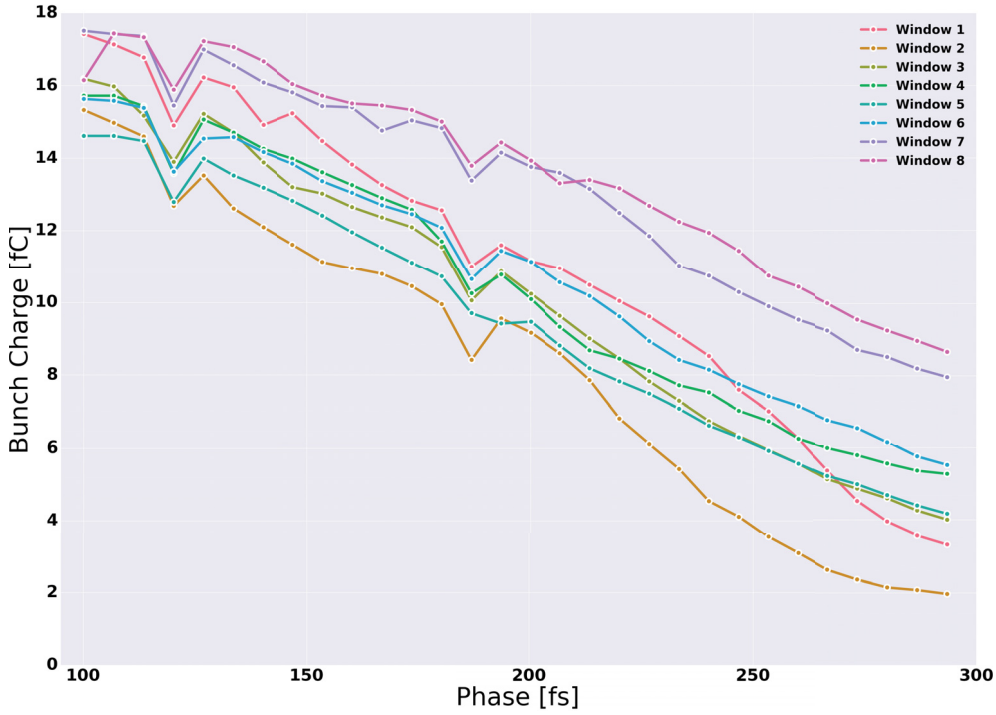

Figure 5.10: The bunch charge for each acceleration window in the simulation with $a = 1.0$.

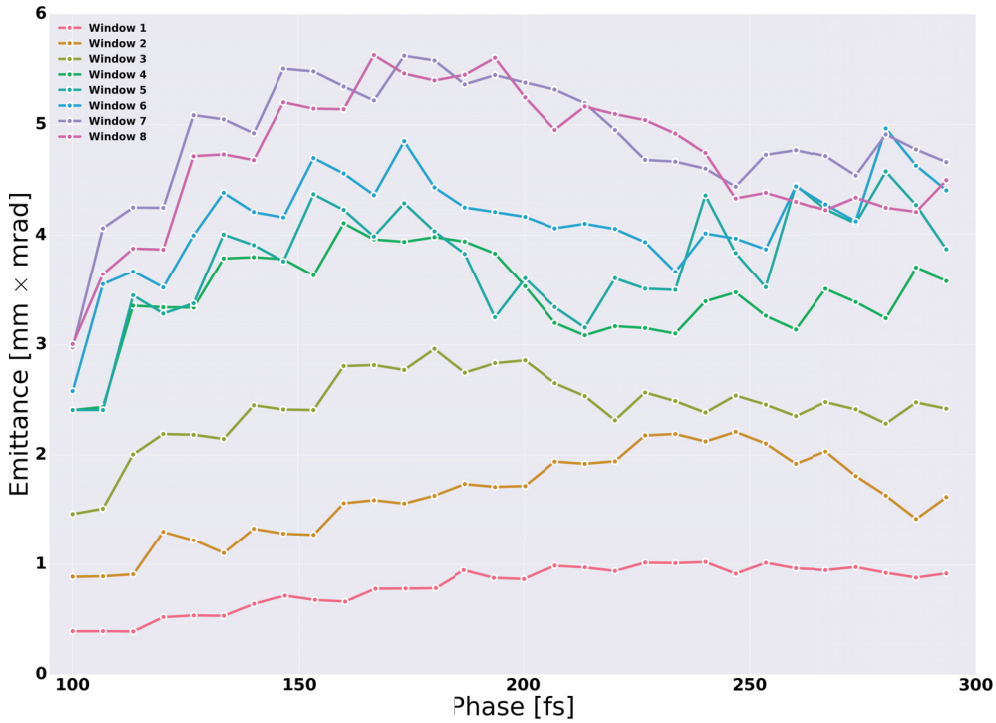

Figure 5.11: The emittance for each acceleration window in the simulation with $a = 1.0$.

charge of the beam has reduced to $Q_f \approx 64.98$ fC from the original value $Q_i \approx 318.37$ fC. This means that only 20% of injected particles are trapped. Figs. 5.10 and 5.11 show the bunch charge and emittance for each acceleration window, respectively. The bunch charge for each window gradually decreases while the emittance tends to fluctuate over the course of the simulation. This behaviour can be explained by examining the fields at the gap during the particle propagation. Fig. 5.9 shows the components E_x (accelerating field) and E_y (defocusing field) when the lasers are focused at the centre of the gap. Both fields show a sign of disturbance growing strongly: the amplitude of E_y has arisen comparable to that of E_x and thus can pull away particles travelling through. The root of this perturbation stems from the ionisation of the structure. Under the influence of an intense laser field, more electrons are removed forcefully from their atoms/ions and become free electrons. These electrons start moving and emit field to the surroundings. This field accumulates over time and in turn affects the particle beam.

From this simulation, we learn that the scheme is able to achieve high acceleration gradient in a short length. However, there appears a hindrance to the performance of the scheme: the disturbance due to the ionisation process. To see clearer the performance dependency on the laser intensity, we run another set of simulations, which will be presented in the next section.

5.3.2 Simulations with intense laser fields

Next, we study the dependence of the acceleration structure's performance and stability on the laser intensity. In this series of simulations, we consider three

cases $a = \{0.5, 1.5, 2.0\}$ in addition to $a = 1.0$ already discussed above.

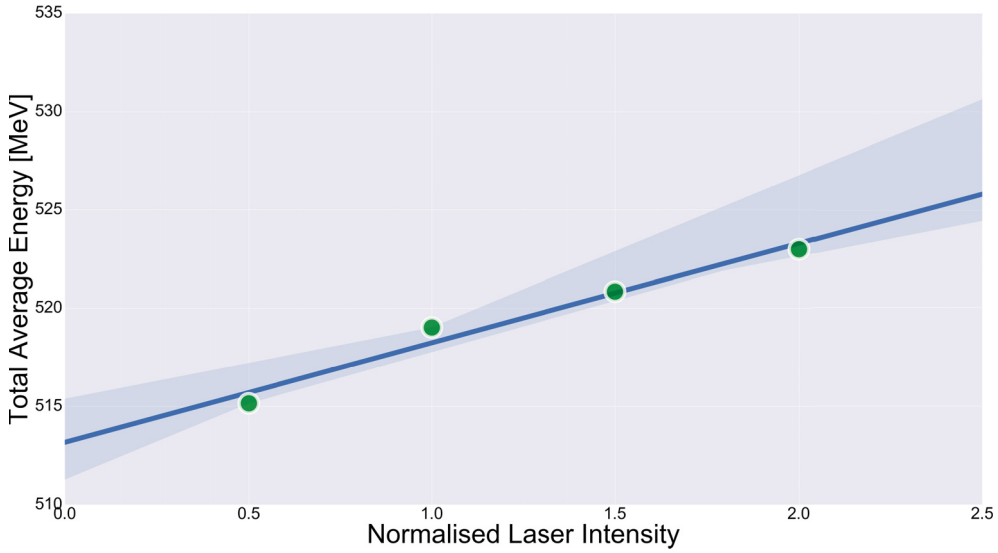

Figure 5.12: The relationship between the electron beam's average energy and laser intensity. The green dots show the average energies obtained directly from the simulations presented above; the blue line represents the regression model fit to the data; the light blue area shows the confidence interval.

Fig. 5.12 depicts the dependency of the beam's average energy on the laser intensity. In the graph, the green dots represents the values obtained directly from the simulations; the blue line shows the regression model fit to the data and the light blue area around the line shows the confidence interval. It can be clearly observed that the average energy is linearly proportional to the laser intensity.

Fig. 5.13 shows the phase space distributions of the electron beam obtained with different laser intensities. The distribution shape for $a = 0.5$ (Fig. 5.13a) is comparable to that for $a = 1.0$ presented above. Meanwhile, the distributions for $a = 1.5$ and $a = 2.0$ are strongly distorted at the region surrounding the beam centre. This region enters the gap at the same time the lasers are focused. It will accordingly experience the strongest force and sup-

posedly harvest the highest accelerating field. However, the ionisation process is more likely to occur with higher intensities. As a consequence, the field is disturbed and undesirable components have chance to rise. To illustrate this statement clearer, we compare Fig. 5.9 and Fig. 5.15. Starting with $a = 0.5$, the electric field E_x displays a clear pattern of laser oscillation. Except along the edge, the component E_y is extremely small inside the gap. As discussed above, the field disturbance can be clearly seen in the case $a = 1.0$. The situation becomes worse when the laser intensity is increased to $a = 1.5$ and $a = 2.0$. The field component E_x ceases to be flat-top and E_y becomes completely chaotic. These undesirable fields even propagate into the shielding hole. Thus, towards the tail the particles are strongly deflected from the hole or get decelerated, as observed in Figs. 5.13b and 5.13c.

With $a = 0.5$, the beam's total charge at the end of the simulation is 104.01 fC (corresponding to 31% trapped particles), while with $a = 1.5$ and $a = 2.0$ the number is 43.53 fC and 31.85 fC, respectively. From these results, we can infer that strong intensity lasers are not always favourable. Essentially it comes down to a trade-off between the beam stability and its acceleration gradient. For this part, the choice of material for the structure can play a vital role.

5.4 Summary

In this chapter, we present the simulation results of the particle acceleration in periodic structures. It is indicated from these simulations that the electrons can harvest high acceleration gradient, up to 136.64 GeV/m, in a short length

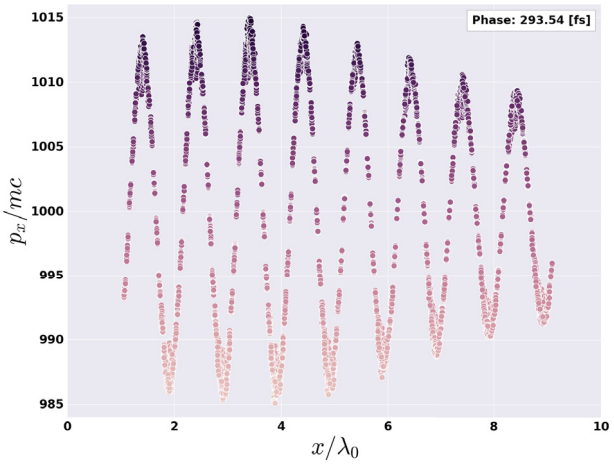

(a) $a = 0.5$.

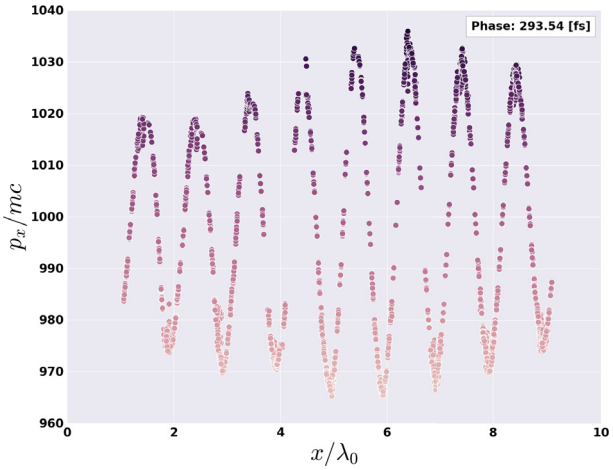

(b) $a = 1.5$.

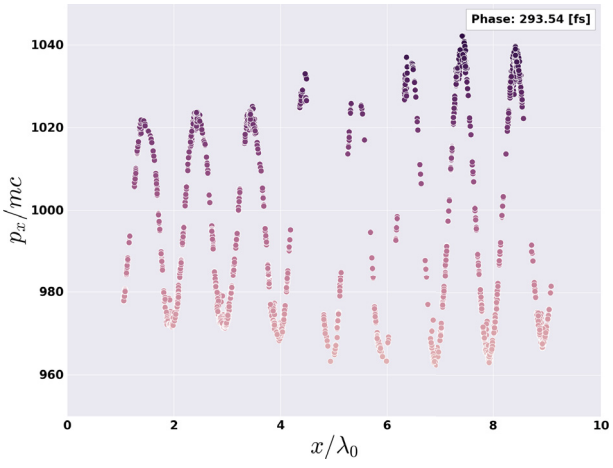

(c) $a = 2.0$.

Figure 5.13: The phase space x/p_x distributions of the electron beam with various laser intensities.

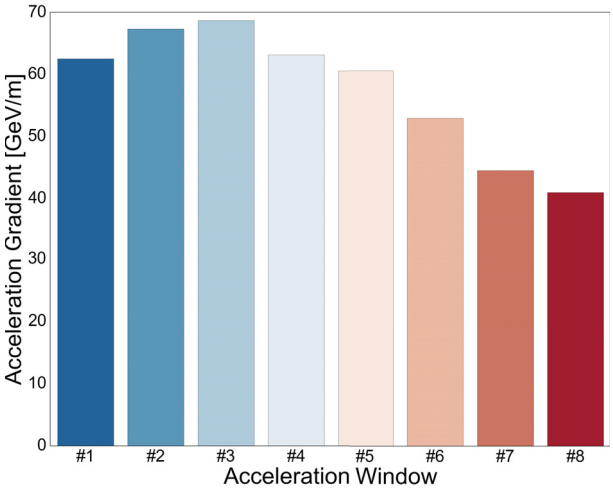

(a) $a = 0.5$.

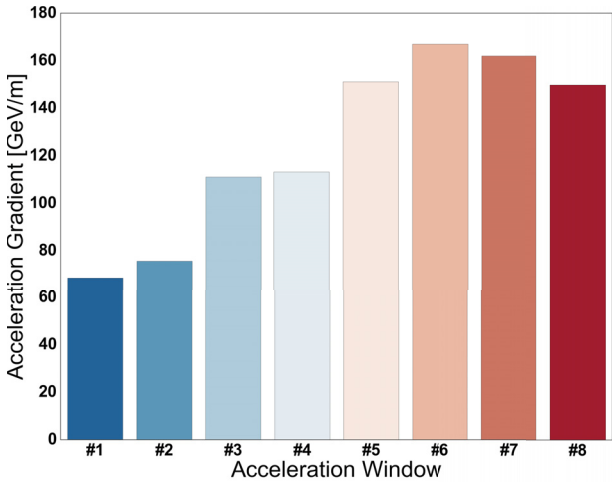

(b) $a = 1.5$.

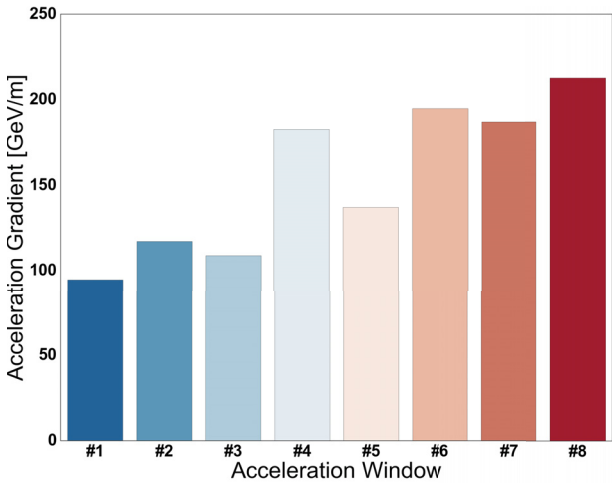

(c) $a = 2.0$.

Figure 5.14: The acceleration gradients of the electron beam with various laser intensities.

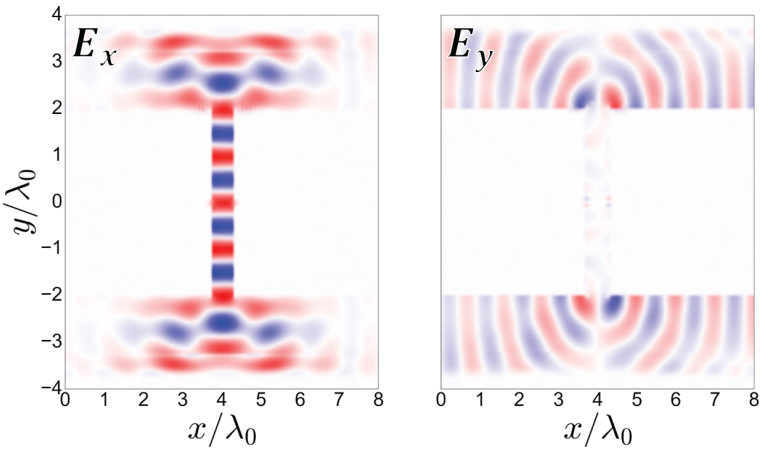

(a) $a = 0.5$.

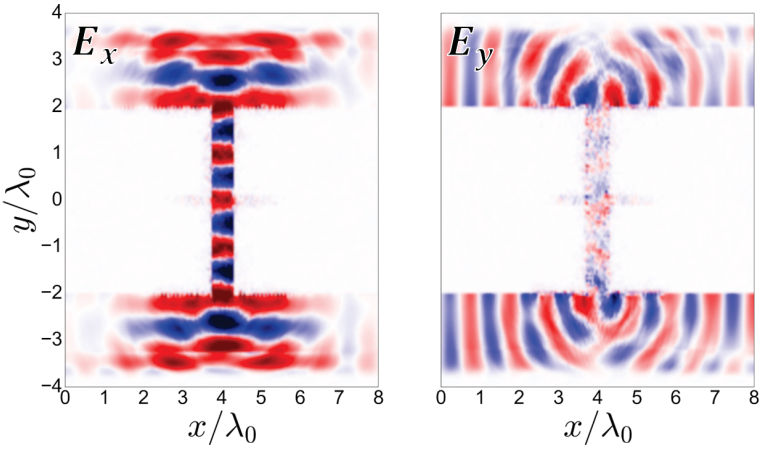

(b) $a = 1.5$.

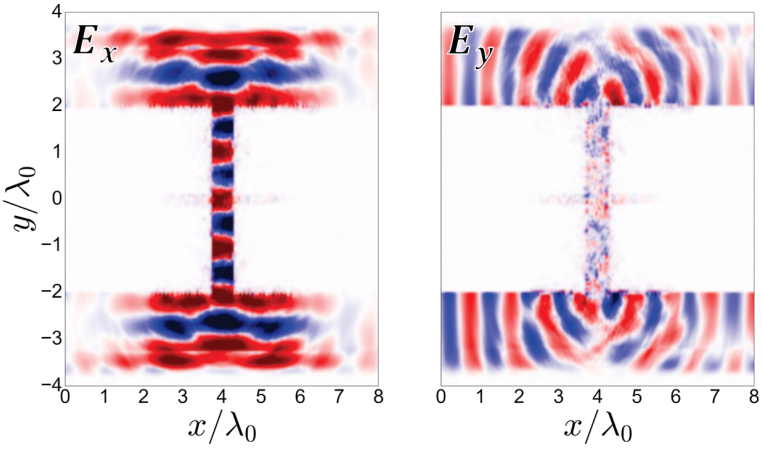

(c) $a = 2.0$.

Figure 5.15: The electric field components E_x and E_y when the lasers are focused at the centre of the gap with different laser intensities.

of 76.8×10^{-4} cm with the laser intensity $a_0 = 1.0$. However, the result is by no means perfect. Due to the ionisation of the structure, the field perturbation has space to grow such that many particles get lost during the propagation in the structure. At the end of the simulation, only 20% of particles pass through. By lowering the laser intensity to $a_0 = 0.5$, the number of trapped particles is increased to 30% but the highest acceleration gradient is reduced by half. Thus, in order to improve the stability of the scheme, we have to take care of the disturbance caused by the ionisation process.

Choice of material For every material, the laser damage threshold fluence is the breakdown limit of that material. Fig. 5.16 shows the damage threshold fluence of several optical materials [52].

From the laser damage threshold fluence F_{th} (unit: J/m^2), we can estimate the maximum accelerating electric field E_{max} (unit: GV/m) that a material can sustain without breaking down by the following formula

$$E_{max} \approx \sqrt{F_{th}}. \tag{5.2}$$

Even though the material breakdown will eventually occur, materials with higher threshold fluences can sustain for a longer time. As a consequence, the field in the gap can be be come more stable, which is critical for accelerating and focusing performance of particles. In the scope of this thesis, the material of the structure is silicon, which has $E_{max} \approx 1$ GV/m. I expect that when materials like Al_2O_3 or SiO_2 are used, the performance of the structure can be greatly improved.

Comparison with the previous development In [48], we reported that

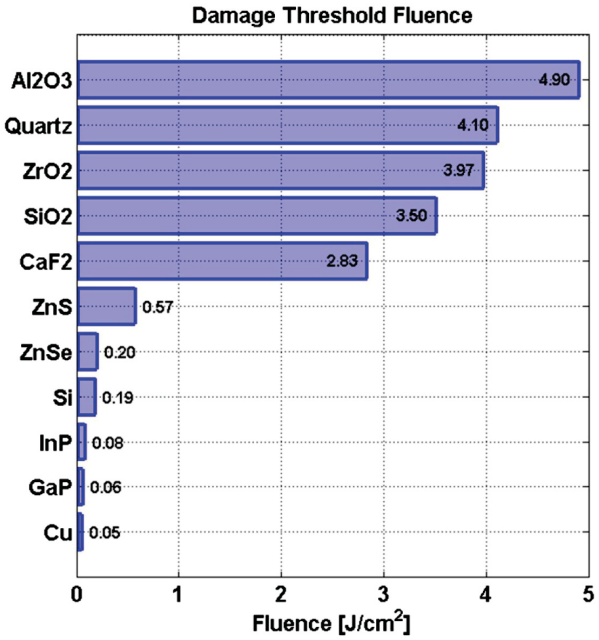

Figure 5.16: The laser damage threshold fluence of several optical materials. The measurements were conducted with a 1[ps], 800[nm], 600[Hz] Ti:sapphire laser. The picture is taken from K. Soon et al. [52].

gradient above TeV/m was achieved and the electron bunch gained up to 200 GeV/m over a distance 10.2 cm in the open accelerating structure an acceleration (see Fig. 5.17). The acceleration gradient about 2 TeV/m is

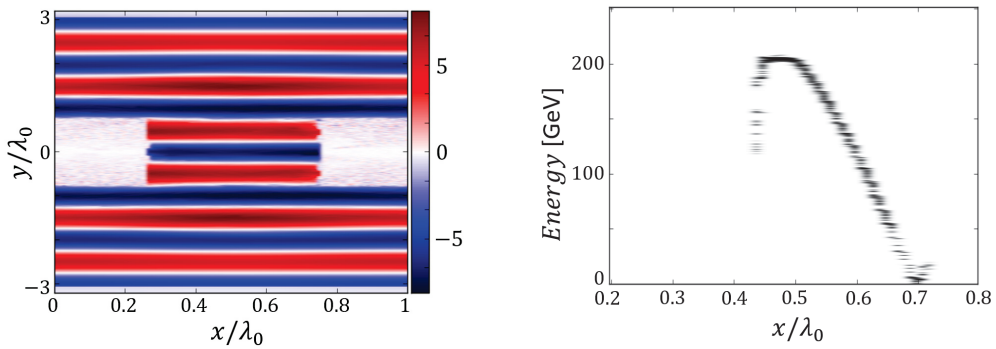

(a) The accelerating field component E_x. (b) The longitudinal electron phase space.

Figure 5.17: (a) The accelerating field component E_x and (b) the longitudinal electron phase space after the accelerating distance 10.2 cm (b). The electrons gained up to 200 GeV over a distance 10.2 [cm].

at least 20 times higher than the one presented in the previous section. The reasons leading to this dissimilarity are as follows:

- In the past publication, we assumed that the structure was fully ionised. This assumption is critical. Under this supposition, the structure can sustain higher laser intensities in a longer duration. In Fig. 5.17a, the peak amplitude reaches 8 TV/m.
- The electron bunch was test particles. The usage of test particles can greatly reduce the simulation duration. However, it has one drawback: the bunch-charge effect is completely ignored. Thus, the physical picture might not accurately rendered.

However, the full ionisation condition is not easily satisfied in experiment. We have to inject a strong laser pulse to completely ionise the structure and wait until the system attains the equilibrium. Only until then can the accelerating phase begin. But we also need to take into account that the effect of the residual field from the ionising phase might to the main phase. If all points are considered, the scale and complexity of simulations would become enormous and present significant difficulties. Thus, we adapt to a simpler and more realistic scenario which is presented in this chapter.

CHAPTER 6

Particle Merging Algorithm in PIC code

In the previous chapters, we explored the possibility of the particle acceleration in periodic structures. It is suggested that using heavier materials can help to mitigate the undesirable fields caused due to ionisation. In these cases, this means that there would be more electrons created in the simulation box which in turn can increase the computation time. The issue can be handled by merging particles together such that the physical description of the system is kept intact after a merging event. In this chapter, we present an efficient algorithm for merging particles in PIC codes: Voronoi particle merging algorithm.

Authorship claim: The content of this chapter is largely reproduced from my paper [53] published in Computer Physics Communication on February 2016. Several parts are edited to fit into the structure of this thesis. Particularly, the new section 6.4 is added to discuss in more detail the matter of energy conservation in this topic.

6.1 Survey on the topic

For more than 60 years the particle-in-cell (PIC) technique [54] has been used to simulate a wide variety of physical problems, ranging from electrical discharge to particle acceleration. However, in several scenarios - in particular field ionisation or QED cascades - the number of particles in the simulation box grows exponentially. Due to an overwhelming number of particles, the associated memory required can easily exceed that available on even high performance computers and as a consequence the computational performance drops drastically.

In these situations, a particle merging algorithm (PMA) has to be implemented. The main goal of a PMA is to reduce the number of particles in a simulation box while keeping the physical properties of the system intact after a merging event. A straightforward PMA is to randomly pick a pair of particles and then merge, see for example [55]. Since it merges with no guidance, the method is not able to preserve the phase space distribution, and so the physical picture is likely to be distorted after merging. The problem is that it fails to incorporate the notion of proximity in the phase space, i.e. how similar particles are, into its framework. In the scope of this paper, we call this PMA the blind method.

Lapenta already proposed a scheme for merging particles (called "particle coalescence") in [56] and [57]. In this method, particles are first sorted into two bins. Then the binning process continues until the number of particles per bin is small enough for the pairwise comparison. This type of PMA was then refined and improved by Teunissen and Ebert [58], in which the k-d tree

method was employed to search for the nearest neighbour. Recently, a similar approach was also proposed by Vranic et al. [59], where the momentum space is divided into smaller subcells for sorting particles.

We design our PMA from a different point of view, in which the algorithm not only merges particles which are close in the phase space but also offers users a direct control over errors introduced by a merging event. The notion of proximity in our algorithm is developed through the concept of the Voronoi diagram [60], thus the name Voronoi PMA. As shown later, the quantification of the error is realised through the coefficients of variation. The algorithm is successfully implemented into the framework of the VLPL (Virtual Laser Plasma Laboratory) code [38].

The chapter is organised as follows: in section 6.2, we briefly introduce the definition and some examples of the Voronoi diagram; the comprehensive description of our PMA is revealed in section 6.3; in section 6.5 the performance of our merging algorithm are discussed in three case studies:

The counter-propagating plasma blocks : Section 6.5.1. This simple test was utilised during the design phase of the algorithm.

The two-stream instability : Section 6.5.2. This is the classical case, in which the phase space distribution undergoes a dynamic and vigorous evolution.

The magnetic shower : Section 6.5.3. This case study is carried out to test the quality of the PMA in a situation where the number of particles always increases.

Finally, the chapter is summarised in section 6.6.

6.2 Voronoi diagram

For any given set of n sites, $S = \{s_1, s_2, ..., s_n\}$ in the real d-space $\mathbb{R}^d$, the Voronoi cell $\mathcal{V}_k$ associated with the site s_k is a set of points in $\mathbb{R}^d$, such that the distance from those points to s_k is not greater than the distance to any other site s_j $(j \neq k)$ in S [61].

$$\mathcal{V}_k = \{x \in \mathbb{R}^d \mid \forall j : \text{dist}(x, s_k) \leq \text{dist}(x, s_j)\} \text{ for } 1 \leq i, j \leq n. \tag{6.1}$$

Here, $\text{dist}(x, y)$ denotes the metric function of the distance in $\mathbb{R}^d$. The Voronoi diagram was first developed, though informally, in 1644 by Descartes. In 1908, the Russian-Ukrainian mathematician G. F. Voronoi formally defined and studied the general case [60]. The concept is used in many contemporary research fields, such as geophysics, meteorology, and condensed matter physics.

Observing eq. (6.1), we see that the metric function $\text{dist}(x, y)$ plays a vital role in the formation of the Voronoi diagram. Different metrics will result in different Voronoi diagrams. Moreover, in our case, different metrics also require different implementations of the algorithm (see section 6.3 for more detail). Fig. 6.1 shows the Voronoi diagram of a random distribution with Euclidean and Chebyshev measures. Given two vectors $\mathbf{p}$ and $\mathbf{q}$, the

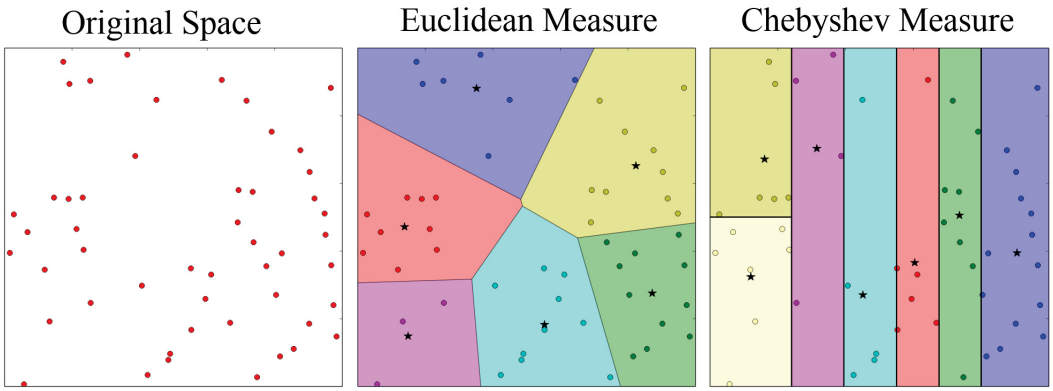

Figure 6.1: The Voronoi diagrams with different metric functions. Each Voronoi region is painted with a distinct colour. The black star in each region is the Voronoi centroid.

Euclidean distance is

$$\mathrm{dist}(\mathbf{p},\mathbf{q}) = \sqrt{\sum_i (q_i - p_i)^2}, \tag{6.2}$$

while the Chebyshev distance is given by

$$\mathrm{dist}(\mathbf{p},\mathbf{q}) = \max |q_i - p_i|. \tag{6.3}$$

6.3 Algorithm

Input: The algorithm requires two user inputs, $T_{\mathbf{X}}$ and $T_{\mathbf{P}}$, which are the tolerances for position and momentum. These parameters are employed as the stopping condition and appear at step 3. A merging event will take place in a simulation cell if the particle number N of that cell is greater than the minimum particle number $N_{\min}$. The merging events are not supposed to take place at every time step. Instead, it is obligated to make sure that the merging

rate is greater than the periods of other physical events in the simulation box. By doing so, the chain of events is kept intact during the merging interval.

Step 1: For every simulation cell, collect all particles (weight w_i, position $\mathbf{x}_i$, and momentum $\mathbf{p}_i$) in that cell into a set $\mathcal{V}_0$. This set $\mathcal{V}_0$ is the first Voronoi cell, which covers the entire phase space of a simulation cell. We then calculate the statistical average in the phase space of this set of particles $\mathcal{V}_0$ by the following formulae:

$$W_0 = \sum_{i \in \mathcal{V}_0} w_i, \tag{6.4}$$

$$\mathbf{X}_0 = \frac{\sum_{i \in \mathcal{V}_0} w_i \mathbf{x}_i}{\sum_{i \in \mathcal{V}_0} w_i}, \tag{6.5}$$

$$\mathbf{P}_0 = \frac{\sum_{i \in \mathcal{V}_0} w_i \mathbf{p}_i}{\sum_{i \in \mathcal{V}_0} w_i}. \tag{6.6}$$

The point $(\mathbf{X}_0, \mathbf{P}_0)$ with weight W_0 is the centroid of the first Voronoi cell $\mathcal{V}_0$. From now on, quantities of a Voronoi centroid are denoted by the capital letters.

Step 2: We calculate the standard deviation of each dimension l in the phase space with respect to the current Voronoi centroid:

$$\sigma_{\mathbf{X}_{0,l}} = \sqrt{\frac{1}{W_0} \sum_i w_i (\mathbf{x}_{i,l} - \mathbf{X}_{0,l})^2}, \tag{6.7}$$

$$\sigma_{\mathbf{P}_{0,l}} = \sqrt{\frac{1}{W_0} \sum_i w_i (\mathbf{p}_{i,l} - \mathbf{P}_{0,l})^2}. \tag{6.8}$$

We compute the coefficient of variation (CV) Δ for each dimension. The CVs

for spatial and momentum dimensions are defined as

$$\Delta_{\mathbf{X}_{0,l}} = \frac{\sigma_{\mathbf{X}_{0,l}}}{L_{\mathbf{X}_{0,l}}}, \tag{6.9}$$

$$\Delta_{\mathbf{P}_{0,l}} = \frac{\sigma_{\mathbf{P}_{0,l}}}{\mathbf{P}_{0,l}}. \tag{6.10}$$

For the spatial dimensions, due to the symmetry in space the CV $\Delta_{\mathbf{X_0}}$ is defined as the ratio between the standard deviation and the length $L_{\mathbf{X}0}$ of the first Voronoi cell $\mathcal{V}_0$. On the other hand, since there is no such symmetry in the momentum space, the CV $\Delta_{\mathbf{P_0}}$ is obtained from dividing the standard deviation by the mean value. As the CVs are dimensionless numbers we can treat the data obtained from the position and momentum spaces equally (see step 4 below). In our algorithm, the CVs represent the accuracy of the merging scheme, with smaller CVs resulting in smaller errors due to merging.

Step 3: We compare the recently obtained CVs $\Delta_{\mathbf{X}_0}$ and $\Delta_{\mathbf{P}_0}$ with their corresponding tolerances $T_{\mathbf{X}}$ and $T_{\mathbf{P}}$. If a Voronoi cell has all six CVs less than or equal to the tolerances, the algorithm will mark that cell finished and stop dividing it. On the other hand, as long as there is at least one component whose CV does not satisfy the aforementioned requirement, the algorithm will keep going to the next step.

Step 4: We consider the individual components of $\Delta_{\mathbf{X}_0}$ and $\Delta_{\mathbf{P}_0}$, that is $\{\Delta_x, \Delta_y, \Delta_z, \Delta_{p_x}, \Delta_{p_y}, \Delta_{p_z}\}$, and find the axis k which has the largest deviation.

$$k = \max_l \Delta_l, \text{ with } l \in \{x, y, z, p_x, p_y, p_z\}. \tag{6.11}$$

Often, the tolerances $T_{\mathbf{X}}$ and $T_{\mathbf{P0}}$ are unequal, due to their instinctive attributes: it is reasonable to relax a bit on $T_{\mathbf{X}}$ and put more restraint on $T_{\mathbf{P}}$. This might prompt an issue, in which two components of CVs, one from space and the other from momentum, are equal and satisfy eq. . One option is to select randomly one of the CVs and proceed. Despite the fact that two CVs are equal, the separation of one CV from its corresponding tolerance is likely far greater than the other. For this reason, this quick but rash solution would render a poor cutting in the next step.

In the VLPL framework, I employ a more rational approach. Assume that Δ_x^{max} and Δ_p^{max} are the largest deviations in the **X**- and **P**-spaces, respectively. We calculate the difference ratios

$$R_X = (\Delta_X - T_{\mathbf{X}})/T_{\mathbf{X}}, \tag{6.12}$$

$$R_P = (\Delta_P - T_{\mathbf{P}})/T_{\mathbf{P}}, \tag{6.13}$$

If $R_X \geq R_P$, the division in **X**-space is favoured, and vice versa.

Step 5: Make a hyperplane cut through the the Voronoi centroid perpendicular to the axis k. Denote q and Q the dynamic variables of the particles and of the centre, respectively, on the axis k. The hyperplane cut divides the set $\mathcal{V}_0$ into two new independent subsets $\mathcal{V}_1$ and $\mathcal{V}_2$, whose new centroids are given by

$\mathcal{V}_1 = \{i \in \mathcal{V}_0 : q_i \leq Q\}$	$\mathcal{V}_2 = \{i \in \mathcal{V}_0 : q_i > Q\}$
$W_1 = \sum_{i \in \mathcal{V}_1} w_i$	$W_2 = \sum_{i \in \mathcal{V}_2} w_i$
$\mathbf{X}_1 = \frac{\sum_{i \in \mathcal{V}_1} w_i \mathbf{x}_i}{\sum_{i \in \mathcal{V}_1} w_i}$	$\mathbf{X}_2 = \frac{\sum_{i \in \mathcal{V}_2} w_i \mathbf{x}_i}{\sum_{i \in \mathcal{V}_2} w_i}$
$\mathbf{P}_1 = \frac{\sum_{i \in \mathcal{V}_1} w_i \mathbf{p}_i}{\sum_{i \in \mathcal{V}_1} w_i}$	$\mathbf{P}_2 = \frac{\sum_{i \in \mathcal{V}_2} w_i \mathbf{p}_i}{\sum_{i \in \mathcal{V}_2} w_i}$

Step 6: Sort the particles into their corresponding new sets. Repeat steps 2-6 for the new sets $\mathcal{V}_1$ and $\mathcal{V}_2$ until the stopping condition is satisfied.

Step 7: If the stopping condition is met for all Voronoi cells, the algorithm removes all particles from the simulation cell and replaces them with the Voronoi centroids as the merged particles. The algorithm ends here.

We have several remarks on our algorithm:

- Our Voronoi PMA is inspired by Schreiber's adaptive k-means clustering algorithm used in Computational Geometry [62].
- In step 1, we state that the merging process is carried out cell by cell. However, the algorithm can be adjusted such that the first Voronoi cell $\mathcal{V}_0$ contains all particles from the simulation box and starts merging from there. The rest of the algorithm is kept intact. However, it is likely that the global merging approach violates the local charge conservation. In this case, one must take into account a correction scheme in order to compensate for the error caused by merging events. Which implementation is used depends strongly on the user preference or the code framework.

We adhere to the cell-by-cell implementation as it is readily parallelised.

- The distance measure used here (see eq. (6.3), step 4) can be considered as a Chebyshev-like distance, since Eq. (6.3) is not guaranteed for every particle and phase space dimension. We have chosen this measure instead of a more obvious candidate, the Euclidean measure, for the following reasons:

    1. The simplest implementation of the Euclidean measure requires the seeding of Voronoi centroids at the beginning of the algorithm. Moreover, the number of Voronoi centroids is kept constant throughout the algorithm. This limitation not only reduces greatly the flexibility of the algorithm but also cannot fit well to the dynamic situation of a physical problem [62]. Conversely, the Chebyshev measure requires no seeding and suits perfectly the divide-and-sort scheme, which is applied here.

    2. In [63], the author states a rule of thumb that for a given dataset of N points, the number of centroids is set to $k \approx \sqrt{N/2}$. Again, the number of Voronoi centroids cannot be changed once the algorithm starts. As such, we do not follow this rule.

    3. In order to use the Euclidean measure without a fixed number of centroids, we would have to solve the problem of an unknown number of clusters in a dataset. This can be done through the Bayesian information criterion [64] or the removing centroids method [65]. The former approach is difficult to implement, while the latter tends to be computationally intensive.

6.4 Energy conservation in PMA

In this section, we will discuss the main concern of every PMA: the energy conservation of the system after a merging event. First, we consider the relation between energy E and momentum $\mathbf{P}$ is

$$E = \sqrt{1 + \mathbf{P}^2}. \tag{6.14}$$

Similarly to step 1 above, we have the statistical average of energy of a set of particles $\mathcal{V}_0$

$$E_0 = \frac{\sum_{i\in\mathcal{V}_0} w_i E_i}{w_i}. \tag{6.15}$$

$$\begin{aligned} \Rightarrow E_0^2 &= \left(\frac{\sum_{i\in\mathcal{V}_0} w_i E_i}{w_i}\right)^2 = \frac{\sum_i w_i^2 E_i^2 + 2\sum_{i\neq j} w_i w_j E_i E_j}{\left(\sum_i w_i\right)^2} \\ &= \frac{\sum_i w_i^2 \left(1 + \mathbf{p}_i^2\right) + 2\sum_{i\neq j} w_i w_j \sqrt{(1+\mathbf{p}_i^2)(1+\mathbf{p}_j^2)}}{\left(\sum_i w_i\right)^2}. \end{aligned} \tag{6.16}$$

On the other hand, the expected value of energy of a new particle, created from the particle set $\mathcal{V}_0$ is

$$E_{exp} = \sqrt{1 + \mathbf{P}_0^2}. \tag{6.17}$$

$$\begin{aligned} \Rightarrow E_{exp}^2 &= 1 + \left(\frac{\sum_i w_i \mathbf{P}_0^2}{\sum_i w_i}\right)^2 = \frac{\left(\sum_i w_i\right)^2 + \left(\sum_i w_i \mathbf{P}_i\right)^2}{\left(\sum_i w_i\right)^2} \\ &= \frac{\sum_i w_i^2 + 2\sum_{i\neq j} w_i w_j + \sum_i w_i^2 \mathbf{p}_i^2 + 2\sum_{i\neq j} w_i w_j \mathbf{p}_i \mathbf{p}_j}{\left(w_i\right)^2} \\ &= \frac{\sum_i w_i^2 \left(1 + \mathbf{p}_i^2\right) + 2\sum_{i\neq j} w_i w_j (1 + \mathbf{p}_i \mathbf{p}_j)}{\left(\sum_i w_i\right)^2}. \end{aligned} \tag{6.18}$$

Then, the difference between Eqs. (6.16) and (6.18) is

$$\begin{aligned}\delta E^2 &= E_0^2 - E_{exp}^2 \\ &= \frac{2}{\left(\sum_i w_i\right)^2} \sum_{i \neq j} w_i w_j \left(\sqrt{(1+\mathbf{p}_i^2)(1+\mathbf{p}_j^2)} - (1+\mathbf{p}_i \mathbf{p}_j) \right). \end{aligned} \tag{6.19}$$

We observe that from Eq. (6.19) the difference δE^2 is always non-zero unless $\mathbf{p}_i = \mathbf{p}_j$. Thus, the whole system always loses an amount of energy after a merging event. For the Voronoi PMA, this issue can be observed in Figs. 6.7 and 6.11 below. These figures show the relative error in the total energy for the two-stream instability and the magnetic shower, respectively. These graphs show that the loss in energy per merging event is extremely small (on the order of 10^-7 to 10^-5). The merging quality can be further improved by introducing a specific mechanism to conserve energy perfectly and directly.

We can consider the Langdon-Marder corrector-scheme [66][67][68]. We also make a side remark that the Langdon-Marder scheme becomes obligatory in case users want to implement the algorithm through the global merging approach. On the other hand, one may think of merging into two particles as in [59]. These two approaches are similar in the sense that the rectification mechanism occurs after a merging event takes place. In [58], the authors introduce four different schemes to deal with this issue: 1. conserve momentum strictly; 2. conserve energy strictly; 3. conserve both momentum and energy on average; 4. scale velocity of one particles to conserve energy strictly. In this case, the correction process is internally implanted into the algorithm. Which approach yields the optimum solution is still an open question.

6.5 Simulation

Having presented the algorithm, we proceed to test its performance. To this end, we consider three situations: counter-propagating plasma blocks, the two-stream instability [39] [69], and the magnetic shower produced by an energetic particle entering a strong magnetic field [70].

Before going further, we briefly describe the implementation of the blind method used here for comparison. We define the parameter α as the merging fraction. A merging event will take place in a simulation cell if the number of particles N of that cell satisfies the condition $N > \text{ceil}(\alpha N)$. Then, the blind method merges particles in the current cell until the number of particles after merging is at maximum $\text{ceil}(\alpha N)$. This implementation allows the blind method produces the same number of particles as in the Voronoi PMA for fair comparison.

6.5.1 Counter-propagating Plasma Blocks

The counter-propagating plasma blocks simulation is a simple test, in which two blocks of non-interacting particles with uniform density distribution propagate and then overlap each other. These blocks have the same momentum magnitude but opposite propagation directions (see Fig. 6.2). With no merging, there is no change to the system apart from the translation in x-direction after the blocks pass through each other. By using this test we can easily spot whether a given PMA preserves the phase space distributions since there is a duration when the blocks overlap. If a merging method does not preserve, two

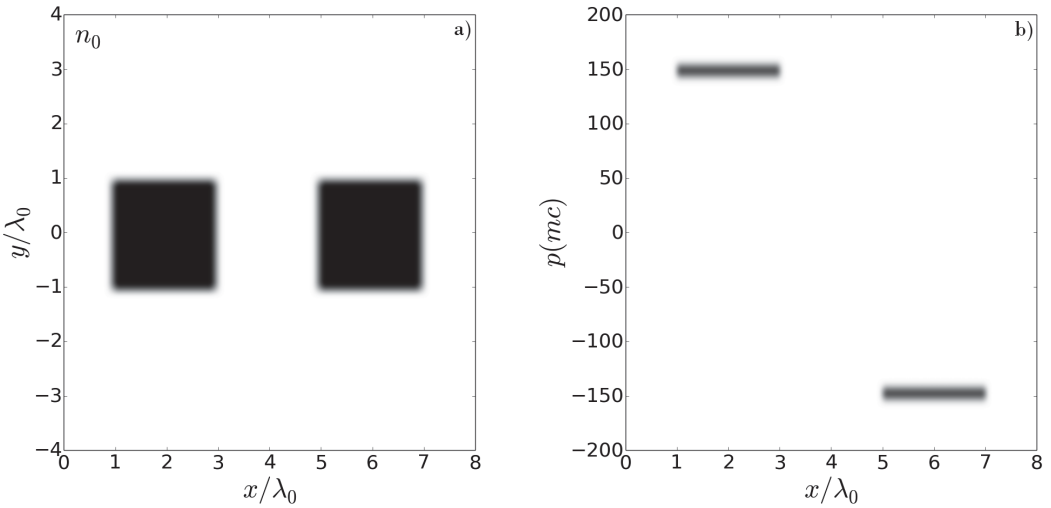

Figure 6.2: The initial configuration for the counter-propagating plasma blocks simulation: two blocks have the same momentum magnitude but opposite propagation directions. The merging event will commence when two blocks start overlapping each other since the particle number exceeds the threshold. For the Voronoi PMA, the threshold is $N_{min} = 15$, and ceil(αN) for the blind method. A good merging algorithm will leave behind no change in the phase space distribution apart from the translation in the x-direction.

or more particles from the different distributions might be merged together. Here, we compare the performance of the Voronoi PMA and the blind method. The merging period $T_{mrg} = 2\Delta t$, with Δt is the time step, is applied for both methods. For the Voronoi PMA, the tolerances are $T_{\mathbf{X}} = 0.4$ and $T_{\mathbf{P}} = 0.01$. For the blind method, we deliberately choose the parameter α so as to give a similar final number of particles as in the Voronoi PMA.

We look at the number of PIC particles appearing in the simulation (see Fig. 6.3a). Starting with 12000 particles, the blind method merges into 4200 particles at the end of the simulation, while the Voronoi PMA finishes the task with approximately 3800 particles. The numbers of particles produced by two methods are approximately equivalent. Fig. 6.4 shows the phase space distributions at the end of the simulation and Figs. 6.3 (b,c, and d) show the

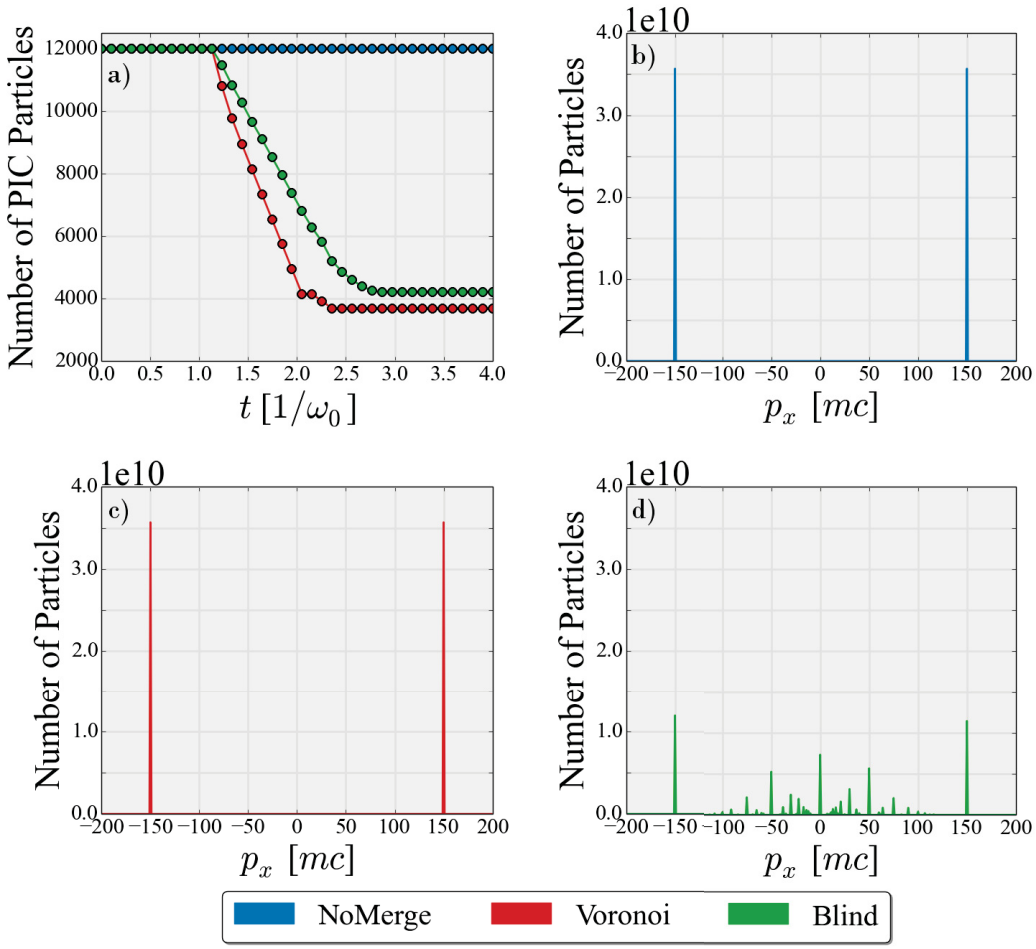

Figure 6.3: The number of PIC particles during the simulation (fig. a) and the histograms for no-merge, the Voronoi PMA, and the blind method (figs. b, c, and d respectively) in the counter-propagating plasma blocks simulation. Despite merging into a similar number of particles, the Voronoi PMA does not distort the momentum distribution.

histogram. For the blind method, we see that after the blocks have passed through each other, there are many particles left behind between the two blocks. The momentum space plot and the histogram shows that these particles have zero momentum. The blind method also produces many particles with momenta not equal to the original magnitude ($150mc$). As a consequence, the particle distributions are smeared and the conservation of energy is vio-

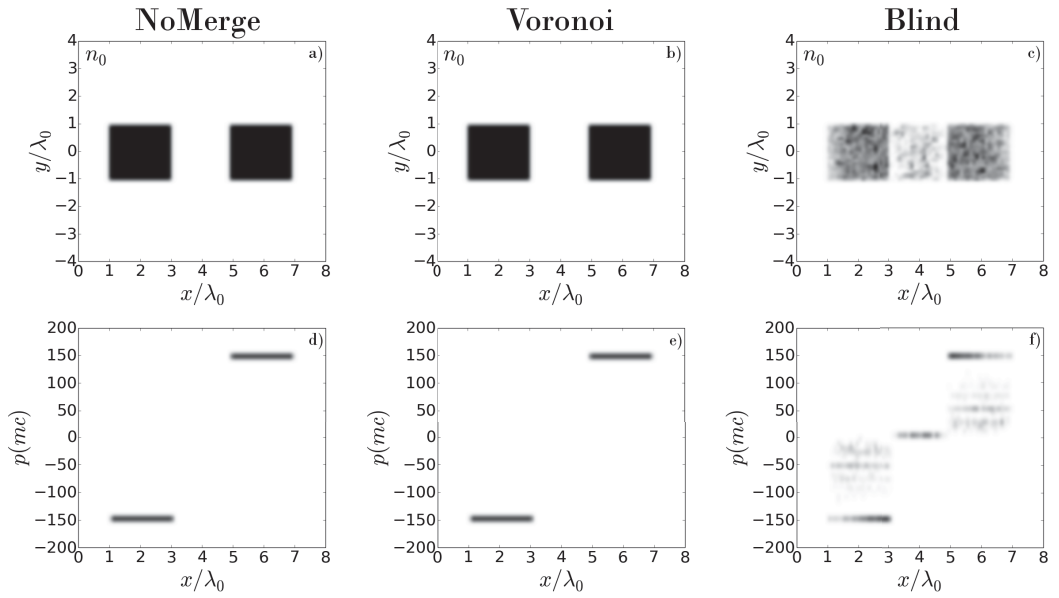

Figure 6.4: The phase space distributions (first row x/y, second row x/p_x) at the end of the counter-propagating blocks simulation. The blind method leaves behind many particles that have zero momentum. Meanwhile, the Voronoi PMA reproduces the result obtained with no merging.

lated. Conversely, the Voronoi PMA accurately preserves the phase space distributions, returning the same result as for the case with no merging. To understand clearly the behaviour of two merging algorithms, we consider Fig. 6.5: two identical particles but with different direction of motion in a same cell.

For the blind method, a typical response is merge two particles together with no caution. According to the conservation of momentum, the newly created particle will have zero momentum and thus its energy is 1 (see Eq. (6.14)). The conservation of energy is outright violated. On the other hand, the Voronoi PMA groups particles by taking into account both the direction and the magnitude of particles' momenta. In the situation of Fig. 6.5, the CVs $\Delta_{\mathbf{P}_0}$ of these two particles will greatly exceed the momentum tolerance

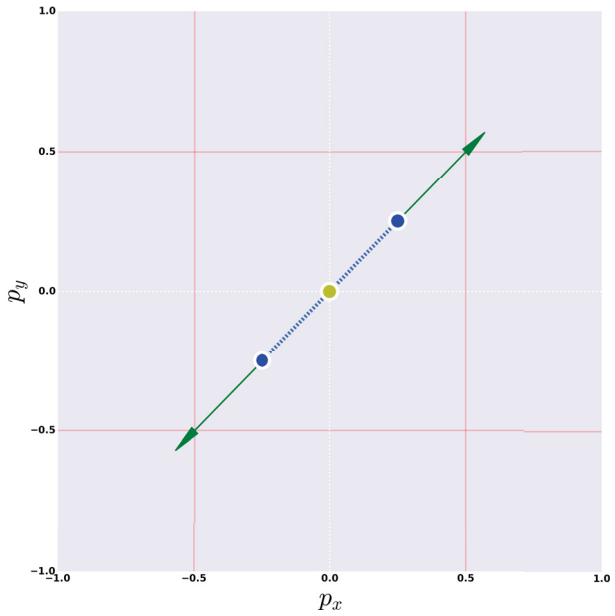

Figure 6.5: A typical problem for PMA: how to merge two identical particles such that the energy and momentum are preserved after the event?

$T_{\mathbf{P}}$. As a consequence, they are recategorise into two different Voronoi groups as in step 5 of section 6.3. Thus, an attempt to merge particles in cases like this is disallowed.

For this test, we see that despite the fact that it finishes the simulation with fewer particles than the blind method, the Voronoi PMA accurately preserves the particle distributions, while the blind method does not.

6.5.2 Two-stream instability

The two-stream instability consists of two identical particle beams streaming through each other. These beams propagate in the opposite directions and a small perturbation in the charge density can change the electric field, which in turn causes further perturbation in the density distributions. This type of

Parameter	Notation	Value	Unit
General Settings			
Wavelength	λ_0	0.8×10^{-4}	cm
Boxlength	$x \times y$	3.2×1.0	λ_0
Gridstep	$dx \times dy$	0.01×0.1	λ_0
Timestep	dt	0.005	λ_0/c
Number of CPUs		8×1	
Electron Settings			
Initial Lorentz factor	γ_0	1.0	
General Merging Settings			
Merging start		5	
Merging period		50	dt
Voronoi Merging Settings			
Minimum particles per cell		200	
Position tolerance	$T_{\mathbf{X}}$	0.8	
Momentum tolerance	$T_{\mathbf{P}}$	0.15	
Blind Merging Settings			
Merging fraction	α	0.965	

Table 6.1: The configuration for the two-stream instability simulation.

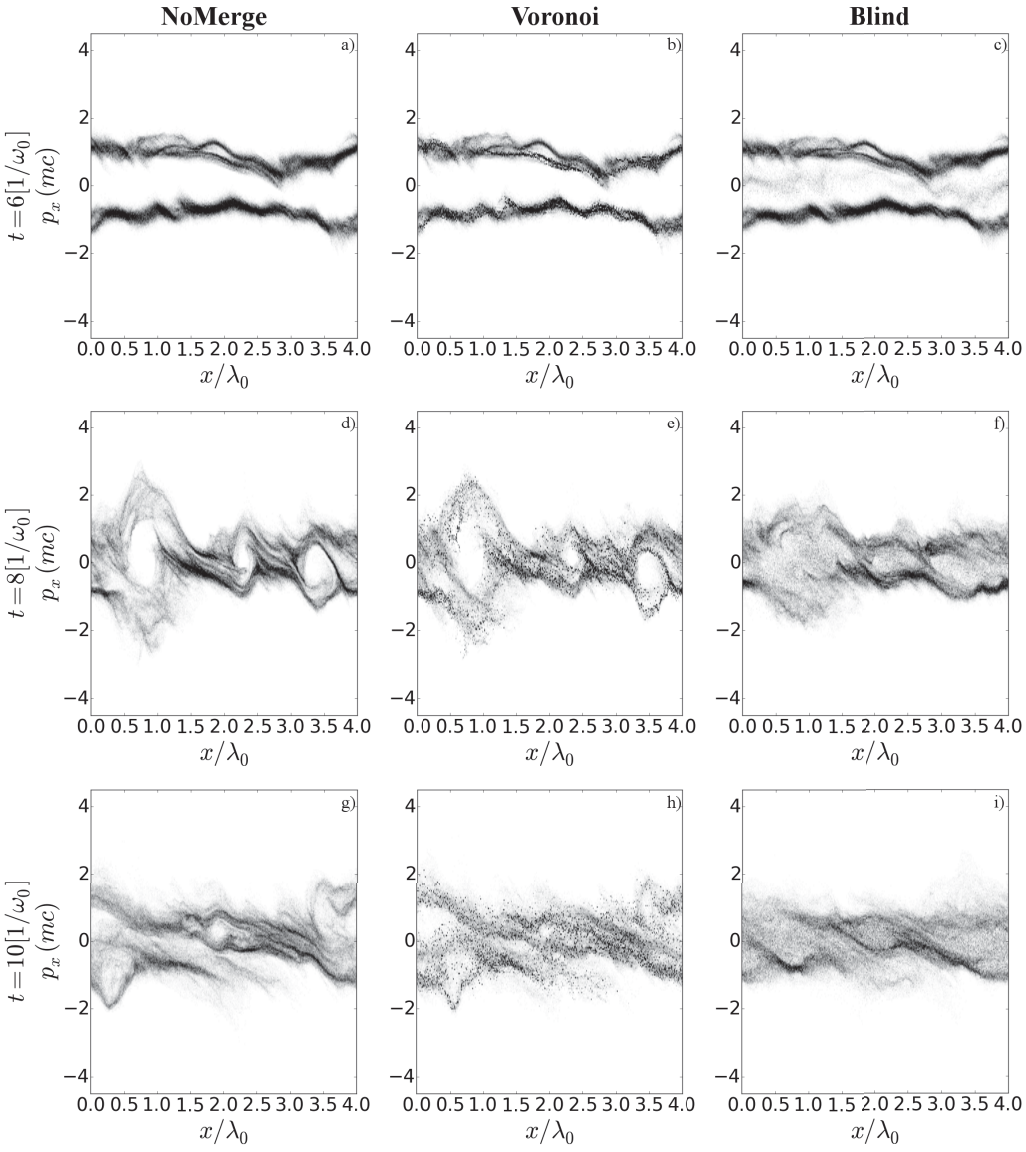

Figure 6.6: The phase space distributions (x/p_x) for the two-stream instability simulation at different time stamps. The first column shows the original simulation with 32×10^4 particles. The second and third columns show the simulation with the blind and Voronoi merging method, respectively. While the outcome produced by the blind method looks different, the Voronoi PMA follows the evolution course as in the no-merging case.

simulation makes an illustrative example of how the algorithm manage merging particles in a dynamic evolution of the phase space. The configuration for the two-stream instability is listed in table 6.1. At the beginning of the simulation, we create two electron beams with the same initial Lorentz factor $\gamma = 1$ but opposite propagation directions. Each beam has 16×10^4 particles and is neutralised by the background charge density. Purposefully, the merging algorithms are only enabled after time $t = 5\lambda_0/c$, when the instability can be visibly observed. The merging fraction for the blind method is chosen to be $\alpha = 0.965$, such that we can have a fair comparison between two algorithms.

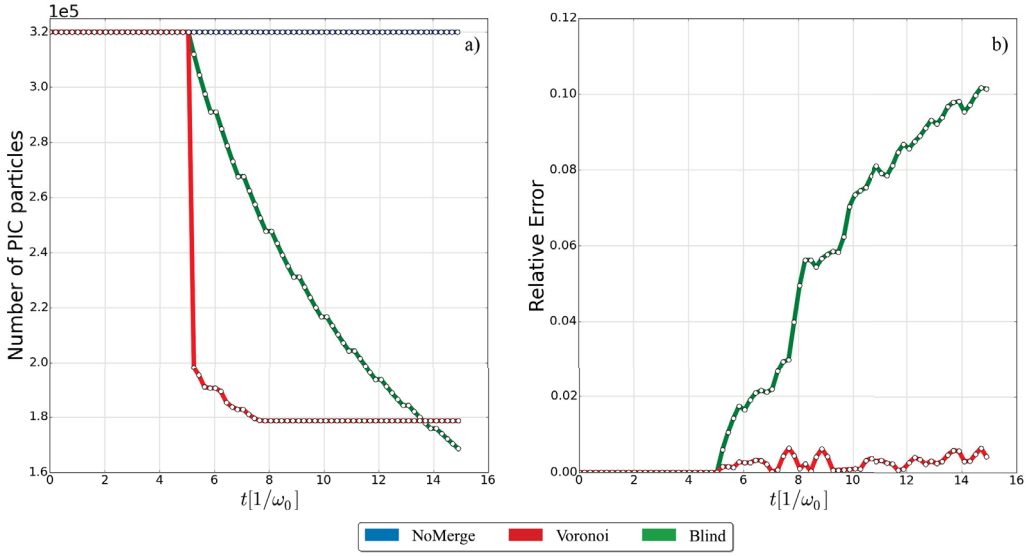

Figure 6.7: The number of PIC particles during the simulation (fig. a) and the relative error in the total energy due to merging events for the two-stream instability simulation. The Voronoi PMA reduces the number of particles from 32×10^4 to 17.8×10^4 particles and stops merging from there, since the number of particles per cell is already below the threshold. The highest relative error in the total energy for the Voronoi PMA is 0.006, and the blind method 0.1.

The phase space distribution (x/p_x) for the two-stream instability is shown in Fig. 6.6 at different time stamps. Similarly to the counter-propagating

plasma blocks, the blind method (the last column) produces many particles with momenta approximately equal to zero, which do not appear in the original simulation (the first column). This early distortion in the phase space distribution leads to a different instability growth at later time. On the other hand, the Voronoi PMA (the second column) retains the phase space distribution throughout the simulation. Moreover, in contrast to the smooth pictures obtained without merging, the outcomes of the two algorithms appear grainier, since there are lesser particles in the phase space due to merging events. Fig. 6.7 shows the number of electrons and the relative error in the total energy $\delta E = \text{abs}(E_0 - E)/E_0$. Here, E_0 is the energy of the system without merging. Observing Fig. 6.7a, we see that when the merging event is enabled (at $t = 5\lambda_0/c$), there is a steep fall in the number of particles for the Voronoi PMA (the red line), falling from 32×10^4 to 20×10^4 particles. This abrupt drop is then followed by a short decline to 17.8×10^4 particles. At around $t = 8\lambda_0/c$, there is almost no merging event till the end of the simulation, since the number of particles per cell is already below the threshold. On the contrary, the blind method (the green line) exhibits a steady decline in the number of particles , reducing to 16.8×10^4 particles at the end of the simulation. From Fig. 6.7b, wee see that the total energy relative error is rising up to 0.1 for the blind method, while the Voronoi PMA reaches a peak at $\delta E = 0.006$ during the simulation.

6.5.3 Magnetic Shower

Introduction

Consider an energetic particle propagating through a strong magnetic field. Due to the interaction with the field, the particle will emit hard photons on its course. In turn, these photons interact with the field and will decay into energetic electron-positron pairs. The cascade of particles develops quickly and an exponential growth of the number of particles is usually observed. This phenomena is called the magnetic shower. The occurrence of the magnetic shower requires both an intense field and high particle energies [70] [71]. This condition is quantified in the quantum parameter χ [70], which is defined as

$$\chi = \gamma \frac{B}{B_S}. \tag{6.20}$$

Here, γ is the particle's Lorentz factor, B the magnetic field strength, and the Schwinger field $B_S = 4.41 \times 10^{13}$ G. The pair production has sufficient probability to start the cascade process only when $\chi \geq 0.1$ [70]. The probability rates for photon emission and pair production are expressed in intricate expressions (see eq. (2) and (3) in ref. [72] and the description therein). The computation usually requires solving the double integral of the Airy function. Thus, the task involves a significant computational overhead. However, under the assumption that the dimensionless field amplitude $a_0 \gg 1$, the field can be regarded as being constant during the decay processes. Additionally, if both conditions $\chi \gg B/B_S$ and $B \ll B_S$ are satisfied, we can utilise the theory of quantum processes under a constant cross field given in [73] [74]. According

to this theory, the probability rates for the photon emission W_{em} and pair production W_{pair} are

$$W_{em} = \frac{\alpha}{3\sqrt{3}\pi}\frac{mc^2}{\hbar\gamma}\int_0^1 \frac{5x^2+7x+7}{(1+x)^3}K_{2/3}\left(\frac{2x}{3\chi}\right)\mathrm{d}x \tag{6.21}$$

and

$$W_{pair} = \frac{\alpha}{3\sqrt{3}\pi}\frac{m^2c^4}{\hbar\varepsilon}\int_0^1 \frac{9-x^2}{1-x^2}K_{2/3}\left(\frac{8}{3(1-x^2)\kappa}\right)\mathrm{d}x. \tag{6.22}$$

Here, α is the fine structure constant; $K_{2/3}(x)$ is the modified Bessel function of the second kind; ε is photon's energy and κ its quantum parameter. Our numerical model for the cascade process is based on the Monte Carlo method [72] [75].

The magnetic shower is an appropriate example since the number of particles can grow exponentially during the simulation and the particles' energies can range from several to hundred MeVs. Thus, it is a good indicator of how a PMA copes with the dynamic development during the simulation while preserving the physical features of the system.

Simulation

The simulation configuration for the magnetic shower is listed in table 6.2. We begin the simulation with 5 numerical electrons. For an electron with a Lorentz factor $\gamma = 5 \times 10^4$ and a magnetic field $eB/m_e c\omega = 500$, the quantum parameter is $\chi \approx 150 \gg 1$. Here, e is the elementary charge, m_e the electron mass, c the velocity of light, and $\omega = 2\pi c/\lambda_0$. As before, we consider

three cases: without merging, with the blind merging method, and with the Voronoi algorithm. As before we deliberately choose the merging fraction α such that the blind method and the Voronoi PMA result in the similar number of particles at the end of the simulation.

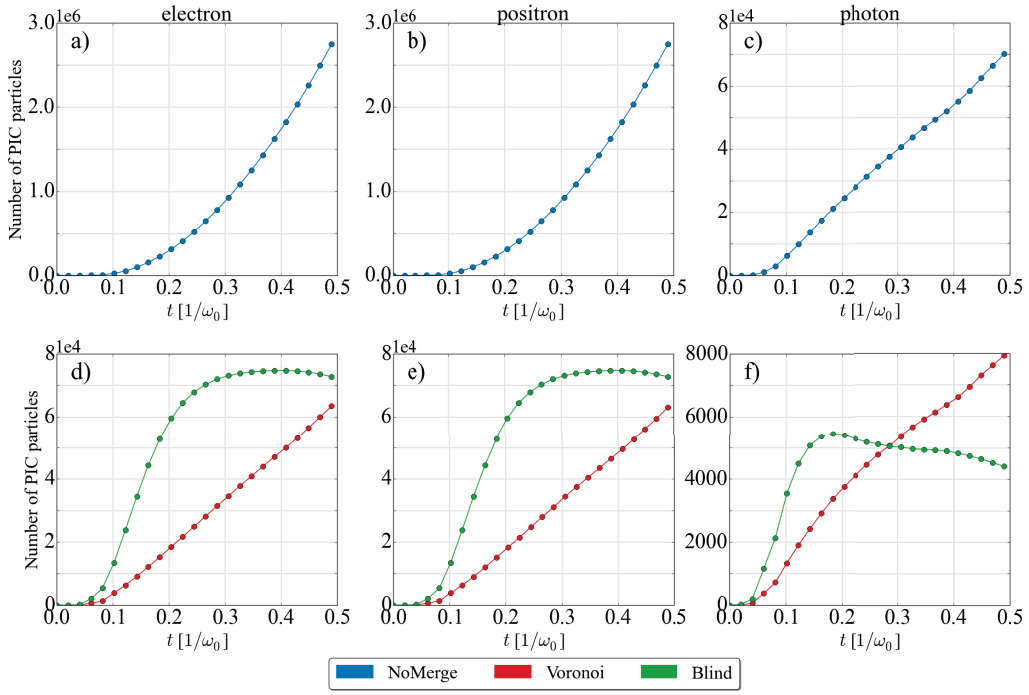

Figure 6.8: The number of particles in the magnetic shower simulation as a function of time for electron, positron, and photon (from left to right). The first row shows the result from the simulation without merging, the second row shows the outcome by using the Voronoi PMA (red) and the blind method (green). The Voronoi PMA reduces the number of electrons (positrons) from 2.8×10^6 to 6.5×10^4 particles.

The growth in particle number is shown in Fig. 6.8. Without merging (blue), both electron and positron display exponential growth during the simulation. At the end of the simulation, a total number of 2.8×10^6 particles has been reached for each specie. Meanwhile, the photon specie grows from 0 to 7×10^4 particles at the last frame. The blind method (green) results in

Parameter	Notation	Value	Unit
	General Settings		
Wavelength	λ_0	0.8×10^{-4}	cm
Boxlength	$x \times y \times z$	$3.2 \times 3.2 \times 3.2$	λ_0
Gridstep	$dx \times dy \times dz$	$0.04 \times 0.04 \times 0.04$	λ_0
Timestep	dt	0.005	λ_0/c
Number of CPUs		$5 \times 5 \times 5$	
	Electron Settings		
Initial Lorentz factor	γ_0	5×10^4	
	External Field Settings		
Magnetic field strength	B_X	6.6×10^{10}	G
	General Merging Settings		
Merging start		0	
Merging period		2	dt
	Voronoi Merging Settings		
Minimum particles per cell		10	
Position tolerance	$T_{\mathbf{X}}$	1.0	
Momentum tolerance	$T_{\mathbf{P}}$	0.02	
	Blind Merging Settings		
Merging fraction	α	0.88	

Table 6.2: The configuration for the magnetic shower simulation.

1.45×10^5 electrons and posittrons, 4000 photons. The Voronoi PMA (red) produces in total 1.35×10^5 electrons and positrons, and 8000 photons. That is, the number of particles in the box is reduced approximately 40 times by both methods. In order to verify the validity of the simulation, we look at the total energy and the spectra of the particles. Figs. 6.9 and 6.10 illustrate the evolution of the particle energies and their spectra at the end of the simulation. For the blind method (solid, green line in Fig. 6.9), we see a gradual decrease in the total energy of electrons and positrons around the point when the photon energy is reaching its peak. This strongly affects the spectrum of every specie in the simulation box (see Figs. 6.10 g, h, i): the distinct peak electrons and positrons is not observed. On the other hand, with a careful approach the Voronoi PMA (short dash, black line) overlaps the case with no merging (long dash, light blue)in Fig. 6.9, showing that it preserves the physical behaviour in the total energy, with the decrease in electron energy, increase in positron energy, and the sharp rise followed by a decrease in photon energy. Moreover, the Voronoi PMA accurately reproduces the spectra obtained with no merging (see Figs. 6.10 d, e, and f). Originally, the simulation with no merging takes approximately 2 hours (7265 seconds). With the same settings, the Voronoi PMA completes roughly in 20 minutes (1172 seconds) and the blind method takes about 24 minutes (1440 seconds).

Finally, we perform a parameter scan on the tolerances $T_{\mathbf{X}}$ and $T_{\mathbf{P}}$ in order to observe the growth of particles and the accumulation of error due to merging. Fig. 6.11 shows the number of electrons and the relative error $\delta E = (E_0 - E)/E_0$ during the simulation and Fig. 6.12 displays the total computation time with various tolerance settings. Here, E_0 is the energy of the

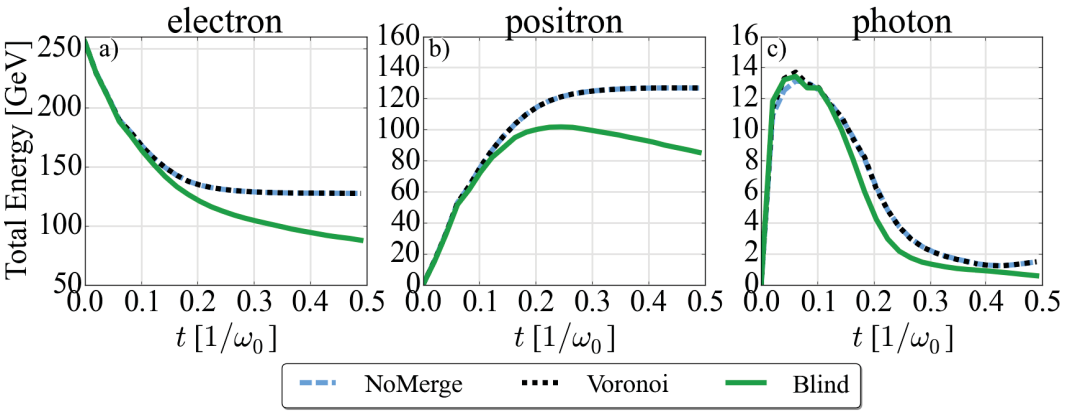

Figure 6.9: The total energy evolution of electron, positron, and photon during the magnetic shower simulation for three merging cases: no-merge case (long dash, light blue); Voronoi (short dash, black), and blind (solid, green). Unlike the blind method, the Voronoi PMA reproduces the results obtained from the original simulation.

system without merging. The most accurate simulation is achieved with $T_{\mathbf{X}} = 0.5$ and $T_{\mathbf{P}} = 0.005$. With this setting, the simulation takes roughly 40 minutes to complete and the total energy loss is around 0.05 MeV ($\delta E \approx 1 \times 10^{-7}$). We observe that the growth is also exponential and the number of electrons has reached 2.4×10^5 particles at the end of the simulation. When we loosen the tolerances, more particles are merged together. As a result, the growth rate becomes more linear but the energy loss develops speedily. In our test, the extreme case with $T_{\mathbf{X}} = 1.0$ and $T_{\mathbf{P}} = 0.03$ produces 7.7×10^4 electrons and positrons, 5×10^3 photons, and takes 14 minutes to finish. However, in this case, it accumulates 20 MeV total energy loss ($\delta E \approx 3.9 \times 10^{-5}$). Although the loss is extremely small, we notice the double in magnitude just by increasing from $T_{\mathbf{P}} = 0.025$ to $T_{\mathbf{P}} = 0.03$. We also observe that, the purple line ($T_{\mathbf{X}} = 0.5$ and $T_{\mathbf{P}} = 0.02$) completely overlaps the dark blue line ($T_{\mathbf{X}} = 1.0$ and $T_{\mathbf{P}} = 0.02$), showing that the tolerance $T_{\mathbf{P}}$ is more sensitive than $T_{\mathbf{X}}$. Since, in a given cell, the particle momenta may vary significantly, an accurate simulation requires

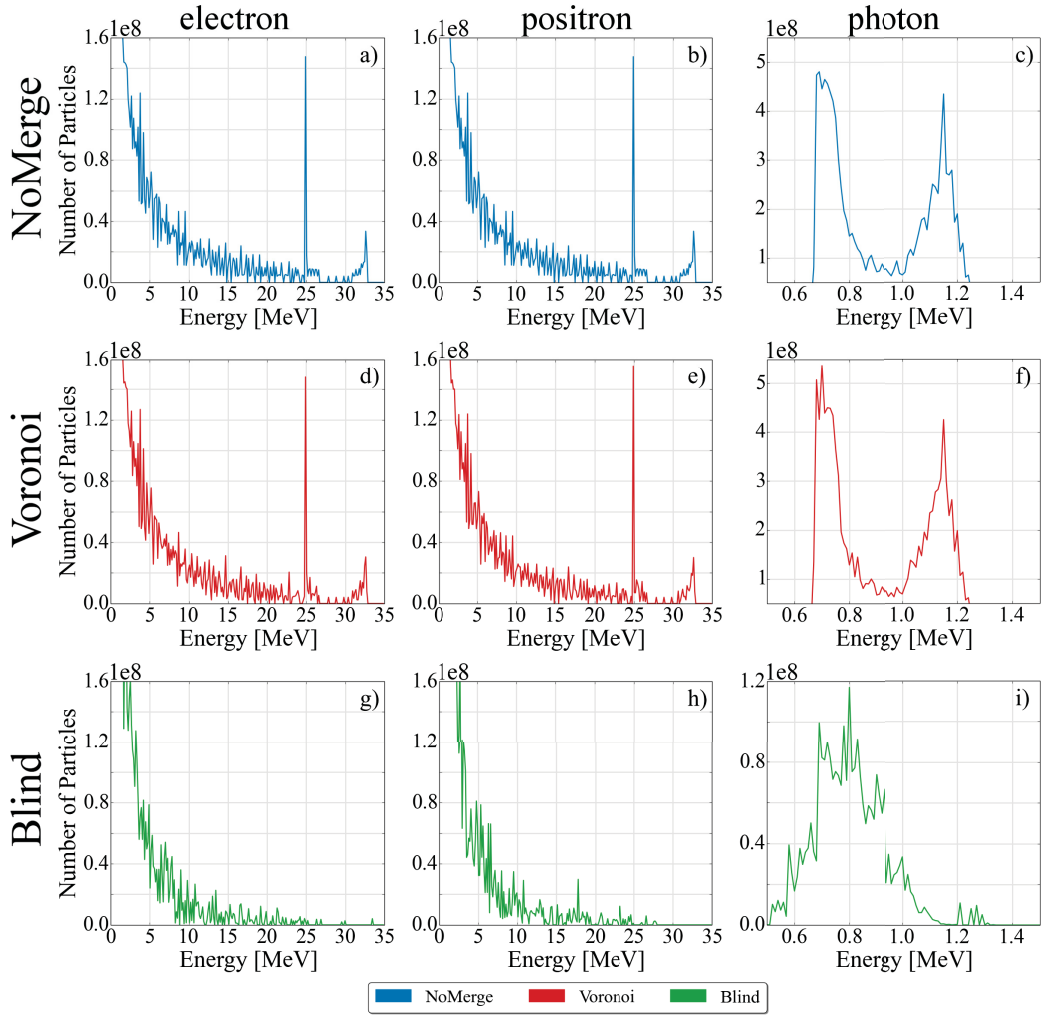

Figure 6.10: The spectra for the electron, positron, and photon species in the magnetic shower simulation at time $t = 98\Delta t$ for three merging cases: no merge (blue), the Voronoi PMA (green), and the blind method(red). The spectra of particles are accurately reproduced by using the Voronoi PMA. Meanwhile, with the blind method, the distinct peak for electrons and positrons is not observed.

small $T_{\mathbf{P}}$. We recommend $T_{\mathbf{P}} = 0.05$ and $T_{\mathbf{X}} = 1.0$ as a threshold for this type of simulation.

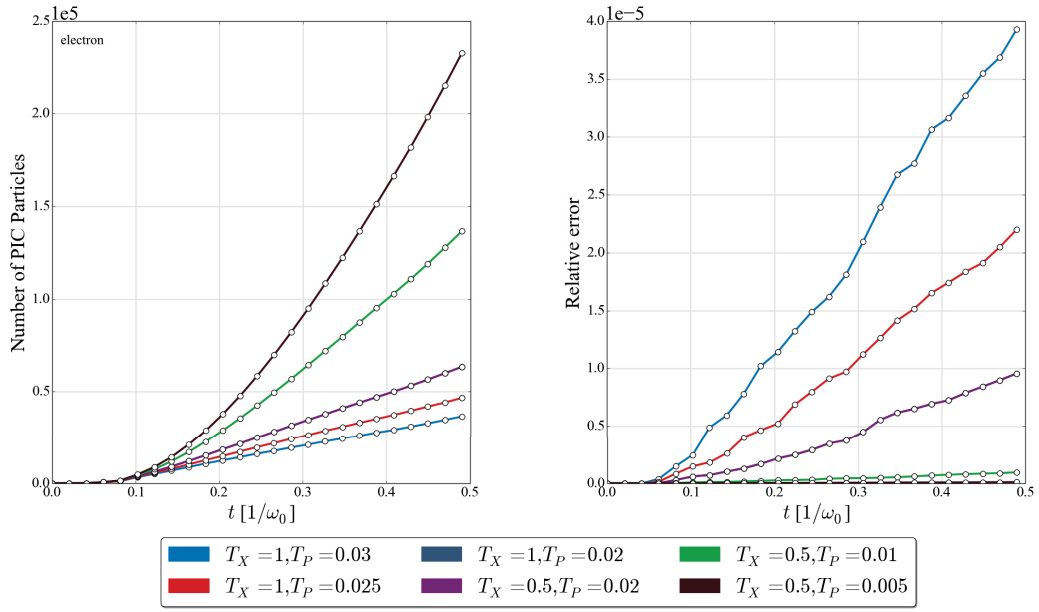

Figure 6.11: The number of electron and the relative error in the total energy due to merging with various tolerances $[T_{\mathbf{X}}, T_{\mathbf{P}}]$ settings for the magnetic shower simulation. With relaxed tolerances, the growth of particle number becomes linear but the error also accumulates faster. When stricter tolerances are used, the growth resumes the exponential behaviour while the error develops with a slower rate. We also observe that, the purple line ($T_{\mathbf{X}} = 0.5$ and $T_{\mathbf{P}} = 0.02$) completely overlaps the dark blue line ($T_{\mathbf{X}} = 1.0$ and $T_{\mathbf{P}} = 0.02$), showing that the algorithm is always more sensitive towards the momentum space.

6.6 Summary

In this chapter, we present the Voronoi particle merging algorithm for PIC codes. The phase space of a simulation cell is partitioned, as in the Voronoi diagram, into smaller subsets, which only consist of particles that are close

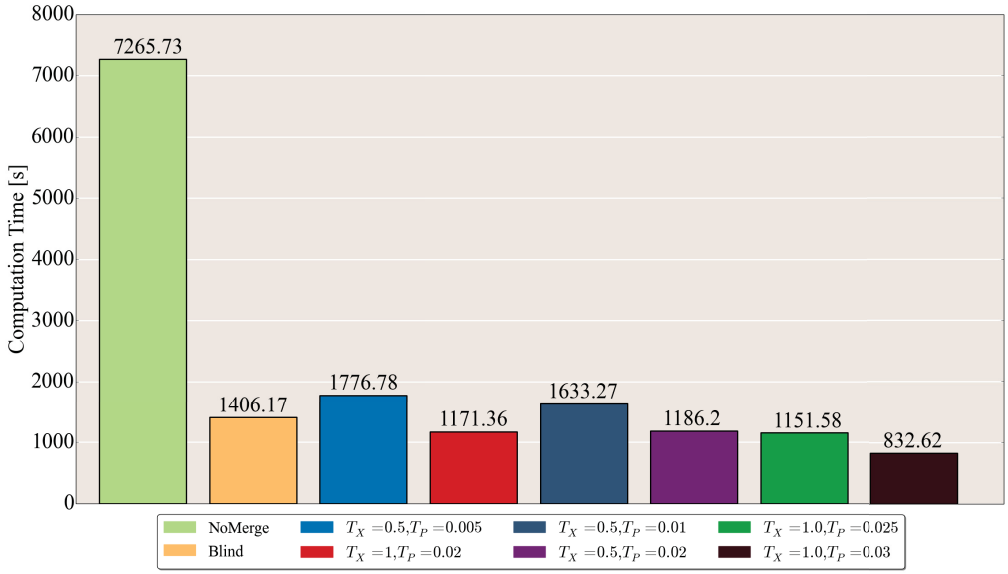

Figure 6.12: The total computation time for the magnetic shower simulation. The last six columns show the simulations with the Voronoi PMA for various tolerances $[T_{\mathbf{X}}, T_{\mathbf{P}}]$ settings.

to each other. The quality of a merging event is ensured by two user inputs, the tolerances on position $T_{\mathbf{X}}$ and momentum $T_{\mathbf{P}}$. The tolerances act as the balance between the speed-up and the accuracy of the simulation. Stricter tolerances mean smaller error but without much in the speed-up. On the other hand, relaxed tolerances result in more merged particles and thus the computation time decreases but the error will accumulate faster. Making a right combination for the tolerance pair for a certain simulation requires prior knowledge of particles' behaviour. If a simulation involves particles which spread out in a large range in the momentum space, we suggest keeping the $T_{\mathbf{P}}$ lower than 0.02. Otherwise, this value can be relaxed. On the other hand, since it relates to particles' relative position in a cell, $T_{\mathbf{X}}$ can be chosen up to 1.0.

We have tested the performance of our algorithm with three tests: the

counter-propagating plasma blocks, the two-stream instability and magnetic shower simulations. In all cases, we observe that the conservation of momentum is perfectly held and the conservation of energy is maintained extremely well, with only small margin of error. The two-stream instability shows that the Voronoi PMA preserves the phase space evolution and the total energy error in this case is of the order of 10^{-3}. In the magnetic shower simulation, the total energy error is of the order of 10^{-5} with a speed-up by a factor of 6 and the spectra of particles are also comparable very well to those obtained with no merging.

CHAPTER 7

Conclusion and Outlook

In the first part of this thesis, we have proposed a new scheme of particle acceleration in periodic structures. The detailed illustration of the scheme is given in chapter 4. The accelerator design consists of multiple identical shielding blocks which are separated from each other by half the laser wavelength. Each block has a cylindrical hole at the centre to support the particle beam's propagation. The main objective of the shielding blocks is to restrict the interaction length between the particles and the lasers: the particles only experience the accelerating field while the effect of the negative phase is negated by the blocks. The scheme is then evaluated by using the PIC simulation method. The outcome is presented in chapter 5. From the simulation results, we observe that the scheme is capable of accelerating the electrons with high acceleration gradient, up to 136.64 GeV/m over a short distance of 76.8×10^{-4} cm. With the advantage of being compact, the structure can serve as a module of a multi-stage acceleration scheme.

However, there is an inherent problem in the scheme. The complication

lies in the field perturbation due to the ionisation of the structure. This is demonstrated in section 5.3. Although the acceleration gradient scales linearly with the laser intensity, higher intensities ionises the structure faster and thus the perturbation has more space to grow. This disturbance is the main cause of particles deflecting away from the shielding hole. At the end of the simulations, only about 20% of particles get trapped inside the hole. Thus, future works would involve explore the choice of material for a certain laser parameters in order to improve the efficiency of trapping particles in the structure. Besides, due to storage limitations, we were only able to perform simulations in 12 structure periods. The extension of the simulation time would be beneficial to studying the acceleration process and particle movement in detail. Apart from this, the most challenging part is bringing the proposal to experimental tables.

In the conclusion of chapter 5, we suggest to use heavier materials for the construction of the structure to mitigate the disturbance by the ionisation process. It is likely that there would be more electrons generated in the simulation box which can stretch the computation time. Thus, the second part of the thesis is devoted to the design of the Voronoi particle merging algorithm as a pre-emptive step for this matter. In our algorithm, the particles are grouped together based on their proximity in the phase space attributed to the Voronoi tessellation method. The algorithm is comprehensibly presented in chapter 6. We have tested the algorithm in various practical situations: counter-propagating plasma blocks, two-stream instability, and magnetic shower. In all case studies, the algorithm has displayed the capability and competence of merging particles and boosting the computation time while preserving the

physical description of the system. The total energy error is ranging between 10^{-3} and 10^{-5}. In the case of magnetic shower, the computation time was boosted up to a factor of 6.

Nevertheless, the development of the algorithm doesn't stop here. The next step would comprise the refinement of energy conservation. There are two possible approaches: using the Langdon-Marder scheme or merging into two particles. Another great upgrade is to provide users an array of justifiable candidates of the tolerance pair for each simulation case. As shown in the simulation, the choice of the tolerances in one case might not be applicable to the other. The Bayesian treatment would be a valuable tool to achieve this task.

APPENDIX A

List of own Publications

- L. Yi, A. Pukhov, P. Luu-Thanh, and B. Shen, "Bright X-ray source from a laser-driven micro-plasma waveguide", *Physical Review Letters*, vol. 116, no. 11, 115001, 2016.
- P. T. Luu, T. Tückmantel, and A. Pukhov, "Voronoi particle merging algorithm for PIC code", *Computer Physics Communications*, vol. 999, pp. 88-99, 2016.
- P. Luu-Thanh, T. Tückmantel, A. Pukhov, and I. Kostyukov, "Laser fields in dynamically ionized plasma structures for coherent acceleration", *The European Physical Journal Special Topics*, vol. 224, no. 13, pp. 2625-2629, 2015.
- A. Pukhov, I. Kostyukov, T. Tückmantel, P. Luu-Thanh, and G. Mourou, "Coherent acceleration by laser pulse echelons in periodic plasma structures", *The European Physical Journal Special Topics*, vol. 223, no. 6, pp. 1197-1206, 2014.

Bibliography

[1] B. Carithers and P. Grannis, "Discovery of the top quark," *Beam Line (SLAC)*, vol. 25, no. 3, pp. 4–16, 1995.

[2] E. D. Bloom and et al., "High-energy inelastic e-p scattering at 6° and 10°," *Physical Review Letters*, vol. 23, no. 16, pp. 930–934, 1969.

[3] P. W. Higgs, "Broken symmetries, massless particles and gauge fields," *Physics Letters*, vol. 12, no. 2, pp. 132–201, 1964.

[4] G. Aad and et al., "Observation of a new particle in the search for the Standard Model Higgs boson with the ATLAS detector at the LHC," *Physics Letter B*, vol. 716, no. 1, pp. 1–29, 2012.

[5] G. A. Loew, "Linear collider systems and costs," in *Proceedings of the 1993 Particle Accelerator Conference* (S. T. Corneliussen and L. Carlton, eds.), (Washington DC), 1993.

[6] C. Nieter, "VORPAL: a versatile plasma simulation code," *Journal of Computational Physics*, vol. 196, no. 2, pp. 448–473, 2004.

[7] R. J. England and et al., "Dielectric laser accelertors," *Reviews of Modern Physics*, vol. 86, no. 4, pp. 1337–1389, 2014.

[8] P. M. Woodward, "A method of calculating the field over a plane aperture required to produce a given polar diagram," *Journal of the Institution of Electrical Engineers - Part IIIA*, vol. 93, pp. 1554–1588, 1947.

[9] J. D. Lawson, "Lasers and accelerators," *IEEE Transaction on Nuclear Science*, vol. 26, no. 3, pp. 4217–4219, 1979.

[10] T. Tajima and J. M. Dawson, "Lasers electron accelerator," *Physical Review Letters*, vol. 43, no. 4, p. 263, 1979.

[11] C. Joshi, B. Mori, J. M. Dawson, J. M. Kindel, and D. W. Forslund, "Ultrahigh gradient particle acceleration by intense laser-driven plasma density waves," *Nature*, vol. 311, pp. 525–529, 1984.

[12] W. P. Leemans and et al., "Multi-GeV electron beams from capillary-discharge-guided subpetawatt laser pulses in the self-trapping regime," *Physical Review Letters*, vol. 113, no. 25, p. 245002, 2014.

[13] E. Esaray, C. B. Schroeder, and W. P. Leemans, "Physics of laser-driven plasma-based electron accelerators," *Review of Modern Physics*, vol. 81, pp. 1229–1285, 2009.

[14] A. Pukhov and J. M. ter Vehn, "Laser wakefield acceleration: the highly non-linear broken-wave regime," *Applied Physics B*, vol. 74, pp. 355–361, 2002.

[15] J. Faure, Y. Glinec, A. Pukhov, S. Kiselev, S. Gordienko, E. Lefebvre, J.-P. Rousseau, F. Burgy, and V. Malka, "A laser-plasma accelerator producing monoenergetic electron beams," *Nature*, vol. 431, pp. 541–544, 2004.

[16] C. Geddes, "Laser wakefield accelerator physics and development," *Presentation at HEDSA, APS DPP*, 2008.

[17] N. Kirby and et al., "Energy measurements of trapped electrons from a plasma wakefield accelerator," *AIP Conf. Proc.*, vol. 877, pp. 541–546, 2006.

[18] M. Litos and et al., "High-efficiency acceleration of an electron beam in a plasma wakefield accelerator," *Nature*, vol. 515, pp. 92–95, 2014.

[19] Y. Takeda and I. Matsui, "Laser linac with grating," *Nuclear Instruments and Methods*, vol. 62, no. 3, pp. 306–310, 1968.

[20] K. Mizuno, S. Ono, and O. Shimoe, "Interaction between coherent ligth waves and free electrons with a reflection grating," *Nature*, vol. 253, pp. 184–185, 1975.

[21] D. Du, X. Liu, G. Korn, J. Squier, and G. Mourou, "Laser-induced breakdown by impact ionization in sio2 with pulse widths from 7ns to 150fs," *Applied Physics Letters*, vol. 64, pp. 3071–3073, 1994.

[22] K. Soong, E. R. Colby, C. McGuinness, R. L. Byer, and R. J. England, "Experimental determination of damage threshold characteristics of IR compatible optical materials," in *Proceedings of 2011 Particle Acclerator Conference* (T. Satogata and K. Brown, eds.), vol. 1, (Melville, New York), pp. 277–279, Devision of Physics Beam, IEEE, April 2011.

[23] T. Plettner, P. P. Lu, and R. L. Byer, "Proposed few-optical cycle laser driven particle accelerator structure," *Physical Review Accelerators and Beams*, vol. 9, no. 11, p. 111301, 2006.

[24] E. A. Peralta and et al., "Demonstration of electron acceleration in a laser driven dielectric microstructure," *Nature*, vol. 503, no. 7474, pp. 91–94, 2013.

[25] J. Breuer and P. Hommelhoff, "Laser-based acceleration of nonrelativistic electrons at a dielectric structure," *Physical Review Letters*, vol. 111, no. 13, p. 134803, 2013.

[26] J. Breuer, *Dielectric laser acceleration of non-relativistic electrons at a photonic structure*. PhD thesis, Ludwig-Maximilians-Universität, July 2013.

[27] A. J. Kemp, R. E. W. Pfund, and J. M. ter Vehn, "Modeling ultrafast laser-driven ionization dynamics with (Monte Carlo) collisional particle-in-cell simulations," *Physics of Plasmas*, vol. 11, pp. 5648–5657, 2004.

[28] L. V. Keldysh, "Ionization in the field of a strong electromagnetic wave," *Soviet Physics JETP*, vol. 20, pp. 1307 – 1314, 1965.

[29] V. S. Popov, "Tunnel and multiphoton ionization of atoms and ions in a strong laser field (Keldysh theory)," *Physics - Uspekhi*, vol. 47, pp. 855–885, 2004.

[30] D. Ristau, *Laser-induced damage in optical materials*. Tylor & Francis Inc, December 2014.

[31] M. Chen, E. Cormier-Michel, C. Geddes, D. Bruhwiler, L. Yu, E. Esarey, C. Schroeder, and W. Leemans, "Numerical modeling of laser tunneling ionization in explicit particle-in-cell codes," *Journal of Computational Physics*, vol. 236, pp. 220–228, 2013.

[32] M. V. Ammosov, N. B. Delone, and V. P. Krainov, "Tunnel ionization of complex atoms and atomic ions in electromagnetic field," *Sov. Phys. JETP*, vol. 64, pp. 1191–1194, December 1986.

[33] J. Buon, "Beam phase space and emittane," in *CAS - CERN Accelerator School: 5th General Accelerator Physics Course* (S. Turner, ed.), (CERN, Geneva), pp. 89–116, CERN Accelerator School, CERN, September 1992.

[34] M. Raiser, *Theory and Design of Charged Particle Beams.* Wiley VCH, 2008.

[35] O. Buneman, "Dissipation of currents in ionized media," *Physical Review*, vol. 115, no. 3, pp. 503–517, 1959.

[36] J. Dawson, "One-dimensional plasma model," *Physics of Fluid*, vol. 5, no. 445, pp. 445–459, 1962.

[37] J. Villasenor and O. Buneman, "Rigorous charge conservation for local electromagnetic field solvers," *Computer Physics Communication*, vol. 69, pp. 306–316, 1992.

[38] A. Pukhov, "Three-dimensional electromagnetic relativistic particle-in-cell code VLPL (Virtual Laser Plasma Lab)," *Journal of Plasma Physics*, vol. 61, pp. 425–433, 1999.

[39] C. K. Birdsall and A. B. Langdon, *Plasma Physics via Computer Simulation.* CRC Press, October 2004.

[40] A. Pukhov, "Particle-in-Cell Codes for Plasma based Particle Acceleration," in *Proceedings of the CAS-CERN Acceleratior School: Plasma Wake Acceleration* (B. Holzer, ed.), vol. 1, (CERN, Geneva), pp. 181–206, 2016.

[41] J. D. Jackson, *Classical Electrodynamics*. John Wiley & Sons, 1998.

[42] K. S. Yee, "Numerical solution of initial boundary value problems involving Maxwell's equations in isotropic media," *IEEE Trans. Antennas Propagat.*, vol. 14, pp. 302–307, 1966.

[43] A. Taflove and S. C. Hagness, *Computational electrodynamics: the finite-difference time-domain method*. Artech House, 2005.

[44] B. Fomberg, "Some numerical techniques for Maxwell's equations in different types of geometries," in *Topics in Computational Wave Propagation: Direct and Inverse Problems* (M. Aisworth, P. Davies, D. Duncan, P. Martin, and B. Rynne, eds.), ch. 7, pp. 265–299, Springer, 2013.

[45] J. P. Boris, "Relativistic plasma simulation-optimization of a hybrid code," in *Proceedings of the 4th Conference on Numerical Simulation of Plasmas* (R. Zgadzaj, E. Gaul, and M. C. Downer, eds.), (Washington DC), pp. 3–67, Naval Research Laboratory, 1970.

[46] A. A. Vlasov, *Many-Particle Theory and its Application to Plasma*. Gordon & Breach Science Publishers, 1961.

[47] T. Tückmantel, *Hyrid particle-in-cell simulations of relativistic plasmas*. PhD thesis, Heinrich-Heine Universität, July 2012.

[48] A. Pukhov, I. Kostyukov, T. Tückmantel, P. Luu-Thanh, and G. Mourou, "Coherent acceleration by laser pulse echelons in periodic plasma structures," *The European Physical Journal Special Topics*, vol. 223, no. 6, pp. 1197–1206, 2014.

[49] B. Shen and M. Y. Yu, "High-intensity laser-field amplification between two foils," *Physical Review Letters*, vol. 89, no. 275004, 2002.

[50] J. Bauer, A. Schroer, R. Schwaiger, and O. Kraft, "Approaching theoretical strength in glassy carbon nanolattices," *Nature Materials*, vol. 2016, 2016.

[51] G. Mourou, B. Brocklesby, T. Tajima, and J. Limpert, "The future is fibre accelerators," *Nature Photonics*, vol. 7, pp. 258–261, 2013.

[52] K. Soong, R. L. Byer, E. R. Colby, R. J. England, and E. A. Peralta, "Laser damage threshold measurements of optical materials for direct laser accelerators," in *Laser damage threshold measurements of optical materials for direct laser accelerators* (R. Zgadzaj, E. Gaul, and M. C. Downer, eds.), vol. 1507, (Melville, New York), pp. 511–515, Department of Energy, AIP Conference Proceedings, June 2012.

[53] P. T. Luu, T. Tückmantel, and A. Pukhov, "Voronoi particle merging algorithm for PIC code," *Computer Physics Communications*, vol. 999, pp. 88–99, 2016.

[54] J. M. Dawson, "Particle simulation of plasmas," *Reviews of Modern Physics*, vol. 55, no. 2, pp. 403–447, 1983.

[55] A. N. Timokhin, "Time-dependent pair cascades in magnetospheres of neutron stars–I. Dynamics of the polar cap cascade with no particle supply from the neutron star surface," *Monthly Notices of the Royal Astronomical Society*, vol. 408, pp. 2092–2114, 2010.

[56] G. Lapenta and J. U. Brackbill, "Dynamic and selective control of the number of particles in kinetic plasma simulations," *Journal of Computational Physics*, vol. 115, no. 1, pp. 213–227, 1994.

[57] G. Lapenta, "Particle rezoning for multidimensional kinetic particle-in-cell simulations," *Journal of Computational Physics*, vol. 181, no. 1, pp. 317–337, 2002.

[58] J. Teunissen and U. Ebert, "Controlling the weights of simulation particles: adaptive particle management using k-d trees," *Journal of Computational Physics*, vol. 259, pp. 318–330, 2014.

[59] M. Vranic, T. Grismayer, J. L. Martins, R. A. Fonseca, and L. O. Silva, "Particle merging algorithm for PIC codes," *Computer Physics Communications*, vol. 191, pp. 65–73, 2015.

[60] G. Voronoi, "Nouvelles applications des paramètres continus à la théorie des formes quadratiques," *Journal für die Reine und Angewandte Mathematik*, vol. 133, no. 133, pp. 97–178, 1908.

[61] R. A. Dwyer, "Higher-dimensional Voronoi diagrams in linear expected time," *Discrete & Computational Geometry*, vol. 6, no. 1, pp. 343–367, 1991.

[62] T. Schreiber, "A Voronoi diagram based adaptive k-means-type clustering algorithm for multidimensional weighted data," in *Computational Geometry-Methods, Algorithms and Applications* (H. Bieri and H. Noltemeier, eds.), Berlin: Springer Berlin Heidelberg, 1991.

[63] K. V. Mardia, J. T. Kent, and J. M. Bibby, *Multivariate Analysis*. Academic Press, January 1980.

[64] D. Pelleg and A. Moore, "X-means: extending k-means with efficient estimation of the number of clusters," in *Proceedings of the 17th International Conf. on Machine Learning*, Morgan Kaufmann Publishers, 2000.

[65] H. Bischof, A. Leonardis, and A. Selb, "MDL principle for robust vector quantisation," *Pattern Analysis & Applications*, vol. 2, no. 1, pp. 59–72, 1999.

[66] A. B. Langdon, "On enforcing Gauss' law in electromagnetic particle-in-cell codes," *Computer Physics Communications*, vol. 70, no. 3, pp. 447–450, 1992.

[67] J. Wang, D. Zhang, C. Liu, Y. Li, Y. Wang, H. Wang, H. Qiao, and X. Li, "UNIPIC code for simulations of high power microwave devices," *Physics of Plasma*, vol. 16, no. 033108, pp. 1–10, 2009.

[68] J. Wang, Z. Chen, Y. Wang, D. Zhang, C. Liu, Y. Li, H. Wang, H. Qiao, M. Fu, and Y. Yuan, "Three-dimensional parallel UNIPIC-3D code for simulations of high power microwave devices," *Physics of Plasma*, vol. 17, no. 073107, pp. 1–10, 2010.

[69] J. A. Bittencourt, *Fundamentals of Plasma Physics, Third Ed.* Springer-Verlag, New York, 2004.

[70] V. Anguelov and H. Vankov, "Electromagnetic showers in a strong magnetic field," *Journal of Physics G: Nuclear and Particle Physics*, vol. 25, no. 8, pp. 1755–1764, 1999.

[71] T. Erber, "High-energy electromagnetic conversion process in intense magnetic fields," *Reviews of Modern Physics*, vol. 38, no. 4, pp. 626–659, 1966.

[72] N. V. Elkina, A. M. Fedotov, I. Y. Kostyukov, M. V. Legkov, N. B. Narozhny, E. N. Nerush, and H. Ruhl, "QED cascades induced by circularly polarized laser fields," *Physical Reivew Special Topics - Accelerators and Beams*, vol. 14, no. 054401, pp. 1–12, 2011.

[73] A. I. Nikishov and V. I. Ritus, "Pair production by a photon and photon emission by an electron in the field of an intense electromagnetic wave and in a constant field," *Soviet Physics JETP*, vol. 25, pp. 1135–1142, December 1967.

[74] E. M. Lifshitz, L. P. Pitaevskii, and V. B. Berestetskii, *Landau-Lifshitz Course of Theoretical Physics, Quantum Electrodynamics*. Pergamon, 2nd edition, January 1982.

[75] E. N. Nerush, I. Y. Kostyukov, A. M. Fedotov, N. B. Narozhny, N. V. Elkina, and H. Ruhl, "Laser field absorption in self-generated electron-positron pair plasma," *Physical Review Letters*, vol. 106, no. 035001, pp. 1–4, 2011.